POLITECNICO DI TORINO
Repository ISTITUZIONALE

Engineering titanium alloys for additive manufacturing: Feedstock design, solidification control, and functional properties

Original
Engineering titanium alloys for additive manufacturing: Feedstock design, solidification control, and functional properties / Bakhshi, M., Ranjkesh, F., Behjat, A., Atzeni, E., Saboori, A.. - In: JOURNAL OF ALLOYS AND COMPOUNDS. - ISSN 0925-8388. - 1080:(2026). [10.1016/j.jallcom.2026.190707]

Availability:
This version is available at: 11583/3015987 since: 2026-09-27T10:49:28Z

Publisher:
Elsevier Ltd

Published
DOI:10.1016/j.jallcom.2026.190707

Terms of use:

This article is made available under terms and conditions as specified in the corresponding bibliographic description in the repository

Publisher copyright

(Article begins on next page)

19 November 2026

Journal of Alloys and Compounds 1080 (2026) 190707

Contents lists available at ScienceDirect

Journal of Alloys and Compounds

journal homepage: www.elsevier.com/locate/jalcom

Review

Engineering titanium alloys for additive manufacturing: Feedstock design, solidification control, and functional properties

Mina Bakhshi [a,b], Farnam Ranjkesh [c,**], Amir Behjat [a,b], Eleonora Atzeni [a,b], Abdollah Saboori [a,b,*]

[a] Department of Management and Production Engineering, Politecnico di Torino, Corso Duca degli Abruzzi 24, Torino 10129, Italy
[b] Integrated Additive Manufacturing Center (IAM@PoliTo), Politecnico di Torino, Corso Castelfidardo 51, Torino 10129, Italy
[c] Department of Applied Science and Technology, Politecnico di Torino, Corso Duca Degli Abruzzi 24, Torino 10129, Italy

ARTICLE INFO

Keywords:
Additive manufacturing
In-situ alloying
Titanium alloys
Columnar to equiaxed transition
Solidification
Microstructure

ABSTRACT

There are thousands of different metallic alloys, but only a few have been officially certified for use in laser powder bed fusion (L-PBF). This is a primary reason why the range of available materials in metal Additive Manufacturing (AM) remains somewhat limited. This review focuses on in-situ alloying combined with fusion-based additive manufacturing processes, specifically titanium (Ti) alloys produced by L-PBF and electron beam powder bed fusion, with laser-directed energy deposition included for comparison. The discussion first addresses the feedstock stage, including powder characteristics, thermophysical mismatches between blended constituents, composition homogeneity, and preparation routes such as conventional blending, MA, satellite milling, and coating. It then links these feedstock conditions to melt-pool transport and solidification, where elemental dissolution, Marangoni-driven mixing, segregation, growth restriction, columnar-to-equiaxed transition, and phase selection are controlled by scan strategy and energy input. Defect formation is also considered within powder bed fusion processing windows, with attention to lack of fusion, keyhole porosity, spatter, denudation, powder-bed instability, and powder-related contamination. The review further compares the microstructural and property responses of major in-situ Ti alloy systems. Multicomponent systems show that the most useful property combinations are obtained when alloy chemistry, feedstock architecture, melt-pool mixing, solidification path, and post-build transformations are treated as a coupled design problem. Up to now, in-situ alloying has proved effective for expanding the Ti alloy design space beyond fixed pre-alloyed powders, but its wider use is still limited by compositional instability, incomplete dissolution, process-window sensitivity,

Abbreviation: AM, Additive Manufacturing; L-PBF, Laser Powder Bed Fusion; EB-PBF, Electron Beam Powder Bed Fusion; L-DED, Laser-Directed Energy Deposition; MA, Mechanical Alloying; LOF, Lack of Fusion; CAD, Computer-Aided Design; SLM, Selective Laser Melting; DMLS, Direct Metal Laser Sintering; CET, Columnar-to-Equiaxed Transition; CP-Ti, Commercially Pure Titanium; HCP, Hexagonal Close-Packed; BCC, Body-Centered Cubic; FCC, Face-Centered Cubic; GB, Grain Boundary; BJT, Binder Jetting; PBF, Powder Bed Fusion; VED, Volumetric Energy Density; LMD, Laser Metal Deposition; DED, Directed Energy Deposition; DMD, Directed Metal Deposition; DLF, Direct Laser Fabrication; LSF, Laser Solid Forming; CNC, Computer Numerical Control; EBSD, Electron Backscatter Diffraction; XRD, X-ray Diffraction; LENS, Laser Engineered Net Shaping; Al_{eq}, Aluminum Equivalent; PSD, Particle Size Distribution; HDH, Hydride-Dehydride; PVA, Polyvinyl Alcohol; FB-CVD, Fluidized-Bed Chemical Vapor Deposition; HCS, Hot-Cracking Susceptibility; CALPHAD (CALPHAD, CALculation of PHAse Diagrams; OMT, Oriented-to-Misoriented Transition; BSE, Backscattered Electron; UTS, Ultimate Tensile Strength; TPMS, Triply Periodic Minimal Surface; SEM, Scanning Electron Microscopy; TEM, Transmission Electron Microscopy; EDS, Energy-Dispersive X-ray Spectroscopy; FFT, Fast Fourier Transform; YS, Yield Strength; GRF, Growth Restriction Factor; LGP, Laser-Glazed Processing; SD, Standard Deviation; TNZF, Ti-14Nb-6Zr-3Fe; IPF, Inverse Pole Figure; T3515, Ti-35Nb-15Zr; RGR, Relative Growth Rate; HAADF, High-Angle Annular Dark-Field; OM, Optical Microscopy; Ti-185, Ti-1Al-8V-5Fe; HAZ, Heat-Affected Zone; LIBS, Laser-Induced Breakdown Spectroscopy; DTEM, Dynamic Transmission Electron Microscopy; GPU, Graphics Processing Unit; CFD, Computational Fluid Dynamics; VOF, Volume-of-Fluid; HIP, Hot Isostatic Pressing; R&D, Research and Development; QA, Quality Assurance; LAM, Laser Additive Manufacturing; ML, Machine Learning; Micro-CT, micro-Computed Tomography; Mo_{eq}, Molybdenum Equivalent; FIB, Focused Ion Beam; WQ, Water Quenching; TRIP, Transformation-Induced Plasticity; TWIP, Twinning-Induced Plasticity; I_{corr}, Corrosion Current Density; R_p, Polarization Resistance; R_{ct}, Charge Transfer Resistance; I_p, Passivation Current Density; N_D, Donor Density; VHN, Vickers Hardness Number; MUD, Multiples of Uniform Distribution; EAS, Elastic Admissible Strain; SaOS-2, Human Osteosarcoma Cell Line 2; HRA, Rockwell Hardness, Scale A.

* Corresponding author at: Department of Management and Production Engineering, Politecnico di Torino, Corso Duca degli Abruzzi 24, Torino 10129, Italy.
** Corresponding author.
E-mail addresses: s329448@studenti.polito.it (F. Ranjkesh), abdollah.saboori@polito.it (A. Saboori).

https://doi.org/10.1016/j.jallcom.2026.190707

Available online 27 August 2026
0925-8388/© 2026 The Author(s). Published by Elsevier B.V. This is an open access article under the CC BY license (http://creativecommons.org/licenses/by/4.0/).

property scatter, and qualification barriers. Further work should therefore focus on validated powder specifications, closed-loop monitoring of melt-pool stability and composition, physics-based modelling linked with non-destructive evaluation, and scalable standards that can move in-situ Ti alloying from laboratory alloy development toward reproducible industrial AM production.

1. Introduction

Additive manufacturing (AM) of metals enables the production of complex and customized parts directly from digital designs, especially when low- to medium-volume production makes traditional tooling costly or inflexible. The digital workflow of AM begins by slicing a computer-aided design (CAD) model into layers, generating toolpaths for each layer, and then consolidating the feedstock, such as powder, wire, or sheet, at the target locations using a focused energy source [1, 2]. Among metal AM techniques, powder bed fusion (PBF) and directed energy deposition (DED) are the most common fusion-based routes. Within PBF, laser powder bed fusion (L-PBF) and electron beam powder bed fusion (EB-PBF) are the two main variants. The choice between them is usually guided by the required geometry, the processability of the material, the available build volume, and economic considerations [3].

As AM technology continues to grow, there is a trend toward using AM as an auxiliary to traditional manufacturing methods rather than as a complete replacement, due to factors such as cost, qualification, and scale [4]. However, AM capabilities continue to evolve, for example through the implementation of multi-laser systems to improve throughput [5]. For this reason, AM is increasingly considered as part of a broader manufacturing route, especially where part complexity, material efficiency, and design flexibility justify its use.

Due to their unique combination of high strength-to-weight ratio, high corrosion resistance, superior mechanical properties, and environmental stability, titanium alloys have been identified as promising candidates for metal AM [6–8]. Their biocompatibility also makes titanium alloys suitable for medical and dental applications, including implants and surgical instruments [9]. The same combination of properties is useful in aerospace, marine, automotive, and biomedical applications, where weight reduction, structural reliability, and long service life are important design requirements [10]. Fig. 1 illustrates the broad application space of additively manufactured titanium alloys.

However, traditional processing of titanium alloys poses several major challenges, including the high reactivity of molten titanium alloys with mold media, low thermal conductivity, which can result in higher machining temperatures, and high spring-back forces during forming [11–13]. While AM may not eliminate all these challenges, it can reduce tooling costs, limit material waste, and shorten lead times for parts with complex geometries. It also enables lightweight structures, part consolidation, and customized designs, which are important for titanium components with demanding performance or design requirements [14].

Beyond component fabrication, AM also creates opportunities for titanium alloy development through feedstock-based composition control. Among the different ways to control composition, cost, and alloy development in powder-based metal additive manufacturing, feedstock strategy plays a central role. Pre-alloyed powders provide reliable and repeatable compositions, but they also restrict rapid alloy modification because each new composition requires a separately produced powder

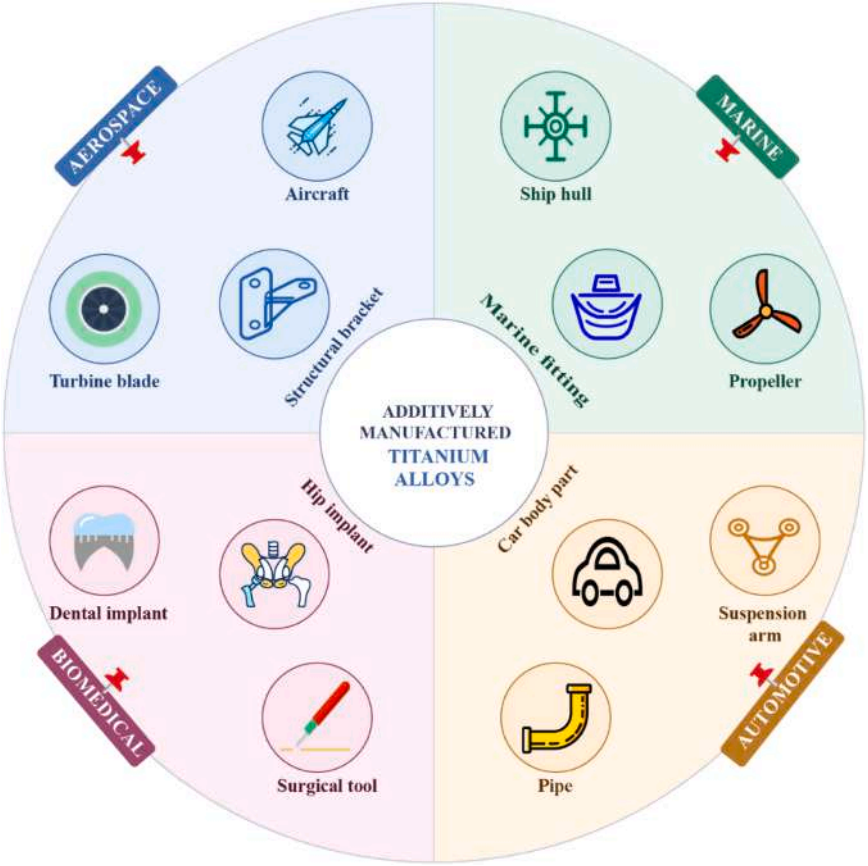


Fig. 1. Representative application areas of additively manufactured titanium alloys in aerospace, marine, automotive, and biomedical sectors.

batch. In contrast, in situ alloying uses elemental, master alloy, or surface-modified powders and allows alloy formation during AM. This approach is therefore attractive for exploring new titanium alloy compositions, although its success depends on controlling powder mixing, melting behavior, elemental segregation, and final microstructural homogeneity [15].

The increasing interest in this approach is reflected in the publication trends shown in Fig. 2. In Figs. 2(a) and 2(b), the publication number in 2014 was set to 100 for each category. The curves, therefore, do not show the absolute number of papers. Instead, they show how strongly each topic has grown relative to its own 2014 level. For example, a value of 500 means that the number of publications increased by a factor of 5 compared to 2014. This normalization makes it easier to compare broad fields, such as all metal additive manufacturing, with smaller subsets, such as in situ titanium additive manufacturing.

Fig. 2(a) shows that publications on in situ metal additive manufacturing have grown faster than the overall metal additive manufacturing literature. A similar trend is observed in Fig. 2(b), where in situ titanium additive manufacturing shows stronger relative growth than the broader titanium additive manufacturing field. To avoid relying only on indexed growth, Fig. 2(c) presents the actual share of in situ studies within the corresponding literature. This share has also increased over time, both within metal additive manufacturing and within titanium additive manufacturing. Together, these trends indicate that in situ alloying is not only growing as the broader additive manufacturing field expands but is also becoming a more visible and distinct research direction in the literature.

To complement Fig. 2, which illustrates how much the titanium in-situ AM literature has expanded over time, Fig. 3 addresses where this activity is concentrated by mapping the geographic distribution of Scopus-indexed titanium in-situ AM publications.

After showing the growth of the literature and its geographic distribution, it is necessary to discuss the technical factors that control reproducibility in in-situ alloying. Consistent results in in-situ alloying depend on proper powder selection and preparation, as well as a clear understanding of melt pool transport and solidification phenomena, including enthalpy of mixing, Marangoni flow, and the columnar-to-equiaxed transition (CET). These phenomena control elemental mixing, microstructure formation, and defect development [16]. Recent studies have also shown that partial inhomogeneities produced during in-situ alloying can be used beneficially to form hierarchical microstructures. At the same time, advanced powder engineering, improved spreading strategies, and process modeling are increasingly used to reduce chemical segregation and refine grain size [17,18]. Before discussing these challenges in more detail, it is useful to briefly introduce the phase stability of titanium alloys, as the response of titanium to in situ alloying is strongly controlled by the α and β phase stabilities.

Pure titanium exists in two allotropic forms: the low temperature α phase with a hexagonal close packed (HCP) crystal structure, and the high temperature β phase with a body centered cubic (BCC) crystal structure, which becomes stable above about 883 °C [19]. Depending on the type and amount of alloying additions, titanium alloys are commonly classified as α, near α, α + β, β, and metastable β alloys [20]. α stabilizing elements, such as aluminum, oxygen, nitrogen, and carbon, increase the α to β transformation temperature, whereas β stabilizing elements, such as molybdenum, vanadium, niobium, tantalum, chromium, manganese, and iron, decrease it [21]. The balance between α and β stability therefore has a direct influence on the resulting microstructure and properties. For example, β and metastable β alloys generally exhibit lower elastic moduli than α and α + β alloys, making them attractive for reducing stress shielding in biomedical applications [22,23]. In contrast, α + β alloys are widely used because they provide a useful balance of strength, toughness, and crack growth resistance [23].

1.1. Integrated alloy-design framework for in-situ AM of titanium alloys

These phase-stability concepts form the basis of several practical approaches used in titanium alloy design. One of the simplest is the use of empirical equivalency parameters, particularly the molybdenum equivalent (Mo_{eq}) and aluminum equivalent (Al_{eq}). represents the combined β-stabilizing effect of alloying additions in terms of an equivalent Mo content, whereas expresses the overall α-stabilizing contribution relative to Al. These parameters provide a convenient first estimate of whether a composition tends toward α, near α, α + β, near β, metastable β, or fully β behavior. However, they remain approximate compositional indicators, since the final phase constitution also depends on processing conditions, cooling rate, and heat treatment [10,16].

A commonly used form of these relations is given as [10]:

$$Mo_{eq} = [Mo] + 2.5[Fe] + 1.7[Co] + 1.7[Mn] + 1.25[Ni] + 1.25[Cr] + 0.67[V] + 0.4[W] + 0.28[Nb] + 0.2[Ta] \quad (1)$$

$$Al_{eq} = [Al] + 0.17[Zr] + 0.33[Sn] + 10[O] \quad (2)$$

where the bracketed terms denote elemental concentration in wt%. Based on this framework, alloys with higher Al_{eq} and lower Mo_{eq} tend toward α or near α compositions, while alloys with higher Mo_{eq} and lower Al_{eq} tend toward near β, metastable β, or fully β compositions. A schematic classification of titanium alloys in the Mo_{eq}-Al_{eq} space is shown in Fig. 4 [10].

It should also be noted that several modified Mo_{eq} relations have been proposed for multicomponent titanium alloys. For example, a more recent relation includes a wider range of β-stabilizing, neutral, and α-stabilizing elements:

$$Mo_{eq} = [Mo] + 1.25[V] + 0.59[W] + 0.28[Nb] + 0.22[Ta] + \quad (3)$$

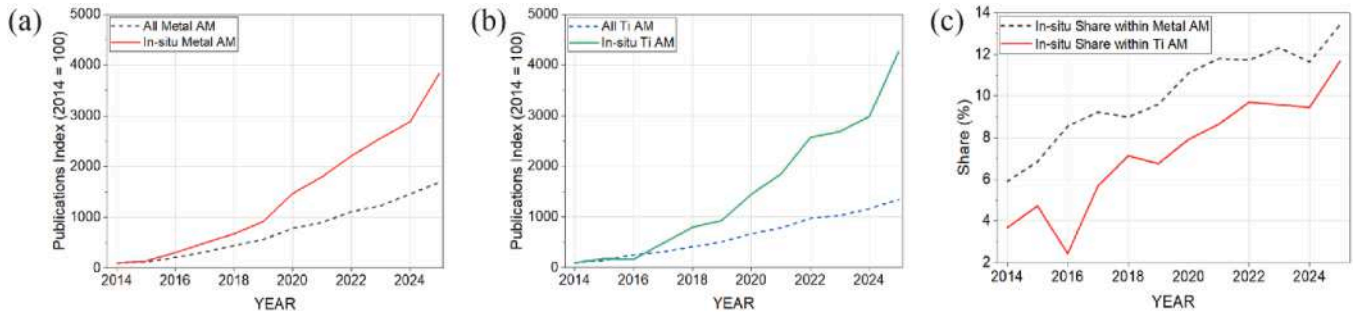


Fig. 2. Scopus-derived publication trends related to in-situ alloying in additive manufacturing: (a) indexed growth for overall metal additive manufacturing and its in-situ subset, (b) indexed growth for titanium additive manufacturing, including its in-situ alloying subset, and (c) share of in situ studies within the corresponding total literature. In panels (a) and (b), 2014 publication numbers were set to 100 for each category, so the curves show relative growth rather than absolute publication counts. Note: Scopus keyword-based queries were used; results represent indicators rather than exact counts.

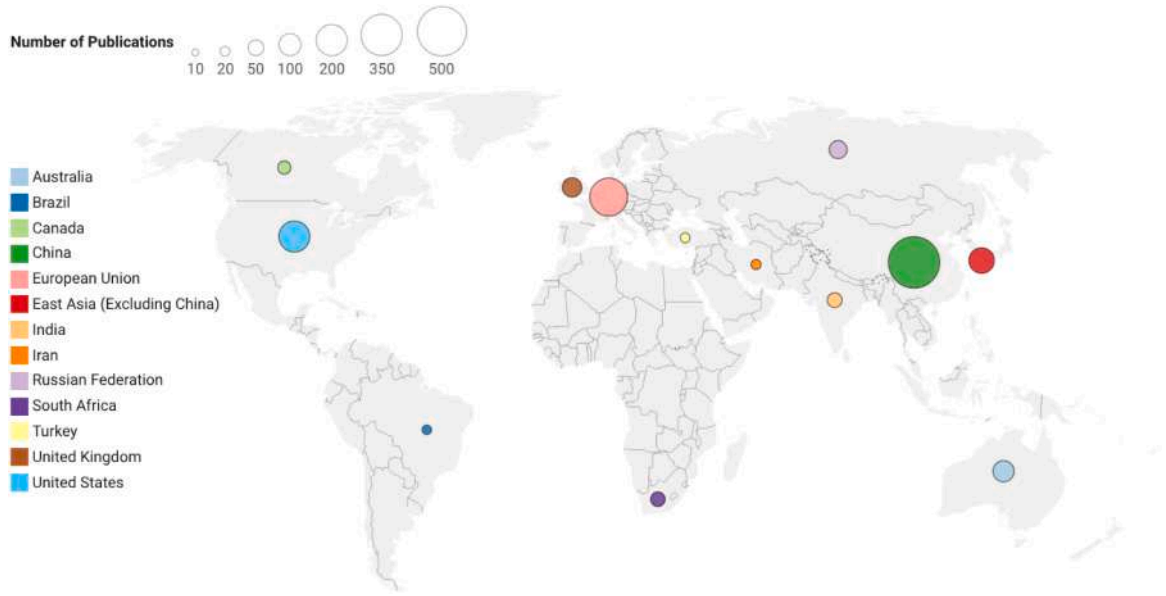


Fig. 3. Geographic distribution of Scopus query-retrieved records on titanium in-situ additive manufacturing (cumulative, 2014–2025). Bubble size indicates the number of records returned by the query for each country/region; selected regions are aggregated to reduce marker overlap and improve readability. Note: results are query-based indicators rather than exact publication totals.

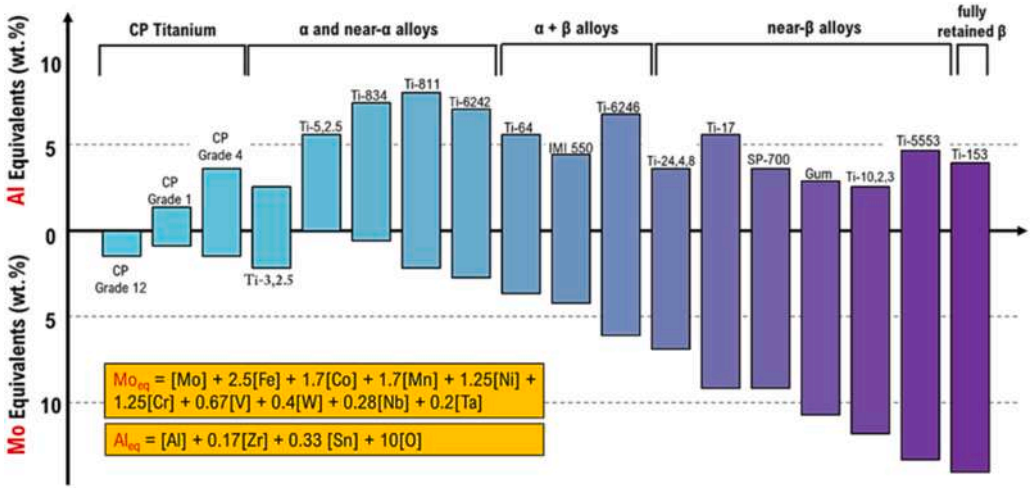


Fig. 4. Classification of titanium alloys based on Mo_{eq} and Al_{eq} values. Reproduced from [10].

$$1.93[Fe] + 1.84[Cr] + 1.5[Cu] + 2.46[Ni] + 2.67[Co] +$$

$$2.26[Mn] + 3.01[Si] + 0.3[Sn] + 0.47[Zr] - 1.47[Al]$$

This expanded expression is useful when comparing more complex Ti alloy systems, especially those containing elements that are not included in the simpler Mo_{eq} relation. However, the same limitations remain for multicomponent alloys, particularly when local chemical homogeneity and AM thermal history are considered.

Beyond empirical equivalency parameters, the *Bo-Md* method provides an additional electronic framework for the design of titanium alloys, particularly β and metastable β alloys. In this approach, *Bo* represents the bond order and describes the covalent bond strength between Ti and an alloying element, while *Md* represents the d orbital energy level of the alloying element and is related to both electronegativity and atomic radius. These two parameters are obtained from molecular orbital calculations and used to describe, from an electronic point of view, the effect of alloying elements on phase stability [24,25].

For multicomponent alloys, the average *Bo* and *Md* values are calculated from the alloy composition as [24]:

$$\overline{Md} = \sum_{i=1}^{n} X_i.(Md)_i \quad (4)$$

$$\overline{Bo} = \sum_{i=1}^{n} X_i.(Bo)_i \quad (5)$$

where *Xi* is the atomic fraction of element *i*, and *(Bo)i* and *(Md)i* are the corresponding bond order and *d* orbital energy level values of that element. By calculating these average values, titanium alloys can be positioned on *Bo-Md* phase stability maps. These maps are useful for distinguishing α, α + β, β, and metastable β regions, and for relating β phase stability to martensitic transformation, ω phase formation, elastic modulus, and deformation mechanisms such as slip and twinning [25].

The extended *Bo-Md* diagram is especially useful for β-type titanium alloys because it includes the β/β + ω boundary, the martensite start and finish boundaries at room temperature, and approximate elastic modulus ranges [26]. The elemental *Bo* and *Md* values used for these

calculations are usually taken from molecular orbital calculations for bcc Ti. Selected values for alloying elements commonly discussed in titanium alloy design are listed in Table 1.

These averaged electronic parameters allow titanium alloys to be positioned on *Bo Md* maps, as shown in Fig. 5.

However, as with Mo_{eq} and Al_{eq}, the *Bo-Md* method should be used as a compositional design guide rather than a complete prediction of the final microstructure. This limitation is particularly important in AM, where powder dissolution, incomplete mixing, rapid solidification, repeated thermal cycling, local thermal gradients, and post-processing can all modify the final phase constitution and properties. Therefore, *Bo-Md* maps are useful for narrowing the alloy design space, but they should be combined with thermodynamic calculations, process understanding, and experimental validation in AM alloy development [27].

Although Mo_{eq} / Al_{eq} and Bo-Md both provide information on titanium alloy phase stability, they address different aspects of alloy design. Mo_{eq} / Al_{eq} offers a simple empirical method for screening the overall α- and β-stabilizing effects of a nominal composition, while *Bo-Md* provides an electronic description that is particularly useful for assessing β-phase stability, metastability, martensitic or ω transformation tendencies, and elastic response. Both approaches can help narrow the initial composition space, but neither directly considers the thermal and solidification conditions imposed during AM. They also do not explicitly incorporate feedstock-scale effects such as incomplete powder dissolution, local segregation, or melt-pool-scale composition variations.

Solidification-based criteria provide a complementary level of information. The growth restriction factor (Q) is commonly used to characterize the effect of solute on growth restriction during solidification. However, Q alone does not uniquely determine the growth response because other factors, including the partition coefficient and imposed undercooling, also contribute [28]. The local temperature gradient (G) and solidification rate (R), discussed in detail in Section 5.1, describe the thermal conditions that influence grain morphology and the CET [16,29]. This coupling between alloy constitution and solidification conditions has been demonstrated in AM of titanium alloys, where solute-induced constitutional undercooling can promote CET and grain refinement [30]. Therefore, Mo_{eq} / Al_{eq} and *Bo-Md* are mainly useful for composition and phase-stability screening, whereas Q and *G-R* conditions provide information on how the selected chemistry is expected to respond during solidification.

Several studies illustrate different elements of this integrated design philosophy. Alabort et al. [31] combined high-throughput thermodynamic calculations and property screening to develop a low-modulus titanium alloy specifically for AM. Chen and Qiu [32] similarly developed the metastable Ti-6Mo-5.5Cr-1Co-0.1 C alloy for L-PBF by considering *Bo-Md* phase stability together with growth-restriction and grain-refinement behavior. These examples show that phase-stability and solidification criteria can be considered together when narrowing the composition space, although the specific criteria used depend on the alloy system and the intended microstructural or property target.

For in-situ alloying, the feedstock and melt-pool stages must also be considered because the nominally designed composition may differ from the local composition that finally solidifies. Differences in particle size, melting point, density, and dissolution behavior can modify the local chemical state before solidification. Choi et al. [33] demonstrated in laser-directed energy deposition (L-DED) using blended Ti-6Al-4V and Co-Cr-Mo powders that enhanced β-phase stability and constitutional undercooling can act together in promoting an equiaxed β-grain

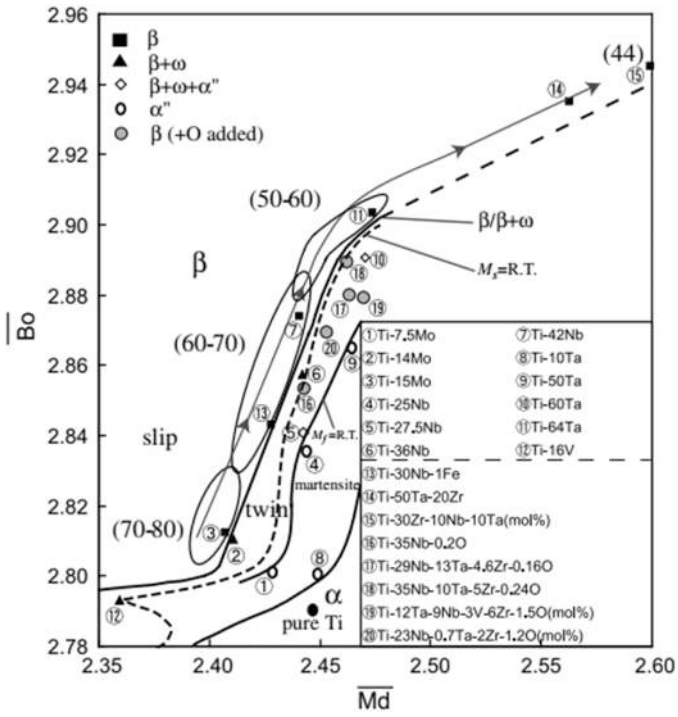


Fig. 5. Schematic *Bo-Md* phase stability map for β-type titanium alloys [25].

structure. A more recent example is the in-situ L-PBF Ti-14Nb-6Zr-3Fe alloy discussed in Section 6.2.2. Its composition was selected with reference to *Bo-Md* phase-stability criteria, while the resulting grain structure was also influenced by the growth-restriction effect of Fe, constitutional supercooling around residual Nb particles, and scan-strategy-dependent thermal conditions [34]. These examples show that phase-stability criteria alone are not sufficient for in-situ alloy design and should be considered together with feedstock behavior, solidification conditions, and experimental validation.

Recent computational strategies extend this concept by integrating several criteria within a single design framework. Su et al. [35] combined CALculation of PHAse Diagrams (CALPHAD)-based Scheil calculations and solidification descriptors, including Q, solidification freezing range, and hot-cracking susceptibility (HCS), with physics-based models, machine learning (ML), and multi-objective optimization. The selected β-Ti composition was subsequently validated by L-PBF. Such computational approaches can substantially narrow the composition space that requires experimental screening. For in-situ alloying, however, additional experimental validation remains necessary because feedstock dissolution and melt-pool-scale chemical homogeneity must still be verified under the actual processing conditions [34,36].

Based on the literature discussed above, a possible integrated design framework for in-situ AM titanium alloys is proposed here. Mo_{eq} / Al_{eq} can be used for initial compositional screening, while *Bo-Md* provides additional assessment of phase stability and related transformation behavior. Thermodynamic and solidification calculations can then be used to evaluate phase formation, solidification range, and segregation tendency, while Q and *G-R* conditions provide complementary information on growth restriction and grain morphology. For in-situ alloying,

Table 1
Bo and *Md* values of selected alloying elements in bcc Ti used for calculating average electronic parameters in titanium alloys.

Element	Ti	Al	Si	Sn	Zr	V	Nb	Ta	Mo	W	Fe	Cr	Mn	Co	Ni	Cu
Bo	2.790	2.426	2.561	2.283	3.086	2.805	3.099	3.144	3.063	3.125	2.651	2.779	2.723	2.529	2.412	2.114
Md	2.447	2.200	2.200	2.100	2.934	1.872	2.424	2.531	1.961	2.072	0.969	1.478	1.194	0.807	0.724	0.567

Adapted from Abdel-Hady et al. [25].

these composition- and solidification-based assessments should then be considered together with feedstock characteristics, powder dissolution, melt-pool behavior, and experimental validation. The relative importance and order of these tools may vary depending on the alloy system and the intended property or microstructural target. Therefore, the proposed framework should be regarded as a flexible design guide rather than a universal sequence. In this sense, the different approaches are complementary rather than interchangeable and can be used to progressively narrow the composition and processing spaces that require experimental investigation.

1.2. Phase transformations and microstructural response under AM conditions

In AM, repeated layer by layer thermal cycles produce steep local thermal gradients and high solidification rates, leading to microstructures that differ from those obtained by conventional processing [37]. In titanium alloys, these rapid heating and cooling conditions strongly affect the stability and transformation behavior of the high temperature β phase. During cooling, β may transform into equilibrium α or into metastable products such as martensitic α′, α″, and ω, depending on alloy composition, cooling rate, and thermal history [38]. As a result, metastable phases are frequently reported in additively manufactured titanium alloys, especially when rapid solidification and incomplete solid-state transformation occur.

Both the AM process parameters and the material being processed influence the resulting phase constitution, grain morphology, and mechanical properties. L-PBF processes typically involve high cooling rates and relatively low base plate temperatures, which favor the retention of α′ martensite through rapid quench transformation pathways in titanium alloys [39]. In contrast, EB-PBF and L-DED processes usually involve higher preheating temperatures and repeated thermal cycles, which promote α′ decomposition into lamellar α + β structures [38,39]. It is reported that Commercially Pure Titanium (CP-Ti) develops different dominant microstructures when processed by L-PBF compared with EB-PBF or L-DED [40,41].

As a result, L-PBF parts often show higher strength and hardness but lower ductility than parts fabricated by EB-PBF or L-DED. By contrast, EB-PBF and L-DED parts generally show greater ductility, mainly because of the formation of lamellar α + β microstructures [42]. Grain morphology also contributes to anisotropy. Additively manufactured titanium alloys commonly develop elongated prior β grains aligned with the local thermal gradient, while grain boundary α (GB-α) forms along prior β grain boundaries. This directional grain structure can lead to build direction dependent strength and ductility through grain size effects, often described by the Hall-Petch relationship, and through phase and strain partitioning during deformation.

1.3. Opportunities and challenges of in-situ alloying

Within this context, in-situ alloying represents the practical processing route through which these compositional design concepts can be explored in AM, but its effectiveness depends strongly on feedstock preparation, melting behavior, elemental transport, and solidification conditions.

In-situ alloying substitutes pre-alloyed powders with elemental, master alloy, or surface-modified powder blends that form an alloy during printing, using feedstocks produced by mechanical blending, satellite milling, or ball milling. In-situ alloying increases composition-design flexibility and potentially reduces powder costs compared to fixed-chemistry pre-alloyed grades, enabling the development of both non-conventional and functionally graded materials tailored to application-specific requirements [43]. The localized energy input associated with AM enables the development of combinatorial composition libraries via high-throughput fabrication methods, in which powders can be blended in real time to produce compositional gradients during a single build operation [44].

In addition to compositional flexibility, in-situ alloying can also be used to modify solidification behavior. Suitable alloying additions may alter constitutional undercooling, growth restriction, and heterogeneous nucleation, thereby promoting the transition from columnar to more equiaxed prior-β grains in titanium alloys. This is important because columnar prior-β grains are often associated with texture and anisotropic mechanical response in additively manufactured titanium alloys. Therefore, element selection in in situ alloying should be considered not only as a route to target composition, but also as a tool for controlling solidification path and grain morphology [33].

However, these advantages are accompanied by several limitations related to feedstock preparation and processing. In addition to common AM defects such as porosity, cracking, and oxide formation, in situ alloying can lead to elemental loss, incomplete dissolution, intermetallic formation, and local composition variations [45]. The extent of these problems depends strongly on particle size, morphology, distribution, and differences in melting behavior among the constituent powders. Feedstock preparation can reduce some of these issues. For example, satelliting or mechanical blending of fine constituents has produced Ti-6Al-4V microstructures comparable with those obtained from pre-alloyed powders when sufficient mixing occurs within the melt pool [36,46]. A broader comparison of these two feedstock strategies, including defect formation, consistency of properties, and the available evidence on stability during service, is discussed in Section 6.

2. AM methods for in-situ alloying

AM of titanium alloys is mainly carried out using PBF and DED. Within the scope of this review, the discussion is focused on L-PBF, EB-PBF, and L-DED since these fusion-based processes are the most widely reported routes for in-situ alloying of titanium alloys. Although binder jetting (BJT) has also been explored for some titanium alloy applications, it is not discussed in detail here because the present review focuses on fusion-based processing. Since in-situ alloying outcomes are strongly linked to melt pool stability, elemental mixing, and defect sensitivity, a focused discussion of PBF process physics and defect mitigation is included to provide the basis for interpreting reported alloying behavior.

In these processes, fabrication begins with slicing a computer-aided design model into layers, followed by toolpath generation and localized consolidation of the feedstock using a laser or electron beam. In PBF, thin layers of powder are selectively melted by either a laser beam in L-PBF or an electron beam in EB-PBF. In L-DED, powder is delivered directly into a laser-generated melt pool, enabling simultaneous material addition and alloying. Both PBF and L-DED enable the production of near-net-shape components from digital models. PBF can achieve high density and fine geometrical resolution, but its use for large aerospace-class structures is limited by build volume and deposition rate. L-DED, in contrast, provides higher deposition rates and greater scalability, though often at lower dimensional resolution and with a larger melt pool [1,47].

As shown in Fig. 6, the main fusion-based AM routes used for in-situ alloying differ in their energy sources and feedstock delivery methods. L-PBF and EB-PBF consolidate thin powder layers using laser and electron beams, respectively, whereas L-DED introduces powder directly into a laser-induced melt pool. These differences strongly affect thermal history, melt pool size, solidification conditions, and the extent of elemental mixing during in-situ alloying.

All three routes can be used for in-situ alloying, although each route has its own advantages and limitations. In PBF, pre-blended or surface-modified elemental powder mixtures are spread layer by layer and locally melted, allowing alloy formation within individual melt tracks and during repeated remelting cycles. In L-DED, the direct delivery of powder into the melt pool enables more flexible material feeding and higher deposition rates, but the larger melt pool and coarser resolution can influence chemical homogeneity and microstructural control. Therefore, the choice of process depends on part size, required

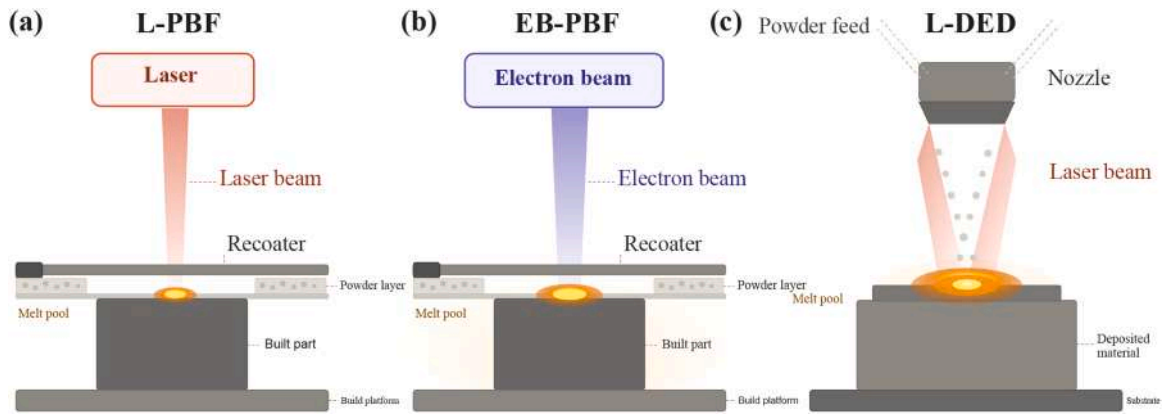


Fig. 6. Main fusion-based additive manufacturing routes used for in-situ alloying of titanium alloys: (a) L-PBF, (b) EB-PBF, and (c) L-DED.

resolution, alloy reactivity, shielding conditions, and the degree of elemental mixing required by the in-situ alloying strategy [1,40,47].

2.1. L-PBF

L-PBF, also referred to in the literature as selective laser melting (SLM), direct metal laser sintering (DMLS), and laser metal fusion (LMF), builds parts by melting thin layers of powder using a high-energy laser, with selected scan vectors. In L-PBF, layers are successively spread and selectively melted, and the same process steps (from CAD slicing to part removal) follow a predetermined digital process flow for each part. Most practical systems run under inert atmospheres (Ar/N_2) to prevent oxidation. They have predetermined scanning strategies and support structures to create internal passages and complex organic geometries [48]. The input parameters that determine how the molten metal behaves during L-PBF are volumetric energy density (VED), laser power (P), scan speed (v), hatch spacing/distance (h), and layer thickness (t). Energy density is commonly used to regulate both density and microstructure during L-PBF. As a result of its highly localized beam and the rapid cooling rates (up to about 10^6 K s^{-1}) produced by L-PBF fast scans, the material can be refined to grain-size levels. However, this results in anisotropic behavior, as well as pore and crack defects, due to the rapid cooling rate when the processing window is incorrectly set [48,49].

L-PBF has a relatively small focal area, which generally results in a good surface finish and finer feature sizes. However, it does require very specific, often difficult-to-determine parameter settings to avoid defects such as lack of fusion (LOF) or keyhole. Preheating is optional for L-PBF, while it is required for some other additive manufacturing processes [1, 37,50]. Due to the limited availability and high cost of specialized pre-alloyed titanium powders, researchers are developing new methods to produce titanium alloys in-situ from non-homogeneous powder blends to accelerate alloy development in L-PBF [47,51,52].

2.2. EB-PBF

The EB-PBF process uses a controlled electron beam, guided by electromagnetic fields, to selectively melt an electrically conductive powder bed inside a vacuum chamber. The conversion of the beam kinetic energy into heat occurs at the surface of the powder. Due to the need for a low-vacuum path to minimize electron scattering, a small helium backfill is introduced during preheat to reduce electrostatic charge on the part and smoke formation [53,54].

The powder bed is heated to a target ambient temperature prior to the contour and hatch melting. This allows the build to remain at an elevated temperature, resulting in a significant reduction in residual stresses and enabling the processing of crack-susceptible alloys [54].

EB-PBF has been successfully used to develop dense parts for aerospace, automotive, and medical implant applications. The preheat time depends on the powder's electrical conductivity and sintering temperature. The beam scan strategy and scanning rate need to be optimized to ensure stable melts [55,56]. While EB-PBF can produce lower residual stresses than L-PBF due to its higher bed temperatures, the surface finishes and dimensional accuracy of parts produced via EB-PBF are generally less refined than those produced via L-PBF, due to having a bigger focal area. Therefore, the choice of process ultimately depends on whether one desires to utilize EB-PBF's ability to produce parts with low residual stresses and defects, or to produce features that are too fine to tolerate the lack of precision associated with EB-PBF [57].

2.3. L-DED

In L-DED, powder feedstock is delivered into a laser generated melt pool along sliced toolpaths. The material is consolidated layer by layer as the nozzle or substrate moves according to the programmed deposition path [35]. This process is also reported in the literature under related terms such as laser metal deposition (LMD), directed metal deposition (DMD), direct laser fabrication (DLF), and laser solid forming (LSF), although the terminology may vary depending on the system configuration and application [50]. In powder-fed L-DED, particles are commonly injected into the melt pool by a carrier gas, often through a coaxial nozzle. Melting, mixing, and solidification then occur during deposition. The use of multi-axis motion and computer numerical control (CNC) allows complex deposition paths, local material addition, and repair of existing components. Since titanium alloys are highly reactive at elevated temperatures, inert shielding of the melt pool is required to reduce oxidation during processing [15].

Compared with PBF, L-DED is generally preferred for large near net shape components, coatings, claddings, and repair applications. It is also suitable for producing functionally graded materials, since the feed composition can be changed during deposition using multi hopper, multi nozzle, or separate elemental powder delivery systems [58,59]. However, the geometrical accuracy and surface finish are usually lower than those obtained by PBF. Since L-DED does not use a recoater to spread and level each powder layer, layer wise deviations can accumulate during the build. For this reason, post-processing machining is often required to reach the final dimensional tolerance and surface quality [59]. In general, powder fed L-DED uses higher laser power and lower scan speed than PBF to form a melt pool large enough to melt the injected particles completely and support elemental mixing. Carrier gas flow also contributes to powder delivery and local shielding during deposition [15]. For these reasons, L-DED is commonly used for structural buildup, tooling, coatings, and repair operations, where metallurgically bonded material can be added directly to a substrate or to an existing component [37].

2.4. PBF process physics and defect control

Because L-PBF and EB-PBF are the most widely reported routes for titanium alloy additive manufacturing, and because many in-situ alloying studies rely on powder-based feedstocks, PBF process physics is discussed in greater detail here. In these processes, alloying behavior is closely linked to beam-powder coupling, melt pool stability, powder-bed condition, and defect formation. Therefore, understanding PBF-specific defect mechanisms provides a useful basis for interpreting the success or limitations of in-situ alloying in titanium alloys.

2.4.1. Beam-powder coupling and melt pool dynamics

Beam-powder coupling provides the first link between feedstock condition and melt pool formation in PBF. The beam-powder interaction in PBF of Ti alloy occurs initially as an energy deposition into a loosely packed bed of powder. In L-PBF, the initial interaction between the laser and the powder bed involves optically based multiple scattering in the unconsolidated, oxidized powder bed, which can increase the powder bed effective absorptance relative to a flat surface. The powder bed response then evolves rapidly as the powder particles heat, neck, melt, and form a solid melt track. Because the first few milliseconds of exposure time have a disproportionate effect on the overall stability of the process, or more specifically on melt-track stability, time-resolved measurement techniques and modeling techniques using radiative transfer methods are important for describing this transient interaction [60]. Specifically, in Ti-6Al-4V, the native oxide and powder/surface chemistry have been shown to affect the amount of absorption and ultimately the melt behavior of the powder, thereby linking the degree of oxidation of the powder to the formation of defects in the final product [61]. The corresponding energy-coupling mechanism differs in EB-PBF, where the beam interacts with the powder via electron energy transfer rather than optical absorption. In EB-PBF, kinetic energy is transferred from the accelerated electrons to the powder. Ti-6Al-4V processing by EB-PBF is typically conducted in a controlled vacuum environment ($<$ 1 Pa) or in a vacuum-controlled environment with a low helium process gas at a very low partial pressure, both to allow transmission of the electron beam and to limit oxidation and contamination of reactive powders [57].

After energy coupling, melt pool stability becomes controlled by fluid flow, recoil pressure, and the selected processing window. Following the absorption of energy in the powder, the melt pool shape is mainly determined by vigorous convection and vapor-recoil effects, and the processing window can span from relatively stable conduction-like melting to highly unstable deep-melt regimes as evaporation-driven recoil increases in intensity. In L-PBF, high-fidelity simulations and in-situ X-ray imaging have identified keyhole collapse as an important mechanism for pore formation in Ti-6Al-4V under high-energy input conditions. Pores can form through the collapse of keyholes formed during the scanning process. In addition, scaling laws have been established relating process inputs to both the stability and porosity of the material over a range of materials, including Ti-6Al-4V [62,63]. For EB-PBF, melt pool behavior is commonly described using process window variables that reflect the different beam control strategies. In EB-PBF, process windows for Ti-6Al-4V are typically described in terms of scan speed and line energy (energy per unit length). The selected strategy can influence not only the build rate and the microstructure of the material, but also the evaporation-induced compositional changes of the material resulting from the high energy input [64].

2.4.2. Process parameters and energy metrics

The transition from beam-powder coupling to stable consolidation is controlled mainly through the selection of process parameters. P (W), v (mm s^{-1}), h (μm), and t (μm) are the primary machine-controlled parameters for L-PBF of Ti alloys. For titanium alloys, these parameters are commonly discussed through the Ti-6Al-4V processing window because it remains the most widely used benchmark alloy in the literature. In the case of Ti-6Al-4V, commonly reported processing windows use several hundred-watt fiber lasers, v around 10^{3} mm s^{-1}, tens of micrometers in t, and h of the order of hundreds of micrometers. These conditions are selected to balance melt pool stability, density, and productivity. Process maps describe the operational windows and transitions between LOF, stable melting, and keyhole regimes [48,61].

Because EB-PBF uses a different beam control strategy, its process parameters are described differently from L-PBF. Beam power in EB-PBF is generally determined by beam current at the accelerating voltage, and the beam is moved electronically, allowing large effective deflections and scan rates, as well as multi-pass heating and melting strategies. Importantly, EB-PBF involves a specific preheat phase in which the powder layer is scanned, often multiple times, to increase temperature and form sintering bridges between particles. This can improve the electrical and thermal coupling between particles and stabilize the powder bed [57]. The preheat phase is directly related to preventing smoke instability, which refers to disturbances in the powder bed caused by charging when charge dissipation and powder-bed stability are insufficient [65].

Although simplified energy metrics are useful for comparing parameter sets, they should not be treated as complete descriptors of melt pool behavior. VED is a common metric in L-PBF: VED = P/(v.h.t). It is sometimes used to characterize regimes from LOF to keyhole across different parameter sets. However, VED does not include information regarding spot size, absorptivity, overlap geometry, scan strategy, and thermal history. Thus, two equal-VED combinations can produce different melt pools and porosities. Therefore, VED should be used only to provide a general description within a study, whereas physical descriptions or process mapping are more reliable when moving to other process conditions [66]. This limitation becomes even more important when comparing L-PBF with EB-PBF. For EB-PBF, the same cautionary recommendation is even more applicable to comparisons among processes, since the process windows of EB-PBF are often characterized by line energy in addition to v and h, and the selected energy input strategy influences evaporation processes.

2.4.3. Defects and mitigation

The dominant defects in PBF depend strongly on the energy source, powder-bed condition, and local thermal regime. In L-PBF, defect formation is commonly discussed in terms of LOF, keyhole porosity, spatter, denudation, and powder-related contamination, while EB-PBF introduces additional powder-bed stability issues under vacuum or low-pressure conditions.

LOF defects typically appear as irregular inter-track and inter-layer voids that form when track overlap is insufficient and/or the local energy input is too low. Consequently, they often align with scan vectors or concentrate along layer interfaces. In Ti-6Al-4V produced by L-PBF, synchrotron tomography has directly linked LOF morphology and spatial distribution to under-melting regimes. Complementary single-track and bulk studies further show that LOF can be reduced by improving track overlap, for example, by reducing h, increasing P, or reducing v, thereby promoting full consolidation without necessarily entering the keyhole regime [67,68].

At the opposite side of the process window, excessive local energy input can promote keyhole instability. In L-PBF, keyhole porosity occurs when vapor-recoil depresses the melt surface into a keyhole. Ultra-fast X-ray imaging indicates that the oscillation and collapse of the over-deepened keyhole traps gas and produces near-spherical pore formation, particularly during rapid changes in v or at h overlaps. Additionally, stabilizing the melt pool in conduction or shallow-keyhole regimes can reduce or suppress this mechanism. Dimensionless universal scaling can capture the boundaries between stable and unstable behavior across different alloys and processing systems [69].

Besides melt pool instability, powder redistribution around the melt track can also contribute to defect formation. Spatter and denudation in L-PBF are caused by the vapor jet interacting with the shielding gas flow,

which can lead to powder entrainment and powder-depleted bands near the melt track. These powder-depleted regions may increase the risk that adjacent tracks will develop LOF defects. The diagnostics show that the design of the gas flow and ambient pressure significantly affects these issues; therefore, nozzle and flow optimization, together with powder loop management, such as filtering and sieving oxidized spatter, can improve L-PBF process stability [70,71].

In contrast to L-PBF, EB-PBF operates in a different processing environment and therefore faces a different powder-bed instability concern. EB-PBF differs from L-PBF because it operates in controlled vacuum conditions at low helium partial pressures rather than conventional shielding-gas crossflow. A common powder bed disturbance in EB-PBF is referred to as smoke and was experimentally characterized as sudden powder motion and/or explosions associated with charging-related mechanisms. This instability can evolve through multiple phases if charge dissipation and powder-bed stability are not adequately controlled [57].

Feedstock condition provides an additional defect source, particularly important for reactive titanium alloys. For example, in Ti-6Al-4V feedstock, oxides, oxygen pickup, and inclusions remain central concerns for defect formation and property degradation. Powder reuse thickens surface oxides and nitrides, increases the amount of O and N in the material, alters absorptance and flow, and enables the incorporation of oxidized particles and spatter as inclusions or defect seeds. Low ppm O2 levels, tight humidity control, and proper powder handling/storage, combined with reuse limits and sieving, reduce risks. Studies have also directly correlated increased powder oxidation with defect populations and property degradation, while decreasing the oxygen partial pressure is a method to mitigate the defects [72].

The main defect mechanisms discussed above are summarized in Fig. 7 using representative observations from Ti-6Al-4V powder bed fusion studies. The figure compares lack of fusion and keyhole porosity, the effect of process parameters on pore morphology, keyhole pore formation near a laser turn point, and powder motion associated with spatter and denudation.

3. Feedstock properties

Feedstock selection sets the boundary conditions for in situ alloying because it controls powder delivery, energy absorption, melting, and mixing before solidification. In powder-based routes, spreadability and packing mainly depend on particle size distribution (PSD), morphology, and surface chemistry. In situ blends introduce an additional level of complexity because differences in melting point, density, absorptivity, and other thermophysical properties among constituents can promote segregation and incomplete homogenization during processing [15].

Therefore, this section discusses the powder-quality metrics that control spreading and packing, the thermophysical mismatches that affect melting and mixing, and the alloy-design metrics used to anticipate solidification behavior under AM thermal cycles.

3.1. Powder quality metrics

For powder-based AM, powder spreadability is governed by PSD, particle morphology and sphericity, and surface chemistry. In this context, PSD controls how particles pack, flow, and absorb energy during spreading and melting. Finer-powder fractions improve absorptance and lower unmelted residuals, but they also increase interparticle friction and cohesion. A broader PSD allows finer fractions to fill voids, increasing the density of a powder layer but decreasing its flowability. Therefore, the effective layer density of a powder layer (ρ_{layer}) is controlled by powder characteristics and other system parameters, including recoating design and speed, gas flow, bed temperature, and the shape and gap of the recoating blade, as well as the degree of adhesion caused by surface oxidation and contamination. At very fine particle sizes (d $<$ 17 μm), adhesive forces may exceed gravitational forces, causing smaller particles to adhere to larger particles and thereby reducing spread. For this reason, practitioners control various powder traits, including morphology, $d_{10}/d_{50}/d_{90}$, hollow-particle ratio, apparent and tap density, specific surface area, inclusions, and rheological measures to optimize flow and packing for PBF and DED. Here, D_{10}, D_{50}, and D_{90} represent the particle diameters below which 10%, 50%, and 90% of the particle size distribution fall, respectively. Surface oxides on powder particles affect both adhesion and agglomeration. Thus, in addition to O/N/C pickup and oxide-film properties, the surface oxidation state becomes critical during recycling or when relative humidity and temperature change [73,74].

Key findings from Elambasseril et al. [75] were that most conventional morphological or rheological metrics, including percent of each morphology, apparent/tap densities, and their ratio, angle of repose, avalanche angle, and generic flowability scores, did not determine L-PBF performance. Similarly, even high percentages of highly spherical particles did not consistently improve performance. Instead, the number of fines played a stronger role because it controlled the packing of the powder layer. In that study, 30 wt% fine-particle content optimized the ρlayer, minimized the onset of agglomeration, and helped maintain sufficient fines during recycling, stabilizing build quality across multiple runs. As such, the emphasis has shifted from achieving perfect sphericity to engineering PSD, particularly the fines fraction, while also monitoring the oxide and contamination states that drive powder adhesion. These results indicate that powder quality for L-PBF should not be judged from particle sphericity alone. Instead, the fines fraction, layer density, surface oxide state, and process-specific spreading behavior must be evaluated together when selecting or recycling powders for in situ alloying [73].

From the perspective of in situ alloying, powder size, shape, and purity are not only feedstock-quality parameters, but also control the uniformity of alloy formation. Differences in particle size and morphology between blended constituents can affect spreading, packing, and segregation, while surface oxides and contamination can modify absorptance, adhesion, and the formation of inclusions. Therefore, suitable powder selection for in situ alloying requires compatibility between the blended powders, not only good flowability or high sphericity of each powder considered separately.

3.2. Thermophysical mismatch and alloy design metrics

In in-situ alloying, thermophysical mismatches across constituents, such as melting point, heat capacity, enthalpy of fusion, reflectivity, density, and viscosity, govern how powders absorb energy, melt, mix, and finally solidify. Elemental blends with disparate density and shape can segregate during flow, biasing local composition [76]. Large melting-point gaps can lead to unmelted high-temperature particles if those particles are oversized for the chosen window [74], while absorption contrasts in mixed powders can drive macrosegregation and shift melt and solidification modes [46]. Even when all constituents melt, differences in liquid density and viscosity hinder complete homogenization [77]. Inside the L-PBF pool, Marangoni flow does mix vigorously, yet small pools and rapid cooling preserve traces of chaotic mixing. Consequently, parameter control becomes the direct lever for intermixing, and studies report that, within a suitable processing window, increasing the laser energy input can alleviate composition inhomogeneity [78].

To describe solute effects during solidification, Fan et al. [28] reviewed the commonly used growth restriction factor, Q, which is expressed for a binary alloy as $Q = mC_0(k\text{-}1)$, where m is the liquidus slope, C_0 is the solute concentration in the alloy melt, and k is the equilibrium solute partition coefficient. For multicomponent alloys, Q is often estimated by linearly adding the binary contributions.

$$Q = \sum_{i=1}^{n} m_i C_{0i}(k_i - 1) \tag{6}$$

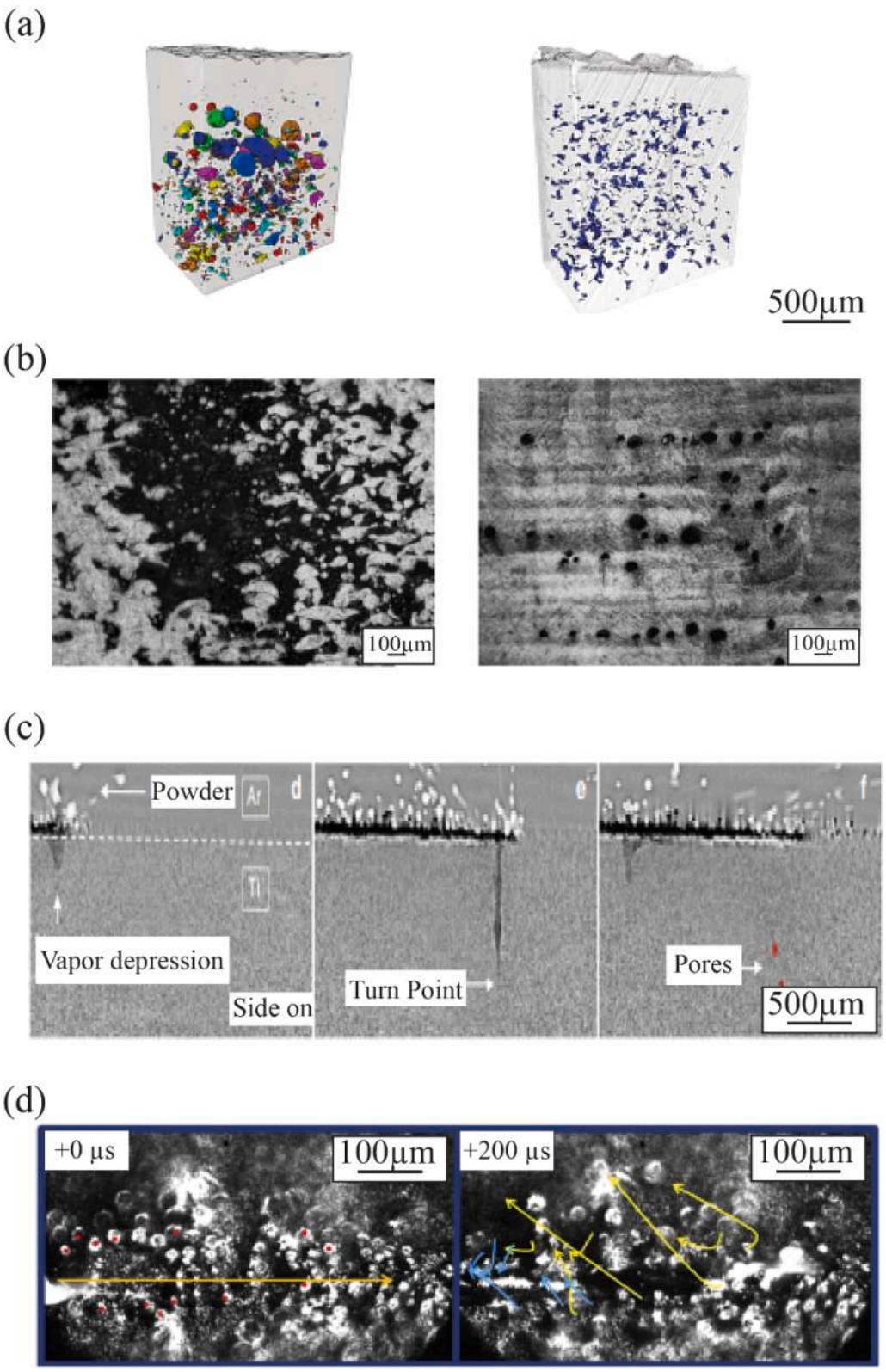


Fig. 7. Representative defects and powder bed instabilities in Ti-6Al-4V powder bed fusion. (a) Synchrotron X-ray microtomography images showing keyhole porosity, left, and lack of fusion defects, right, under different L-PBF processing conditions [67]. (b) Cross-section micrographs showing pore morphology under insufficient energy input, left, and excessive energy input, right, in L-PBF Ti-6Al-4V [68]. (c) In situ X-ray images of keyhole pore formation near a laser turn point during L-PBF of Ti-6Al-4V, shown from left to right as vapor depression formation, turn point region, and pore formation [69]. (d) High-speed imaging of powder motion around the melt track in a Ti64 powder bed, showing particle entrainment at + 0 μs and particle ejection and redistribution at + 200 μs during denudation [71].

However, Fan et al. showed that growth velocity is not a unique function of Q, because growth restriction also depends on the solute partition coefficient and the imposed undercooling. To address this limitation, they proposed a new growth restriction parameter, β, defined as $\beta = Q/\Delta T\text{-}k$ for binary systems, where ΔT is the undercooling. They further showed that β can also be expressed as the liquid-to-solid fraction ratio, $\beta = f_L/f_S$, and that it provides a more consistent description of growth restriction in multicomponent systems than Q alone. In this framework, growth restriction is not controlled only by solute concentration but by the combined effect of solute type, partitioning behavior, and solidification condition.

3.3. Composition homogeneity

The attainment of uniformity in the composition of an in-situ build is a multistage outcome. It depends on the pre-exposure powder blending stage, the melt pool homogenization stage during scanning, the solidification stage, and the post-build solid-state transformation stage [15]. Therefore, the homogeneity of the final product is influenced by both the initial blend and by how each layer is processed through layer-wise control of the AM build process, including the scan strategy and location-specific melting [79].

During melting, the extent of convective mixing and the dissolution of the various components are determined by several factors, including the size and speed of the laser beam, the energy density, the h, powder-bed absorptivity, the viscosity of the molten metal, the degree of partial melting, and the degree of Marangoni flow [15]. After solidification, chemical leveling at both the track scale and the layer scale depends on the nucleation rate, segregation, the growth morphology of the solidifying material, the cooling rate and superheat of the solidifying material, the Q value of the material, the CET of the material, the shape of the phase diagram for the material, and whether the layers are rescanned. In this sense, the designed scan pattern not only defines the build geometry but also provides the thermal history required to achieve the desired transformation [80].

In-situ alloying is advantageous due to its low cost, ability to create location-specific compositions, and capability to create functionally graded materials via layer-by-layer control, but it also presents technical challenges, including issues with metering dissimilar powders, compatibility between metallic components, and thermophysical incompatibilities that prevent complete mixing [80,81]. Thus, the homogeneity of the in-situ alloyed composition often requires a combination of modifying the melt pool window, including energy input, timing of scans, and overlap of scans, together with additional rescan cycles when necessary and post-build heat treatment to reduce the residual gradients [82].

4. Feedstock preparation for in-situ alloying

Feedstock preparation sets the initial spatial distribution of elements in in situ alloying, and early segregation in blended constituents can translate into local composition bias, uneven energy coupling, and melt pool instability during processing [15]. Fig. 8(a) schematically illustrates conventional powder blending, where differences in constituent size, density, and morphology can permit segregation within the mixture. Preparation routes are therefore judged not only by mixing efficiency, but also by how well they preserve powder handling and printability.

This section compares conventional blending, mechanical alloying (MA), and surface engineering approaches such as satelliting and coating, with emphasis on the trade-off between improved compositional uniformity and the risk of morphological change, contamination, or scale-up complexity. Fig. 8(b) contrasts blending with ball milling, a mechanical approach that can be operated in low-or high-energy regimes to promote stronger guest-host attachment and improved compositional uniformity. Fig. 8(c) shows a solution-based coating route, where coating particles are deposited onto a parent powder to increase local chemical uniformity while largely retaining the parent morphology.

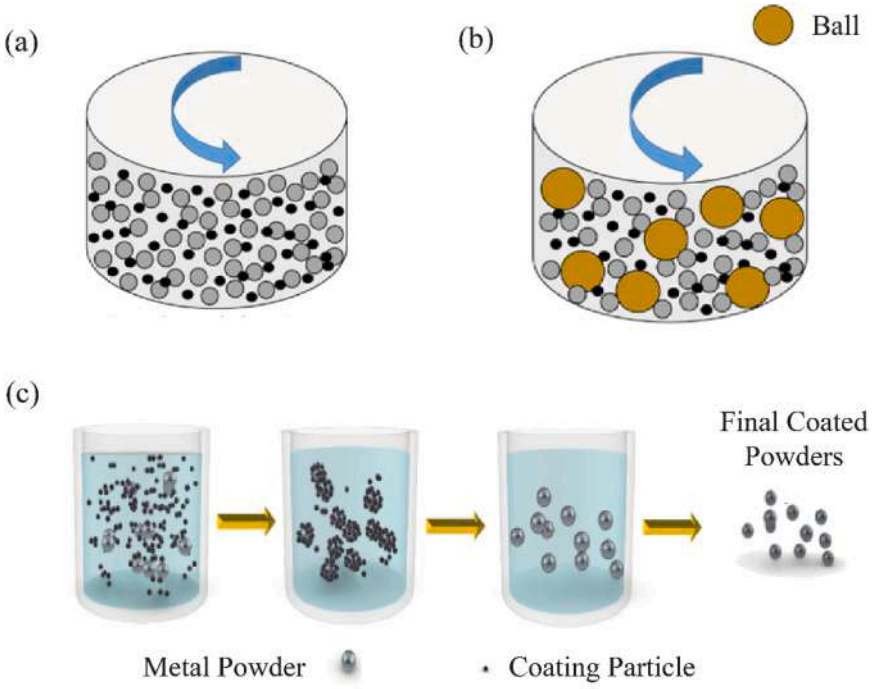


Fig. 8. Feedstock-preparation strategies for in situ alloying: (a) conventional low-energy powder mixing of a powder blend [83], (b) mechanical mixing by ball milling to promote more intimate host-guest contact, and (c) solution-based powder coating in which coating particles are deposited onto a parent metal powder to produce coated feedstock [84].

4.1. Conventional powder blending

Low-energy mixing using tube blenders, tumble mixers, or jars may yield heterogeneous feedstocks due to differences in constituent densities, morphologies, and sizes. Therefore, segregation can occur before laser or beam exposure begins [46]. In practice, these factors interact with AM processing conditions, such as the feeding of dissimilar powders and thermophysical mismatches between constituents, making uneven local energy input an ongoing concern in in-situ alloying. Marangoni convection within the melt pool can facilitate mixing. However, fast solidification and large thermal property contrasts, such as differences in viscosity, density, and melting temperature, can preserve local composition fluctuations after solidification [48]. At the part level, uneven heating of constituents with different thermal conductivities and absorptivities can contribute to macro-segregation, insufficient fusion, porosity, cracking, and distortion [79]. To minimize macro-segregation from the feed stage, powders with narrow PSDs should be used, and the degree of intimate mixing required increases as the beam spot size decreases, making L-PBF particularly sensitive to simple powder blends [46].

Direct mixing of powders is also susceptible to agglomerate formation, which can degrade densification and material properties, especially at higher levels of reinforcing phases [84]. Practical methods to mitigate macro-segregation at the feed stage include pre-heating the powder and/or slightly offsetting the heat source to provide additional heat to high-conductivity phases. Scanning parameters and energy input can also be adjusted to balance melt pool flow and dissolution. Repeated recommendations have been made to model the effects of particle size and morphology on printability to support empirical testing aimed at determining optimal processing conditions. A practical rule of thumb is to adjust the mixing intensity according to the capabilities of the optical system, including spot size and track width, and to verify the feedstock with process-specific measurements of spreadability and effective ρ_{layer} instead of relying only on empirical blending heuristics [79].

4.2. Mechanical alloying

Ball milling or mechanical mixing can be used to prepare more homogeneous blended feedstocks for AM by increasing contact between constituents and reducing segregation. At higher milling intensities, MA can further promote compositional refinement through repeated deformation, fracture, and cold welding. Low- and high-energy ball milling are commonly distinguished by the welding-deformation equilibrium [85,86]. The printability of the feedstock can be controlled by adjusting the ball-to-powder ratio, rotation speed, milling time, and precursor PSD, aiming to balance interfacial reactivity, chemical and microstructural homogeneity, and the retention of sufficient spherical morphology for stable flow and spreading in PBF [84]. A parametric window for milling spherical powders has been proposed to prevent loss of sphericity and provide hardness and morphology targets compatible with laser-based AM [87]. The stored energy introduced during milling can assist melt pool formation and may allow higher scan speeds, thereby reducing the likelihood of unwanted intermetallic formation under optimal conditions [88]. Morphology control of particles with respect to their laser absorptance and the stability of the melt pool, therefore, remains important throughout milling [89].

Powder architecture is equally important. A bimodal PSD can be beneficial when finer particles fill the spaces between coarser particles, since this improves powder bed packing and can support more uniform melting and mixing during in-situ alloying. Ball milling may be used as a deliberate morphology conditioning process for irregular or Hydride-Dehydride (HDH) powders to improve flowability toward behavior closer to that of spherical powders suitable for PBF [90]. High-energy milling also enables nanoscale surface decoration to increase absorptivity and stabilize melt pool dynamics, although achieving a large, uniformly dispersed fraction without compromising spheroidicity has proven to be difficult [79]. Porosity created by gas uptake during milling and defects generated during spreading and/or printing are common risks when utilizing milled feeds. Thus, minimizing gas exposure and optimizing milling severity are crucial before printing [91].

4.3. Satelliting and powder coating

Satelliting and other powder surface engineering techniques attach fine particles or coating materials onto a coarser parent powder to improve local chemical uniformity during in-situ alloying. These approaches can form discrete satellite particles, an outer decorated layer, or a thin coating shell around the parent powder, while maintaining the coarser spherical-particle structure that supports smooth spreading and more consistent laser-powder interaction in AM [15]. Satelliting methods can include wet-binder satelliting using Polyvinyl Alcohol (PVA), electroless plating, electrostatic self-assembly, and fluidized-bed chemical vapor deposition (FB-CVD). These routes provide more controlled attachment or coating without requiring complete alloying of the blended powder before printing [79].

There are limitations to all these methods, however. For example, when using a binder as the satellite medium, there must be sufficient binding strength to maintain satellite particles on the surface of the parent particles, but the binder content should not be so high that it causes satellite-particle aggregation or impedes flow and recoating. Additionally, the geometry and particle size contrast influence how well the satellite particles distribute on the surface of the parent particles. The detachment force required to remove satellite particles from the parent surface can also influence the ability to use this type of satellited feedstock in certain L-DED configurations [15].

Methods used to create coatings, such as electroless plating and FB-CVD, can yield more even coatings, although their practical scale-up depends on factors such as bath or precursor composition and coating thickness, which can also affect contamination risk and part-to-part variation [79]. When the coating conditions and the particle size distribution of the parent and satellite particles are optimized, surface decoration can enhance homogenization, absorptivity, and printability for in-situ alloying. However, the additional process steps and the potential for issues during scale up need to be justified by improvements in performance and reproducibility [46].

4.4. Comparative homogenization performance and practical considerations of feedstock preparation routes

Direct numerical comparison of homogenization among MA, satelliting, and surface-engineering routes is difficult because the available studies use different material systems and different measures of uniformity. The most reliable comparison is therefore based on the compositional and microstructural indicators reported within each study, while powder-flow and spreading data are considered separately as measures of processability.

For MA, Parsons and Shaik compared simply mixed and high-energy ball-milled AlSi10Mg/TiB_2 feedstocks for L-PBF. The simply mixed powders retained separate AlSi10Mg and TiB_2 particle populations and exhibited a bimodal particle-size distribution. After high-energy milling, TiB_2 was incorporated within the AlSi10Mg particles, and cross-sectional scanning electron microscopy/energy-dispersive X-ray spectroscopy (SEM/EDS) showed a more uniform distribution of the reinforcement within the composite powder particles [92].

The change in feedstock structure was accompanied by improved powder handling. The simply mixed powders containing 16 and 30 wt% TiB_2 did not flow through the Hall funnel, whereas the ball-milled powders tested in the study exhibited measurable Hall flow. The simply mixed feedstock also clumped during recoating, while the ball-milled powders could be spread into 30 μm layers.

For satelliting, Simonelli et al. [46] compared simply mixed and satellited Ti-Al-V feedstocks for in situ Ti-6Al-4V fabrication by L-PBF. In

the sample produced from the simply mixed feedstock, the α/α′ matrix contained approximately 0.5–7 wt% Al and 0.4–1 wt% V, while segregated regions contained 15–25 wt% Al or 10–25 wt% V. In the satellited condition, the matrix composition was closer to the target Ti-6Al-4V composition, with approximately 3–5 wt% Al and 2–3.4 wt% V. Severe elemental segregation was nevertheless still observed in the satellited sample.

A similar effect was reported for L-DED of Ti-6Al-4V/TiB_2, where Farayibi et al. [93] observed a relatively uniform distribution of TiB reinforcement and reported improved microstructural homogeneity compared with the simply mixed condition presented in their earlier work.

Since the comparison was based on an earlier study performed under different processing conditions, it is considered supporting rather than direct quantitative evidence.

Surface engineering has also been used to improve the distribution of fine additions without intensive mechanical milling. Zhang et al. [94] compared conventional mechanical mixing with an alternating-adsorption surface-engineering method for Ti-6Al-4V/CP-Ti feedstock containing Fe_2O_3 nanoparticles. The mechanically mixed powder showed pronounced Fe_2O_3 agglomeration, whereas the surface-engineered feedstock exhibited a much more uniform distribution of Fe_2O_3 on the surfaces of individual Ti particles, as shown by SEM and EDS mapping. In this study, the improvement was demonstrated through spatial distribution rather than through a numerical homogeneity parameter.

Taken together, the available studies show that MA, satelliting, and surface engineering can all improve the distribution of secondary constituents compared with simple mixing, but the degree of improvement is reported using different measures. For this reason, the available data support a route-by-route comparison rather than a single numerical ranking of homogenization efficiency.

Beyond the cost of the starting powders, the different feedstock-preparation routes involve different processing requirements that should also be considered when assessing their practical implementation. The study by Zhang et al. [94] illustrates this difference between conventional mixing and surface engineering. The mechanically mixed Ti-based feedstock was prepared using 60 min of tubular mixing, whereas the surface-engineering route involved repeated adsorption and rinsing steps, mixing in an Fe_2O_3 suspension, and more than 10 h of vacuum drying.

For ball milling, Wang et al. [95] used 4 h of planetary milling under Ar with periodic pauses and air cooling and showed that excessive milling caused particle deformation, cold welding, and deterioration of powder spreading. These results highlight the need to carefully control milling conditions when preparing feedstocks for AM.

Tan et al. described satelliting as a rapid and low-cost feedstock-preparation method, although their Ti-15Mo route still involved 20 min of tubular mixing with an aqueous PVA binder followed by 12 h of vacuum drying [96]. Wet coating can likewise require an additional drying step and may introduce contamination or oxidation concerns [97].

From a practical perspective, comparing the cost and scalability of these feedstock-preparation routes is not straightforward, because their suitability depends on the specific alloy and AM process as well as on factors such as preparation time, equipment and atmosphere requirements, additional drying or post-treatment steps, powder losses, contamination risk, preservation of particle morphology and flowability, reproducibility, and the level of compositional uniformity achieved. The available studies are therefore more useful for identifying the trade-offs associated with each route than for establishing a universal ranking of MA, satelliting, and surface-engineering methods.

5. Solidification and melt pool dynamics

The rapid-solidification regime in metal AM results in high cooling rates and fast liquid-solid interface velocities, leading to large deviations from equilibrium conditions. In addition, because the heat source moves, each track or layer experiences a unique thermal cycle along its length. Therefore, the resulting solidification conditions and build features, including microstructure, residual stress, and distortion, are controlled by the transient, three-dimensional temperature distribution in the part [48]. This thermal history is analogous to fusion welding, but fusion-based AM also imposes layer-wise reheating, evolving boundary conditions, and process-dependent melt pool sizes that can shift both mixing efficiency and solidification mode even within a single build.

As a result, for in-situ alloying, melt pool mixing and fluid dynamics play key roles, since under non-equilibrium solidification, solute can be trapped or redistributed when the solid-liquid interface velocity is high relative to solute diffusion in the liquid, creating localized composition variations and the potential for phase formation. Therefore, solidification morphology, including planar, cellular, and dendritic growth, together with macrostructure, CET, Q, and the governing phase diagram, determines how uniformly an alloy composition is created during printing [15]. Accordingly, the following subsections connect thermal-field descriptors, including the gradient G and R, alloy-design metrics such as Q and related undercooling criteria, and melt-pool convection via Marangoni flow to CET mechanisms. The discussion then extends to segregation, cracking tendency, and residual-stress development under repeated thermal cycling.

5.1. Solidification and modeling frameworks

Transient heat flow under a moving source determines the local G and R, which govern interface morphology through constitutional supercooling. Grain selection in AM can be framed in G-R space [50]. As shown schematically in Fig. 9, solidification mode can be organized in G-R space, where the G/R ratio separates planar/cellular/columnar-to-equiaxed regimes, and $G{\times}R$ is associated with structure fineness through its link to cooling rate. Hunt's equiaxed criterion links a critical G to the available nucleation site density and undercoolings, so equiaxed formation is promoted when the attainable undercooling increases through solute redistribution while G is not excessively high. In titanium systems, this is often expressed through the growth-restriction framework, where $\Delta T \propto (Q{\cdot}R)^{1/2}$. Thus, higher Q or

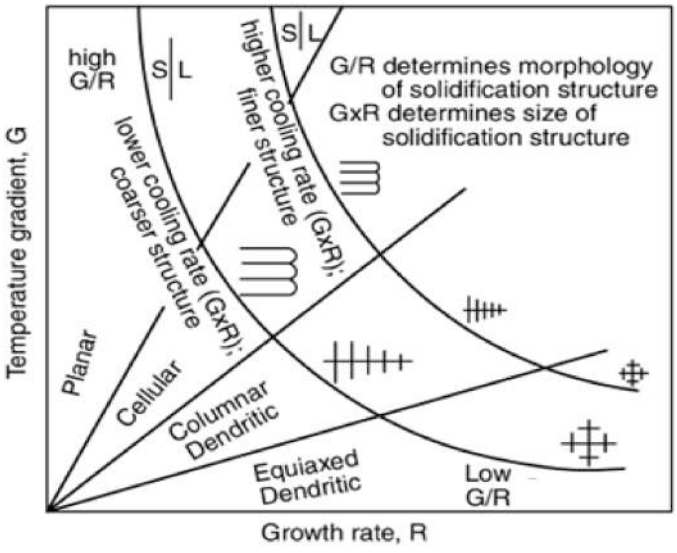


Fig. 9. Schematic G-R solidification map showing microstructure selection as a function of G and R. The G/R ratio is associated with the transition among planar, cellular, columnar dendritic, and equiaxed dendritic morphologies, while $G{\times}R$, corresponding to cooling rate, is associated with solidification structure fineness [101].

higher R favors equiaxed grains, whereas very high G stabilizes columnar growth [16]. Practically, G-R maps collate these regimes and allow AM data to be superimposed to interpret observed morphologies across processing windows.

Modeling tools formalize this picture. The classic Hunt model provides the equiaxed threshold, while the Gäumann-Kurz modification recasts it as a G^n/R condition that highlights how, under AM very high G, nucleation site density N_0 becomes rate-controlling, and the required nucleation undercooling can be neglected to first order [29]. Extensions to multicomponent alloys retain predictive power and have been validated by constructing solidification microstructure maps in Ti-6Al-4V, tying measured transitions to positions in G-R space [50]. These extensions remain useful for identifying solidification trends, but they do not yet provide a complete description of in-situ AM solidification. Ti-based studies show that coupling thermal and fluid fields with solute transport requires simplifying assumptions associated with the different physical scales and computational requirements [98], while far-from-equilibrium microstructure models may additionally require system-specific calibration and validation [99].

Composition provides the complementary lever via Q, which quantifies how the solute establishes a constitutionally undercooled zone that favors CET and grain refinement [29]. In practice, Q can be estimated from Scheil analysis by evaluating the initial slope of the solidification temperature interval with respect to solid fraction f_s, providing a practical metric to compare solute choices for equiaxed propensity [100]:

$$Q = \left(\frac{\partial(\Delta T_s)}{\partial f_s}\right)_{f_s \to 0} \tag{7}$$

This Scheil-based form is useful for multicomponent alloys, while the simplified binary expression clarifies the physical dependence of Q on solute properties. Because Q is commonly related to the liquidus slope, solute concentration, and partition coefficient, as expressed in simplified form by $Q = mC_0(k\text{-}1)$ [28], choosing solutes with larger $m(k\text{-}1)$ can increase growth restriction and, together with suitable R and manageable G, shift AM solidification toward more equiaxed microstructures during in-situ alloying [16]. However, Q should be used mainly as a first screening metric, since growth restriction is also affected by solute partitioning behavior and the imposed undercooling [28].

5.2. Mixing enthalpy and freezing range effects

Exothermic enthalpy of mixing can contribute localized heat during in-situ alloying, assisting interdiffusion and, in some cases, lowering the external laser energy needed. However, this effect is confined to the reaction zones and is only one factor, alongside melting point, reflectivity, and heat capacity, in determining the critical energy input [102]. Its impact also couples to constitutional undercooling. When composition and transport raise the attainable ΔT, the alloy is more likely to meet equiaxed conditions provided the thermal field does not push G/R beyond the stability limit.

The freezing range, ΔT, therefore requires careful control. If it is too narrow, the alloy may have limited constitutional undercooling and reduced tendency for grain refinement. If it is too wide, the extended mushy zone can increase susceptibility to solidification cracking [31]. A compact criterion for constitutional undercooling is:

$$\frac{G}{R} < \frac{m\, c_0\, (1-k)}{D_L\, k} = \frac{\Delta T}{D_L} \tag{8}$$

where G and R are the temperature gradient and solid-liquid interface rate, respectively, m is the liquidus slope, C_0 is the solute content, k is the partition coefficient, D_L is the liquid diffusivity, and ΔT is the solidification range. Satisfying this inequality indicates that constitutional undercooling can develop ahead of the solid-liquid interface, which supports CET and grain refinement when suitable nucleation conditions are present during laser additive manufacturing (LAM) [103].

Freezing shrinkage can also contribute to cavity formation when the volume change accompanying solidification is not compensated by feeding of the remaining liquid. Wang et al. [104] investigated freezing shrinkage through in-orbit solidification experiments on eutectic Nb82.7Si17.3 and hypoeutectic Zr64V36 refractory alloy droplets under microgravity. Their experiments and simulations showed that when growing solid regions contact each other and isolate residual liquid, continued solidification reduces the volume of the separated liquid region and can produce shrinkage cavities. They further identified nucleation and crystal growth velocity as dominant factors affecting the differences in solidification and shrinkage patterns observed between the two alloys. Although these experiments were conducted under container less microgravity conditions rather than AM processing, they provide fundamental evidence of how residual-liquid isolation and solidification shrinkage can generate cavities.

In a fusion-based AM context, Templeton et al. [105] directly investigated shrinkage porosity in L-PBF Alloy 718 and related its formation to volumetric contraction during solidification and insufficient interdendritic liquid feeding. They further showed that shrinkage-pore severity was associated with solidification cooling rate and secondary dendrite arm spacing, while the transition toward cellular growth at higher cooling rates reduced the occurrence of shrinkage porosity.

5.3. Marangoni flow and melt pool mixing

Marangoni convection is driven by surface-tension gradients, which are usually generated by temperature gradients and can also be affected by local composition. This convection strongly controls fluid motion within the AM melt pool and contributes to solute transport during in-situ alloying [48]. Since $d\gamma/dT$ is usually negative for metals, heating in the pool center creates outward surface flow with inward return currents, dragging particles into the pool while increasing mixing and diffusion. As shown in Fig. 10(a-c), Marangoni convection is driven by surface-tension gradients along the melt-pool surface: a negative surface-tension gradient produces outward surface flow with a recirculating return current (Fig. 10(a)), whereas a positive gradient reverses the surface flow and the associated circulation pattern (Fig. 10(b)). Under transitional conditions where the effective gradient changes sign, a mixed flow response can arise (Fig. 10(c)), which helps explain why melt-pool mixing and stability can be sensitive to local thermal and compositional conditions. The Marangoni number can be used to describe the relative strength of this flow [106]:

$$Ma = -\frac{d\gamma}{dT}\frac{L\,\Delta T}{\mu\,\alpha} \tag{9}$$

where $d\gamma/dT$ is the temperature coefficient of surface tension, L is the characteristic length, ΔT is the temperature difference, μ is the dynamic viscosity, and α is the thermal diffusivity.

The behavior of Marangoni convection has also been investigated under microgravity conditions, where natural convection is strongly reduced. Wang et al. [107] studied refractory Nb-Si and Zr-V alloy droplets aboard the China Space Station and reported very weak internal flow under microgravity compared with ground-based levitation. Nevertheless, a thermally induced Marangoni effect was present at the surface of the floating droplet. For Zr64V36, Marangoni convection induced a swirling flow that resulted in spiral microstructures on the alloy surface during the liquid-solid phase transition.

In a Ti-based AM context, Iantaffi et al. [108] used in situ synchrotron X-ray imaging to examine melt-pool behavior during L-DED of Ti6242. Under an inert gas chamber, the melt flow was directed outward, whereas under localized shielding gas conditions, increased oxygen uptake changed the temperature coefficient of surface tension and reversed the Marangoni flow toward the center of the melt pool. The authors attributed this reversal to dissolved oxygen species acting as surface-active elements. The change in flow direction was associated

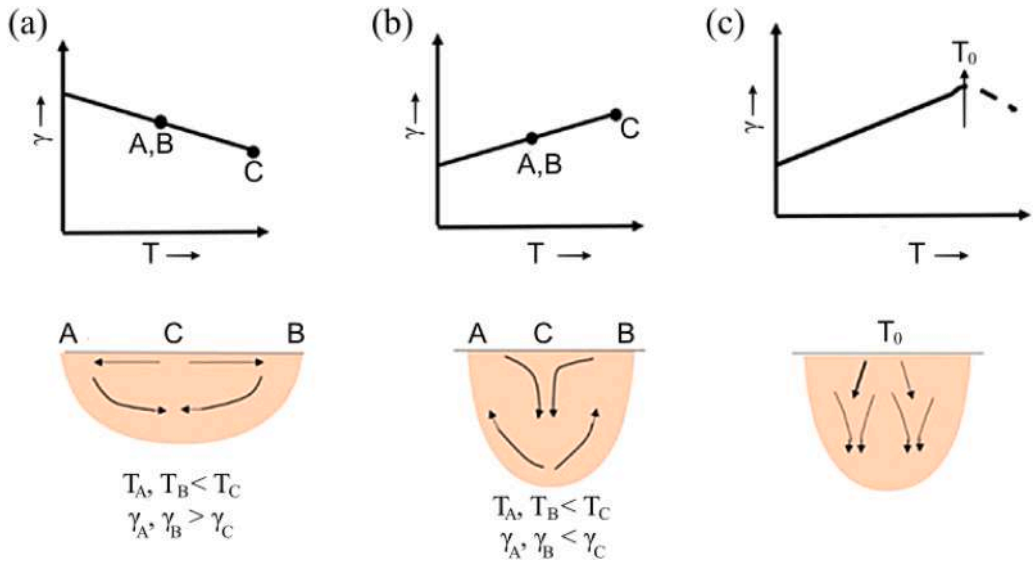


Fig. 10. Schematic Marangoni-flow patterns in a melt pool showing (a) outward surface flow for a negative surface-tension gradient, (b) inward surface flow and reversed circulation for a positive surface-tension gradient, and (c) a transitional case where the effective gradient changes sign, leading to a mixed flow response [110].

with a deeper, more convex melt-pool geometry and changes in pore transport and defect formation.

Direct comparison of L-PBF and L-DED also shows substantial differences in their melt-pool and thermal conditions. Roy et al. [109] reported a much higher travel speed and a considerably smaller melt pool for L-PBF, whereas L-DED exhibited a larger melt pool and a broader range of calculated *G* and *R*. They further described heat transfer in their L-PBF condition as being more strongly conduction dominated, while convection and radiation had a greater influence on the elongated L-DED melt pool.

The flow can modify the melt pool shape and the local *G-R* field, which in turn influence nucleation conditions and grain selection. Composition-dependent surface-tension gradients also affect melt-pool geometry and texture development. Stronger energy input, for example, higher power or lower scan speed, can intensify Marangoni-driven flow and improve mixing, but excessive flow instability may also disturb melt-pool stability and increase defect susceptibility [50].

5.4. CET mechanisms

Solidification processing to produce equiaxed structures in AM titanium alloys is sought to reduce or eliminate the epitaxial columnar β textures resulting from high thermal gradient rates and very rapid solidification. However, controlling process parameters such as *v*, *h*, and energy often only shortens or modifies columnar grains rather than producing a fully equiaxed grain structure, especially when thermal control is not coupled with nucleation and grain-size design. In practice, CET is promoted by reducing the advantage of epitaxial growth and increasing the probability of new grain formation ahead of the advancing front, primarily through changes in local thermal conditions and the availability of heterogeneous nucleation sites [16]. As shown in Fig. 11, measured or simulated processing conditions can traverse a CET transition band, and the plotted points illustrate how relatively small shifts in local thermal conditions can move solidification from columnar growth into a mixed regime and ultimately toward equiaxed grains.

When viewed collectively, process-based mechanisms for solidification closely align with observed microstructural transitions. When increasing heat input in a controlled manner (for example, by increasing power input while maintaining constant speed), the near-surface zone may exhibit a lower *G/R* ratio, creating regions with both mixed and equiaxed grain structures. Similarly, when heat accumulates within a

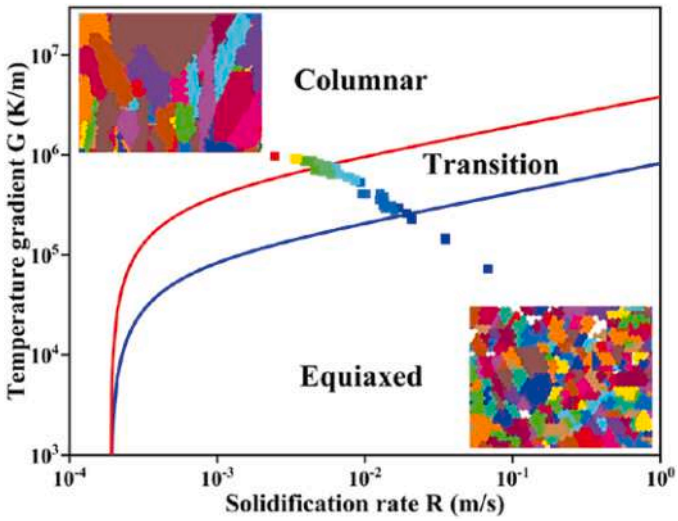


Fig. 11. *G-R* CET map showing columnar, transition, and equiaxed regimes as a function of *G* and R, with representative microstructure insets and data points crossing the transition band [114].

deposited material due to decreasing *t* and/or increased interlayer dwell times, the process shifts from directional solidification to CET, driven by changes in local gradients [40,111]. Conversely, applying less energy per unit area or feeding excess powder onto the bed can increase porosity and other defects, including LOF and delamination; therefore, CET must be achieved while maintaining print-quality operating windows.

Process parameters that affect microstructure formation operate through two complementary mechanisms, nucleation and fluid flow. The use of in-situ alloying, which increases *Q* and the number of potential nucleation sites, together with control of scan strategy, heat-flux modulation, and Marangoni-driven melt mixing, can reduce the probability of epitaxial growth and increase the probability of heterogeneous nucleation. When possible, additional external stimuli (such as high-intensity ultrasonic radiation) can activate nucleation sites during L-DED to provide CET without significant changes to base-processing parameters, while simulation can be utilized to guide processing

conditions toward equiaxed solidification regimes before initiating deposition [50,112].

Roy et al. [109] directly compared solidification morphology and CET prediction in L-PBF and L-DED using the same low-alloy martensitic steel and modeling framework. In their study, L-PBF occupied the higher end of the solidification growth-rate spectrum and exhibited an exclusively cellular morphology in the examined melt pool, whereas the larger L-DED melt pool covered a broader range of *G* and *R* and exhibited solidification morphologies ranging from planar to equiaxed. The conventional Kurz-Giovanola-Trivedi (KGT) treatment, based on constitutional undercooling, did not correctly predict the L-PBF microstructure at high growth rates. Their instability-modified framework incorporated growth-rate-dependent thermal, radial, kinetic, and constitutional undercooling contributions, together with solidification-front instability and solute-trapping effects, and provided better agreement with the experimentally observed L-PBF morphology.

For Ti-6Al-4V L-DED, Chen et al. [113] found that most of the calculated *G* and *R* values for both the stable liquid-bridge and stable wire-penetration modes fell within the mixed columnar/equiaxed region of the Ti-6Al-4V solidification map. Experimentally, however, near-fully equiaxed prior-β grains of about 200–300 μm were obtained only under the stable wire-penetration mode. Their thermal-fluid model showed a mushy zone containing unmelted coaxially fed wire, which the authors proposed could serve as heterogeneous nucleation particles and trigger CET.

5.5. Segregation and residual stress

The compositional versatility enabled by in-situ alloying during fusion-based additive manufacturing comes with an inherent trade-off. If the supplied energy does not fully dissolve high-melting-point additives, such as Mo, during layer formation, compositional segregation can develop within a layer and persist as the build progresses. Gradients formed across successive melt pool boundaries further increase microstructural contrast due to differences in composition and local thermal history, leading to bands of variability along the build direction. As shown in Fig. 12(a), segregation can persist at the melt-pool/track scale, where compositional contrast appears as localized enrichment patterns in elemental maps, indicating incomplete mixing and chemical non-uniformity retained after rapid solidification. In essence, these heterogeneities arise from insufficient energy input and/or inadequate mixing within the transient melt pool. Additive-rich residues from previous passes may then act as preferential sites for compositional or texture non-uniformities in subsequent layers [40].

Alongside chemical heterogeneity, the same repeated thermal cycling that controls solidification also contributes to the development of residual stress. Residual stress accumulates due to steep thermal gradients and the inherent cyclic reheating of layer-wise deposition.

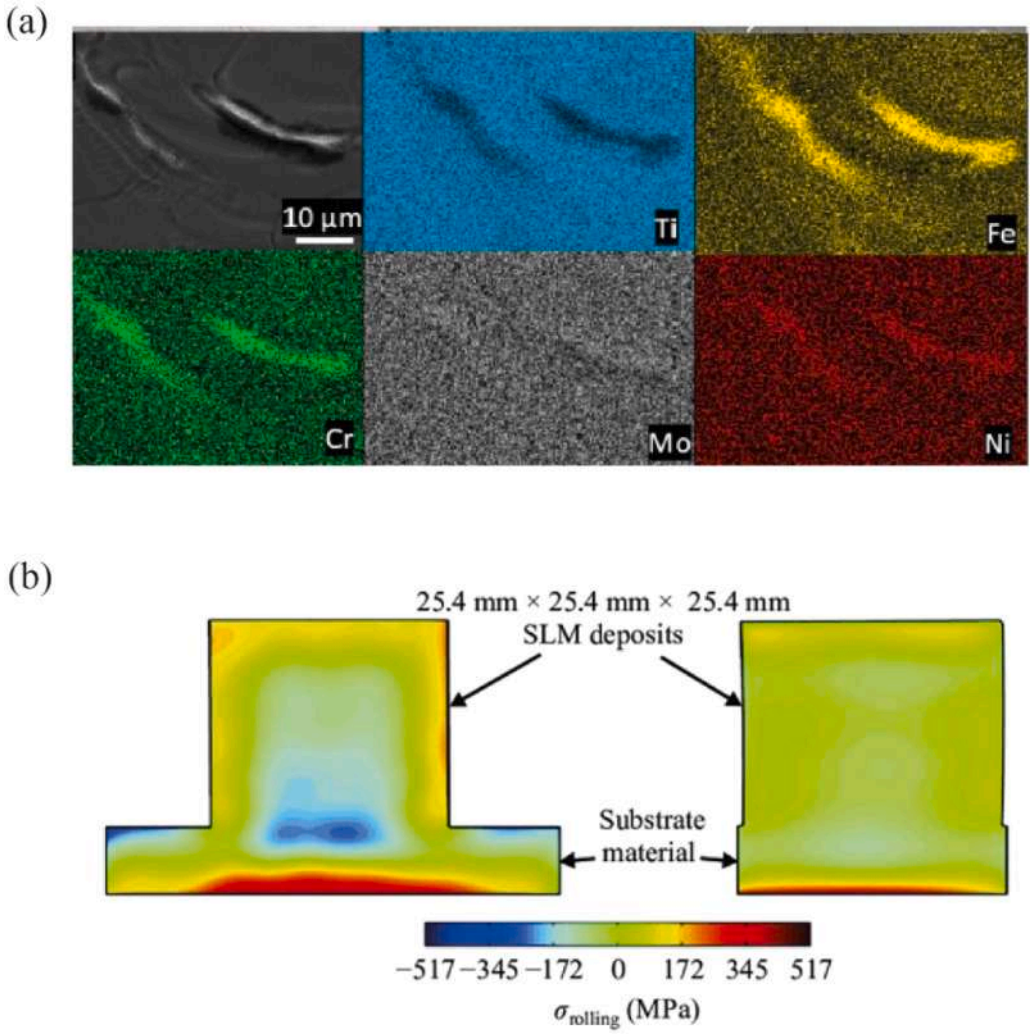


Fig. 12. (a) Example of track-scale compositional non-uniformity illustrated by a SEM image with corresponding elemental maps, highlighting segregation patterns retained after melting and rapid solidification [116] (b) Residual stress of L-PBF-fabricated Ti-6Al-4V measured via the contour method in the rolling direction of the substrate, comparing specimens built on a large substrate with an overhang (left) and on a small substrate without an overhang (right) [117].

Temperature fluctuations induce thermal strain $(\varepsilon_T) = \alpha(T - T_o)$, and plastic accommodation during cooling can lock in residual stresses. Fig. 12(b) shows residual stress in an L-PBF-fabricated Ti-6Al-4V deposit measured by the contour method, reported in the rolling direction of the substrate, highlighting the difference between builds produced on a large substrate with an overhang and on a smaller substrate without an overhang. Processes characterized by large temperature gradients and rapid cooling rates tend to exhibit higher residual stress magnitudes [48].

Hot-cracking susceptibility can be evaluated using the HCS metric:

$$HCS = \frac{t_{f_s \to 0.9} - t_{f_s \to 1.0}}{t_{f_s \to 0.4} - t_{f_s \to 0.9}} \quad (10)$$

This index quantifies the relative duration of the final stage of solidification, during which thin liquid films between grains are prone to tearing under tensile strain. The denominator represents the time spent traversing the broader mushy region (from 40% to 90% solid fraction), while the numerator captures the critical terminal interval (90–100% solidified). Lower HCS values generally indicate improved resistance to solidification cracking. However, strategies that enhance grain refinement, such as increasing growth restriction through alloying additions, may simultaneously broaden the solidification range. Consequently, an optimal balance between alloy chemistry and processing conditions must be achieved to ensure both structural integrity and the desired grain morphology [115].

6. Microstructure evolution and property relationships in in-situ alloyed Ti systems

In the last few years, in-situ alloying has become an important approach to change the microstructure and properties of Ti and Ti alloys during advanced processing techniques such as AM. In particular, the use of additional elemental powders, which are introduced during processing and incorporated into the melt pool, is increasing alongside pre-alloyed feedstocks. This can alter the phase stability and may enhance the strength of materials, refine the grain structure, and regulate solidification both locally within the melt pool and across layers or build height [15].

During laser-based AM of Ti alloys, the molten pool undergoes extremely steep thermal gradients of 10^5-10^6 K m^{-1} and rapid solidification rates of 10^3-10^6 K s^{-1}, depending on the process and parameters. These conditions often promote the formation of metastable martensitic α' rather than equilibrium $\alpha + \beta$ microstructures [16]. The α' phase, commonly observed in rapidly cooled Ti alloys, results from a diffusionless transformation during rapid cooling and is generally associated with high hardness and reduced ductility, which can also affect fatigue performance [50,118]. Consequently, the introduction of appropriate β-stabilizing solutes is often required when ductility is targeted to suppress the α' transformation, refine the prior-β grain structure, and promote the retention of ductile β or $\alpha + \beta$ dual-phase morphologies under the extreme solidification conditions typical of AM [50,118,119].

The alloy systems discussed below can be interpreted using the integrated phase-stability and solidification framework introduced in Section 1.1. Accordingly, the following sections first address the isomorphous β-stabilizers, which exhibit high solubility in Ti and generally stabilize the β phase without forming brittle intermetallics at typical compositions [118,119]. Next, the influence of neutral elements such as Zr and reactive elements such as B is discussed for their roles in preserving ductility and promoting grain refinement via in-situ TiB formation [118,120]. Finally, the focus shifts to the eutectoid β-stabilizers, which can promote constitutional supercooling and CET in Ti alloys [16,79,121].

6.1. In-situ Ti-alloying with isomorphous β-stabilizers

Molybdenum (Mo), niobium (Nb), tantalum (Ta), and tungsten (W) are commonly used as isomorphous β-stabilizing additions in the in-situ alloying of Ti alloys [119]. These elements show high solid solubility in Ti and generally avoid extensive brittle intermetallic formation at typical alloying levels. However, their high melting points, density mismatch with Ti, and repeated thermal cycling during AM can make complete dissolution and chemical homogenization difficult [122].

6.1.1. Ti-Mo

Ti-Mo alloys are strong contenders for replacing Ti-6Al-4V in medical implant materials because they are biocompatible, highly ductile, and have an E modulus close to that of cortical bone. These advantages arise from the dominant β-Ti phase, which reduces stress shielding and provides good mechanical compatibility. The use of Mo, which is a strong β-stabilizer, also effectively lowers the β-transus temperature and limits the formation of martensitic α'. In-situ alloying by L-PBF enables the inexpensive manufacture of Ti-Mo alloys with varying β-phase fractions for use in implants [119]. The difference in the melting point and densities of Ti and Mo (ΔT_m = 950 °C, ρ_{Mo} = 10.2 vs. ρ_{Ti} = 4.5 g cm^{-3}) gives rise to difficulties in achieving homogeneity, leading to partially melted Mo particles and local segregation. Improved laser energy, powder particle size, and post-heat treatment have progressively developed Ti-Mo alloys from heterogeneous dual-phase structures to complete homogenization of the β-stabilized structure (Fig. 13).

In binary Ti-Mo alloys, the increase in Mo promotes β-phase stability and reduces the amounts of α and α'. At intermediate compositions, the phases α'' and ω appear. The lowest values of E (about 70–90 GPa) are noted at 5–15 wt% Mo [119].

In the earliest in-situ alloying investigation on Ti-Mo by Yadroitsev et al. [77]. Mixed elemental powders of Ti and Mo were employed to fabricate Ti-15 Mo by L-PBF. In the material produced, they found that the coarse Mo powder particles that spread along the melt pool boundaries were incompletely melted, resulting in an inhomogeneous $\alpha + \beta$ matrix with sharp Ti/Mo boundaries. The mechanical properties indicated limited ductility (Ultimate Tensile Strength (UTS) = 894 MPa, Strain (ε) = 2.8%) due to insufficient mixing and weak convective flow during melting. Optical Microscopy (OM) and Backscattered Electron (BSE)-SEM images provided evidence of incomplete alloying and the presence of unmelted Mo clusters, indicating an early stage in the in-situ development of Ti-Mo alloys. The nature of the incomplete melting is well exhibited in Fig. 13(a & b).

This finding was also confirmed by Dzogbewu et al. [123], who produced Ti-15 Mo by means of a similar L-PBF parameter set, establishing the presence of unmelted remaining Mo particles with microhardness values of 410–440 HV and a mixed ductile-brittle fracture morphology, again supporting the need for finer powder and a greater strength of convection of the melt pool.

Subsequent work by Kang et al. [124,125] modified the melt pool dynamics in the L-PBF fabrication of Ti-7.5 wt% Mo (with and without TiC additions). The process resulted in a so-called conchoidal microstructure consisting of intercalating β channels of high Mo concentration and α islands of low Mo concentration, produced by Marangoni convection in the molten pool. Transmission Electron Microscopy (TEM) examination of the Focused Ion Beam (FIB)-prepared lamellae exhibited a well-defined chemical contrast between the two regions. The material exhibited an excellent strength-to-stiffness balance (UTS = 750 MPa, and ε = 9%), surpassing Ti-6Al-4V in matching E for implant applications.

To promote greater homogeneity, Dzogbewu et al. [126] employed fine Mo powders (1 μm) and adopted a double-scan strategy (200 W Power, 100 μm hatch distance, and 1.0 m s^{-1} scan speed) to increase convection in the melt pool. Their SEM/EDS maps of Ti-10Mo showed evidence of complete dissolution of Mo after rescanning, whereas single-scan tracks contained undissolved Mo-rich clusters. The

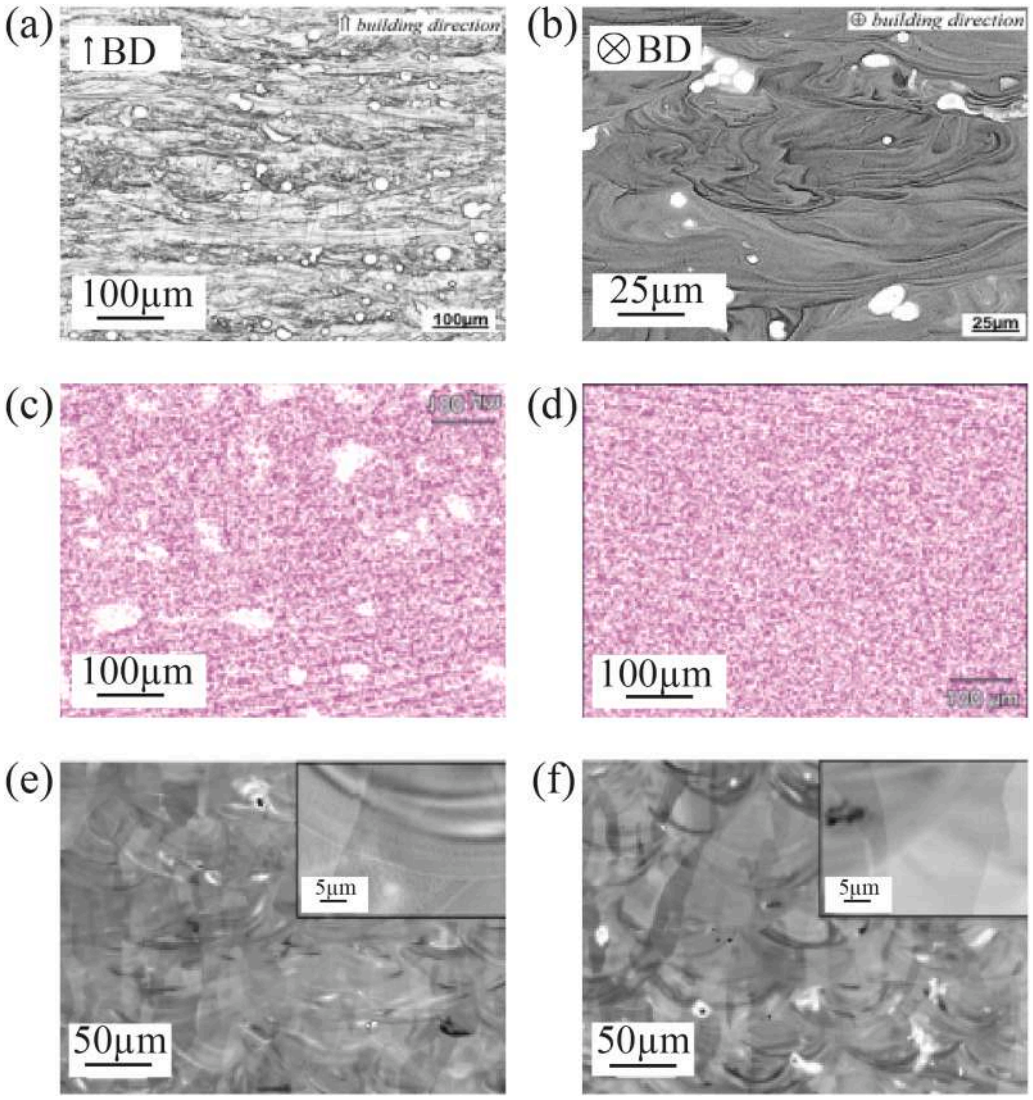


Fig. 13. Microstructural characterization of in-situ Ti-Mo alloys: (a,b) L-PBF Ti-15Mo [77], (c,d) Ti-10Mo after single and double scanning, respectively [126], and (e,f) as-built and heat-treated Ti-12Mo, respectively [130].

optimized samples were practically fully dense (99.7%) with uniform hardness (420–450 HV), demonstrating that repeated scanning effectively leads to complete in-situ alloying and uniform chemical composition. The passage from the single-scan type to the fully homogenized microstructure can be noted in Fig. 13(c & d).

Beyond L-PBF, directed-energy routes provide additional evidence that repeated thermal cycling and build-height-dependent thermal histories strongly affect phase distribution in Ti-Mo alloys. Krajňák et al. [127] made Ti-8.5 Mo by L-DED through in-situ alloying using elemental Ti and Mo powders. The build showed a gradual α to β phase transformation along the height and a hardness gradient from 350 to 500 HV. In the same way, Mantri and Banerjee [128] studied the Laser Engineered Net Shaping (LENS)-processed Ti-12Mo system and showed that columnar β grains with a pronounced ⟨001⟩β texture form along the build axis. The lower parts contain dense α precipitates, which progressively coarsen and decrease in volume fraction as they move towards the top. Electron Backscatter Diffraction (EBSD) analysis revealed twelve Burgers-related α variants in the β matrix, resulting in a weak α texture and demonstrating the significant impact of thermal cycling on variant formation and microstructural anisotropy.

More recently, Ding et al. [129] investigated in-situ L-DED of Ti-5Mo using blended Ti and Mo powders. At low energy input, residual Mo particles remained because of the high melting point of Mo, whereas optimization of the deposition parameters produced samples with a relative density above 99.9%. The optimized alloy consisted mainly of α/α′ phases, with Mo solid-solution strengthening contributing to a yield strength (YS) of 549 ± 30 MPa, UTS of 710 ± 22 MPa, and elongation of 12 ± 2%. This study further shows that L-DED can provide effective in-situ alloying of Ti-Mo, although sufficient energy input remains necessary for complete Mo dissolution.

Duchaussoy et al. [130] investigated the effect of a short heat treatment (900 °C / 90 s + water quenched (WQ)) on L-PBF Ti-12 Mo. As-built, columnar β grains contained fine α″ and ω precipitates, which were responsible for brittleness. After heat treatment, SEM and EBSD examinations revealed the disappearance of metastable phases, resulting in a uniform recrystallized β matrix. The alloy subsequently exhibited markedly increased ductility (ε = 36%) and very high strength (UTS = 820 MPa, YS = 695 MPa), demonstrating that rapid homogenization enabled the coexistence of transformation-induced plasticity/twinning-induced plasticity (TRIP/TWIP) with high strength. The change from the α″-type to the homogeneous β-type microstructure is shown in Fig. 13(e & f). Similar homogenization behavior was also reported by Dai et al. [131], who correlated linear energy density with complete Mo dissolution and enhanced ductility in Ti-10 Mo.

At the same time, Peterson et al. [132] established a link between the energy density applied during the process and the evolution of texture. They showed that decreasing the VED to below 90 J mm^{-3} results in a weakening of the {100}β texture and an alteration of the oriented-to-misoriented transition (OMT), which allows equiaxed β grains to prevail with greater isotropy in Ti-10Mo. This showed, therefore, that a direct relationship is present between the energy density of processing and the structural textural changes produced.

Zhao et al. [133] produced Ti-15Mo containing dispersed ω precipitates that enhanced strength (UTS of 888 MPa) while maintaining 20% elongation *(δ)* through {332}⟨113⟩ twinning.

Moderate Mo content (7–12 wt%), fine powders, and sufficient laser energy yield homogeneous β-stabilized Ti-Mo alloys suitable for use in biomaterials.

6.1.2. Ti-Nb

Nb is one of the most promising non-toxic β-stabilizers for titanium alloys, due to its ability to reduce the β-transus temperature while inhibiting the formation of α′ or ω phases, resulting in a low E and good biocompatibility. As reviewed by Gouthamaraj et al. [118], β Ti-Nb systems in the 20–40 wt% Nb range have E of 45–60 GPa and YS of 600–900 MPa, which are closest to those of cortical bone while retaining good corrosion resistance. Dobrzańska et al. [119] further established, through a five-year bibliometric and heuristic study, that Ti-Nb is by far the most successful in-situ AM system among all β-stabilized Ti alloys, having the most balanced properties of β-phase stabilization, bone-like elasticity, and non-cytotoxicity.

Tang et al. [98] developed the most comprehensive understanding of segregation phenomena in L-PBF Ti-Nb. By combining simulations and experiments on alloys containing 10–41 wt% Nb, they showed that increasing the Nb content changed the melt-pool shape from long-wide-shallow to short-narrow-deep. Simulated maps show that at 10 wt% Nb, Nb-enriched bands form at the edges of the melt pool, whereas in the experimental micrograph, the Nb-enriched bands at 41 wt% Nb are more pronounced. This is due to Marangoni solute partitioning and accounts for the varying composition of the as-built Ti-Nb.

Borgman et al. [134] fabricated Ti-10,20, and 30 wt% Nb alloys by L-PBF for the study of phase transformations at an energy density of 230 J mm^{-3}. Fig. 14(a & b) shows SEM micrographs that reveal the transformation from fine acicular α″ martensite at 20 wt% Nb to a cellular β product at 30 wt% Nb, indicating enhanced Nb diffusion and stabilization of the β phase. YS of 769 MPa, UTS of about 800 MPa, and E of 65 GPa were obtained, indicating that Ti-20Nb appears to be the optimum alloy for biomedical applications.

Zhao et al. [135] engineered Ti-25 Nb by L-PBF using different VED values (70–110 J mm^{-3}). Fig. 14(c & d) shows SEM images at 110 J mm^{-3}, where partial α′ laths coexist with fine β subgrains, allowing the conclusion of partial β stabilization and improved Nb dispersion. YS about 645 MPa, UTS of 700 MPa, and E about 83 GPa were obtained, with improved corrosion resistance due to the formation of Nb_2O_5 on the surface.

Fischer et al. [136] fabricated a β-Ti-Nb alloy by L-PBF, representing the first realization of a homogeneous alloy using elemental Ti + Nb powders (26 Nb). Epitaxial β columns of about 100 μm were obtained, with structures being {001} aligned along the build direction, which confirms the formation of a single β phase directly from elemental powders. The alloy exhibited an E of 77 GPa and a hardness of 266 HV.

In-situ Ti-28.5 Nb and Ti-40.0 Nb alloys were produced by L-PBF, via ball-milled powders of elemental Ti and Nb, respectively, by Singh et al. [137]. The microstructural investigation of the Ti-28.5 Nb showed a two-phase microstructure (β + α″) with a few partially bonded Nb particles, while the Ti-40Nb showed a single-phase β matrix. The mechanical properties of the alloys were commensurate with the phase stability observed: Ti-28.5 Nb exhibited a UTS of 1063 MPa and an E of about 91 GPa, while Ti-40Nb exhibited a UTS of roughly 802 MPa and an E of 81 GPa, which should enhance ductility. The alloys exhibited almost complete densification, featuring non-toxic, well-passivated β surfaces that promoted osteoblast proliferation. It was concluded from the work that Nb could be added in a controlled manner, in-situ by L-PBF, thus providing a direct means of both tuning the β-phase fraction and the mechanical compatibility for orthopedic applications.

Huang et al. [138] studied L-PBF Ti-41Nb prepared from elemental powders. BSE/EBSD mapping shows columnar β grains (about 150 μm) consisting of alternating Nb-poor and Nb-rich lamellae. TEM identified 4 nm isothermal ω precipitates in the β matrix. This microstructure corresponds to high β-stability (E of 75 GPa) but low ΔL, about 41.5%,

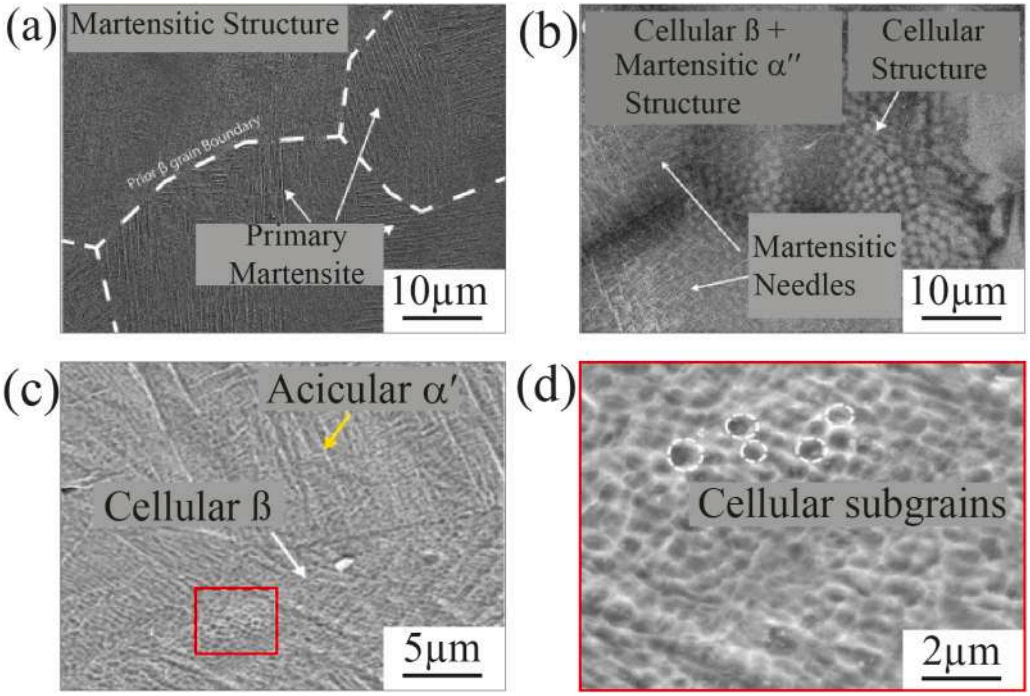


Fig. 14. Representative microstructures of in-situ L-PBF Ti-Nb alloys: (a) Ti-20Nb and (b) Ti-30Nb [134], and (c,d) Ti-25Nb [135].

due to segregation and ω precipitation, which restricts slip.

Recent work has advanced this route further through in-situ L-PBF. Chou et al. [139] studied the effect of thermal rest periods between successive layers during in-situ L-PBF of Ti-41Nb. They found that the solubility, density, and mechanical properties of Nb were considerably affected by this rest time. More extended rest periods increased Nb diffusion and decreased the number of unmelted particles, resulting in a UTS of 1007 MPa and enhanced ΔL.

Further, the stabilization of the β-phase in the in-situ Ti-Nb L-PBF systems has also been demonstrated by Boubaker et al. [140] who fabricated a Ti-42Nb alloy from elemental powders to produce a dense single-phase β microstructure (E = 57 GPa, and YS = 1180 MPa) with a porosity of < 1 vol%. Similarly, Sharkeev et al. [141] fabricated Ti-40Nb by L-PBF of a Ti + Nb composite powder whereby a β + α dual phase structure was produced in which fine α" laths (0.1–0.7 μm) decorated the β grains (5–7 μm) were present. The microhardness was 420–550 HV, confirming fast-solidification hardening. Wang et al. [142] investigated in-situ L-PBF of Ti-35Nb produced from elemental powders and showed that heat treatment at 1000 °C for 24 h (hrs) allowed for the homogenization of the undissolved Nb cores, which resulted in improved ΔL of about 38–47% with E of 85 GPa, with good corrosion resistance due to the formation of a uniform TiO_2-Nb_2O_5 film. Collectively, these works indicate that higher Nb contents, combined with post-build heat treatment when needed, can transform α″/α-containing dual-phase structures into a more stable β matrix. This provides a favorable balance between YS and E, which is particularly relevant for implant applications.

EB-PBF has also been applied to in-situ Ti-Nb alloying. Surmeneva et al. [143] fabricated Ti-10 at% Nb from elemental Ti and Nb powders at a build temperature of 880 °C. Increasing the electron beam energy reduced porosity and the amount of residual Nb, with the higher-energy regions becoming nearly fully dense. Nevertheless, the as-built material still contained partially dissolved Nb cores surrounded by Nb-rich β solid solution and α/β regions, showing that particle size and beam energy remain important for chemical homogenization even under the elevated-temperature conditions of EB-PBF.

Overall, these results show that in-situ AM of Ti-Nb alloys can produce either partially martensitic dual-phase structures at low Nb content or low VED, or fully β-stabilized microstructures at higher Nb contents. Both L-PBF and EB-PBF processes can produce dense, low-E, bioinert Ti-Nb alloys with controllable phase composition.

6.1.3. Ti-Ta

Ta is a highly biocompatible, corrosion-resistant metal with a body-centered cubic structure and an excellent ability to stabilize the β phase, making it an attractive alloying element in titanium-based biomedical alloys. The addition of Ta lowers the β-transus temperature and alters the stability of the phases progressively: α′ martensite and α″ martensite are dominant at concentrations of less than 50 wt% Ta, whereas a stable β phase appears at concentrations above 60 wt% Ta, near the concentration (70 wt%), which gives the material the lowest E of about 67 GPa. In the ternary and quaternary systems of the type of Ti-Nb-Ta and Ti-Nb-Ta-Zr, additions of Ta in small amounts (5–10 wt%) lower the E to about 64–67 GPa by giving stability of the phases and bioactivity due to the spontaneous formation of a protective film of Ta_2O_5 [118].

The excellent specific tensile strength and corrosion resistance of Ti are combined with the biocompatibility and osseointegration of Ta in Ti-Ta alloys, providing a good compromise for load-bearing implants. Cast or forged Ti-Ta alloys that have been used conventionally suffer from elemental segregation due to the significant differences in melting point and density of Ti (1668 °C, 4.5 g cm^{-3}) and Ta (3020 °C, 16.6 g cm^{-3}). These difficulties are overcome by the rapid melting and cooling rates associated with the L-PBF technique, which solves the problem of segregation by allowing Ta to dissolve in-situ in Ti, thus obtaining homogeneous microstructures of the β-stabilized type and ultimately the desired mechanical and biological properties [118].

The mechanical and corrosion characteristics of Ti-xTa (0–25 wt%) were investigated by Zhao et al. [144], who prepared in-situ by L-PBF using ball-milled powders of Ti + Ta. Increasing Ta converted the microstructure from lath α to acicular α′ and finally to a dual α′ + β structure, verifying progressive β-stabilization. The UTS increased from 641 to 1186 MPa, but E reduced from 115 to 89 GPa. Corrosion tests in Ringer's solution showed that Ti-25Ta had the most stable passive film due to the formation of a Ta_2O_5/TiO_2 bilayer and that Ta addition increased β-stability as well as corrosion resistance.

After that, Polozov et al. [145] investigated the in-situ production of Ti-10Ta, Ti-15Ta, and Ti-20Ta alloys by L-PBF. Here, the Ta concentration was correlated with the microstructural and mechanical response. As shown in Fig. 15(a), as-fabricated and Fig. 15(b & c) heat-treated (post-annealing at 1100 °C) Ti-15Ta resulted in a homogeneous lamellar α + β structure, rather than a cellular β network, and improved Ta homogenization, reducing unmelted Ta from 2.9% to 0.8%. Increasing the Ta concentration reduced the E from 118 GPa (Ti-10Ta) to 102 GPa (Ti-20Ta), but Ti-15Ta showed the best combination of UTS and E (UTS of 1.10 GPa, E of 110 GPa). Comparison of triply periodic minimal surface (TPMS) lattices, such as gyroid and schwarz, reduced the E values to 10–19 GPa, which are closer to cortical bone and thus show the biomedical potential of in-situ L-PBF Ti-Ta.

Soroa et al. [146] produced Ti-25Ta in-situ by L-PBF using mixed elemental powders at a power of 95 W and scan speed of 300 mm s^{-1} and obtained almost completely dense parts (99.8%) with 1.2% unmelted Ta. SEM micrographs showed acicular α″ martensite within prior-β grains, with β boundaries wrapping Ta inclusions. This again verifies the β-stabilization in Ti caused by the presence of Ta. The alloy exhibited high compressive ductility (70%) and an E of 73 GPa for compact parts, decreasing to 14–36 GPa in Schwarz-type TPMS scaffolds. This demonstrates the positive retentive effect of Ta on β-phase retention and ductility, making in-situ L-PBF Ti-25Ta a promising candidate for bone-mimetic implants.

Huang et al. [147] systematically examined Ti-Ta (0–10–30–50 wt %) L-PBF-fabricated alloys to establish the composition-phase-property relationships. Higher Ta contents indicate a change from Fig. 15(d) coarse α′ laths (Ti-10Ta) through Fig. 15(e) fine acicular α″ (Ti-30Ta) to Fig. 15(f) equiaxed β grains (Ti-50Ta). From EBSD mappings, texture weakening (multiples of uniform distribution (MUD)16.4–5.4), and grain refinement (3.3–0.05 μm) were obtained due to heterogeneous nucleation from unmelted Ta particles. For Ti-30Ta, the observed properties were a UTS of 860 MPa and an E of around 72 GPa, whereas Ti-50Ta exhibited β-stability and greater ductility. Porous (of 60% porosity) Ti-50Ta scaffolds showed comparable cell viability to cp-Ti and Ti-6Al-4V, thus indicating the biomedical advantage of Ta-induced β-stabilization.

Brodie et al. [82] improved Ti-25Ta homogeneity through a remelt scan technique in the L-PBF process, which enhanced Ta diffusion and reduced texture anisotropy. The remelted sample showed random orientation of α′ plates and minor α″ precipitates near Ta-rich regions, with UTS of 566 MPa and E of 65 GPa, thereby improving mechanical isotropy and the strength-E relationship.

Higher Ta levels have been demonstrated by Sing et al. [148], who produced dense Ti-50Ta in-situ by L-PBF (power of 360 W, and scan speed of 400 mm s^{-1}), showing complete formation of a β(Ti, Ta) solid solution. The microstructure consisted of equiaxed β grains (about 10 μm) with UTS = 924 MPa, YS = 883 MPa, E = 75.8 GPa, and ε = 11.7%, confirming that Ta suppresses the β to α′ transformation and lowers the E without adversely affecting ductility.

Liu et al. [149] furthered this study by producing a Ti-50 wt% Ta alloy by L-PBF to improve fatigue resistance and bioactivity. The high Ta content led to the formation of a fully β(Ti, Ta) matrix with uniformly distributed fine α″ precipitates, which stabilized dislocation motion under cyclic loading. The alloy exhibited an endurance limit of 310 MPa after 10^6 cycles and a low E (about 77 GPa). Electrochemical tests revealed the presence of a stable passive layer composed of Ta_2O_5/TiO_2

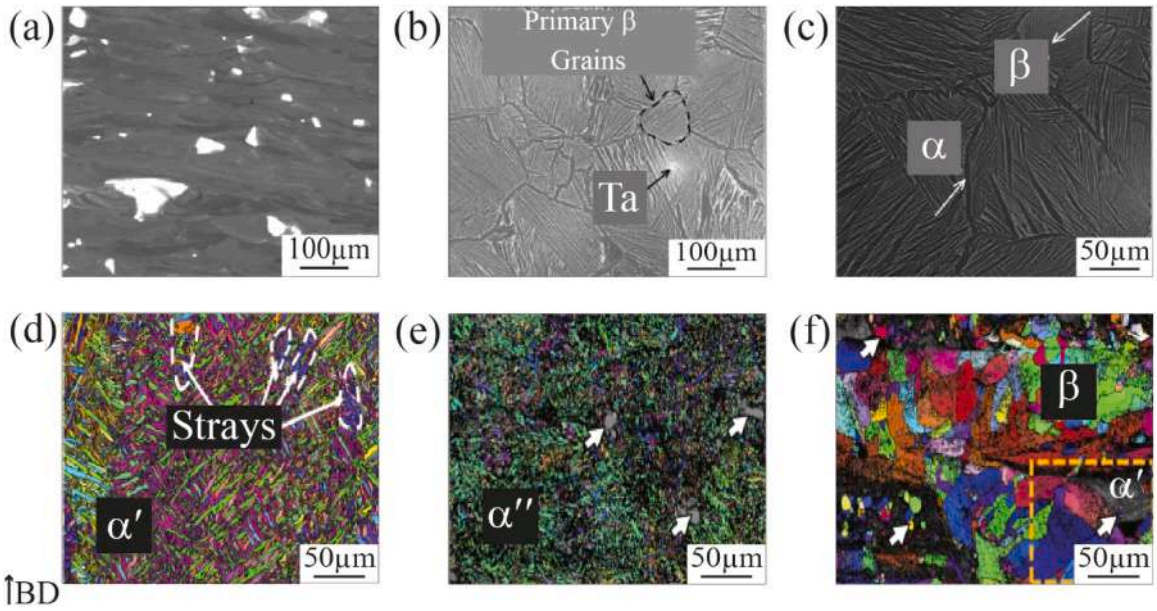


Fig. 15. Microstructural evolution of in-situ L-PBF Ti-Ta alloys: (a) as-fabricated and (b,c) heat-treated Ti-15Ta [145], and EBSD inverse pole figure (IPF)-Z maps of (d) Ti-10Ta, (e) Ti-30Ta, and (f) Ti-50Ta [147].

and excellent cell adhesion, confirming that high-Ta β-Ti alloys manufactured by L-PBF exhibit both long-term fatigue durability and bioactivity.

Huang et al. [147] and Sing et al. [150] showed that an energy density of 144 J mm^{-3} (power of 360 W, scan speed of 400 mm s^{-1}) ensures full melting of Ta and about 99.85% density in Ti-50Ta. X-ray diffraction (XRD) revealed a fully β-type structure, whereas lower energy inputs resulted in unmelted Ta and porosity, defining the process window for dense in-situ Ti-Ta alloys.

Extending beyond bulk samples, Zhao et al. [151] synthesized an in-situ L-PBF Ti-25Ta gyroid structure (about 90% porosity) to couple mechanical integrity and bioactivity. Nanoscale α′ lamellae have been observed in a β matrix by TEM, with an orientation of (102)α′//(200)β and a uniform Ta distribution. The two-phase structure (β subgrain size of 1 μm, α′ of 50 nm) gave YS = 55.5 MPa, E = 1.83 GPa, and elastic admissible strain (EAS) = 3.03%, corresponding to cancellous bone. The naturally produced Ta_2O_5 film promoted apatite formation and osseointegration after 8 weeks, demonstrating the potential of in-situ L-PBF Ti-Ta gyroid scaffolds for next-generation biomedical implants.

Most recently, Xu et al. [79] reviewed the results of in-situ multi--metal alloying in laser-based AM techniques, noting that the Ti-Ta system is an ideal model system for providing fundamental insight into β-phase development under large thermal gradients. They found that Ta Q of 11.2 °C leads to an equiaxed β-grain structure during rapid solidification. Furthermore, advanced process map modeling and ML tools are now being applied to predict Ta dissolution and β fraction directly from the thermal regime of the L-PBF process. Their analysis places in-situ L-PBF Ti-Ta systems as ideal model alloys for future adaptive alloy design in AM-based technologies.

6.1.4. Ti-W

There is increasing interest in W, with strong β-stabilizing tendencies and the ability to cause a CET and refine prior-β grains during laser-based AM [50]. In addition, several studies of conventionally processed Ti-W alloys have shown that W plays a vital role in providing improved oxidation resistance and microstructural stability at elevated temperatures by forming compact oxides and refining α-lamellae [152].

Mendoza et al. [153] studied the microstructural evolution and mechanisms of grain refinement in additively manufactured Ti-xW alloys made via LENS using in-situ alloying of elemental Ti and W powders. A compositionally graded Ti-xW (0–30 wt%) system was fabricated to study the relationship among composition, processing, and microstructure. Increasing the W content decreased the prior-β grain size from > 170 μm to 30 μm at 23 wt% W, without forming intermetallic phases, indicating that W acts as an isomorphous β-stabilizer and grain refiner. The Easton-St John model fits the data with a high Q of 22.65 °C, suggesting a mixed solute- and nuclei-based refinement mechanism. BSE images show that the fine β grains contain α-laths and W-rich zones that stabilize the β phase, as shown in Fig. 16(a-c), increasing W concentration resulted in progressive refinement of the β grains. COMSOL simulations indicate that a higher energy input enlarges the melt pool and reduces the cooling rate (from 6.5×10^3 to 5.6×10^3 K s^{-1}), resulting in slightly coarser grains. Therefore, W is a highly effective grain-refining solute for AM-Ti systems.

Rolchigo et al. [154] extended the experimental observations of Mendoza et al. by developing a multiscale model for the LENS processing of Ti-5.5 wt% W. In this approach, a macroscale COMSOL simulation was used to describe heat transfer and melt-pool flow, including Marangoni convection, while a microscale Lattice Boltzmann-Cellular Automata model captured solute transport and dendritic growth under AM-like conditions (thermal gradients of 10^5-10^6 K m^{-1} and cooling rates of 10^3-10^4 K s^{-1}). The simulations show that the planar solidification front rapidly becomes unstable and transforms into columnar and cellular dendrites, consistent with constitutional undercooling in the Ti-W system.

The simulated microstructures (Fig. 16(d-g)) also indicate that fluid flow perpendicular to the solidification front enhances local solute mixing and leads to asymmetric dendrite arms. The predicted primary dendrite spacing ranges from about 5–15 μm, which agrees well with the compositional oscillations measured by EDS (around 7 μm periodicity). As the cooling rate and thermal gradient increase, the morphology evolves from coarse columnar dendrites (Fig. 16(d); 10 K s^{-1} and 50,000 K m^{-1}) to a mixed columnar-equiaxed structure nucleating from the bulk liquid (Fig. 16(e), 50 K s^{-1} and 50,000 K m^{-1}). Under conditions closer to those typical of the LENS process, finer columnar dendrites appear (Fig. 16(f), 2500 K s^{-1} and 250,000 K m^{-1}), and eventually the structure transitions to columnar cells (Fig. 16(g), 4000 K s^{-1} and 250,000 K m^{-1}). The high partition coefficient of tungsten ($k > 1$), together with its strong growth-restriction effect, plays a key role in promoting grain refinement and stabilizing the β phase in the Ti-W

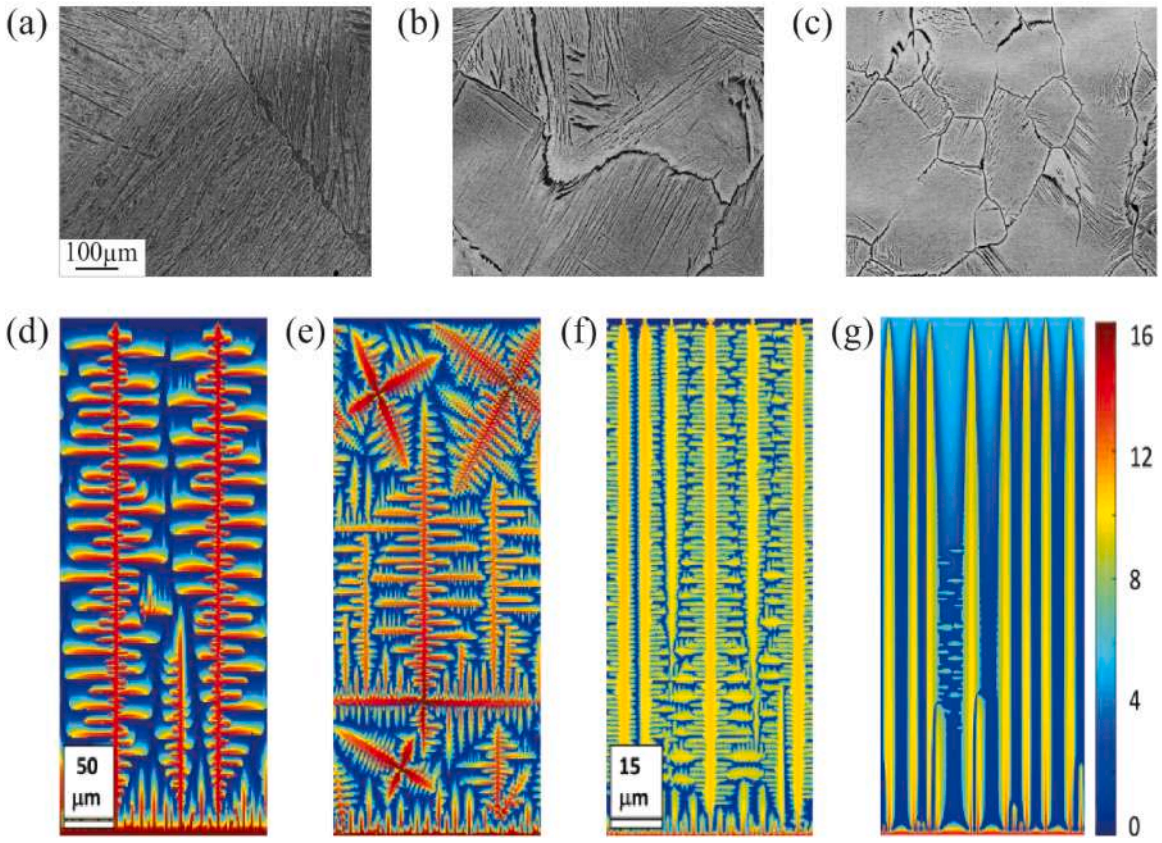


Fig. 16. Microstructural evolution of Ti-W alloys: BSE micrographs of LENS-processed (a) Ti-5W, (b) Ti-13W, and (c) Ti-25W [153]; simulated Ti-5.5 W microstructures at cooling rate/thermal gradient conditions of (d) 10 K s^{-1} /50,000 K m^{-1}, (e) 50 K s^{-1} /50,000 K m^{-1}, (f) 2500 K s^{-1} /250,000 K m^{-1}, and (g) 4000 K s^{-1} /250,000 K m^{-1} [154].

system [154].

6.2. *In-situ Ti-alloying with neutral and reactive additions*

According to the theory of the *Q*, boron (B) is one of the most effective grain-refining solutes in titanium-based alloy systems [50]. Zirconium (Zr) is satisfactorily β-neutral in every respect regarding the previously discussed enhancements in terms of ductility and corrosion resistance, without a significant change in the α-β transus, and should not lead to increased stability of the β phase. However, stability can be easily attained by using Zr, in combination with β-stabilizers, such as Nb, Ta, and Mo [118].

6.2.1. *Ti-(B, TiB, and TiB_2)*

Boron has been studied as a reactive additive to titanium to form in-situ TiB reinforcements, which can refine the microstructure of titanium and its alloys. Due to the extremely low solubility of boron in titanium (0.02 wt%), its rapid reaction with titanium upon melting leads to the formation of TiB with an orthorhombic B27 crystal structure [120,155,156]. The reaction Ti + B → TiB occurs spontaneously because of the highly negative Gibbs free energy (ΔG of 40 kcal mol^{-1}) [157], which prevents boron from remaining in solid solution within the titanium matrix. Consequently, elemental boron can be directly introduced into pure titanium or titanium alloys, where it rapidly forms a network of finely dispersed TiB reinforcements that profoundly influence microstructural evolution and improve mechanical and tribological performance.

One example of in-situ syntheses of TiB by L-PBF was reported by Attar et al. [155], who used a Nd: YAG (Neodymium-doped Yttrium Aluminum Garnet) laser at 165–185 W power and 118–154 mm s^{-1} scan speed to produce 99.5% dense TiB-reinforced titanium composites from a Ti + 5 wt% TiB_2 powder mixture. As shown in Fig. 17(a & b), in different views, TiB whiskers were uniformly distributed within the α-Ti matrix, refining the α-grain size to less than 1 μm. The TiB/Ti composites exhibited a hardness of about 402 HV, YS of 1.1 GPa, and UTS of 1.42 GPa, all markedly higher than those of L-PBF-processed Ti.

Hu et al. [102] further analyzed the in-situ reaction mechanism between titanium and boron during L-PBF of elemental Ti and B powders, combining thermal modeling with experimental verification. Their simulations revealed that the exothermic reaction Ti + B → TiB/TiB_2 initiates at 723 K (well below the melting points of either constituent), confirming that the chemical reaction precedes melting. Using a Yb-fiber laser (λ of 1070 nm, $P \leq 200$ W), they showed that under low energy input (about power of 30 W, and scan speed of 7 m s^{-1}), the process is self-sustaining and forms TiB_2 directly, while excessive power ($P \geq 144$ W, scan speed of 0.53 m s^{-1}) leads to over-melting and partial vaporization due to the reaction's high exothermicity. These results highlighted that the heat released from the Ti-B reaction can effectively supplement the laser energy, but also necessitates precise control of input parameters to avoid instability. This work established selective laser alloying as a thermodynamically viable pathway for in-situ synthesis of Ti-B and TiB_2 in titanium systems.

Mantri et al. [158] investigated in-situ TiB formation in β-type alloys by adding 0.5 wt% B to Ti-20V and Ti-12Mo processed via LENS. Fig. 17 (c-f) displays how the formation of TiB at β-grain boundaries resulted in a reduction in the size of prior-β grains from millimeters to 10–40 μm and eliminated the strong (001)β texture commonly found in AM β titanium alloys. The increase in Q-factor from 29 to 67 °C indicated that B could induce isotropy in metastable β-titanium alloy systems. Additionally, the finer, more equiaxed α precipitates indicated that B improved the microstructure of these alloys.

Ye et al. [159] developed a finite element-based thermal model to

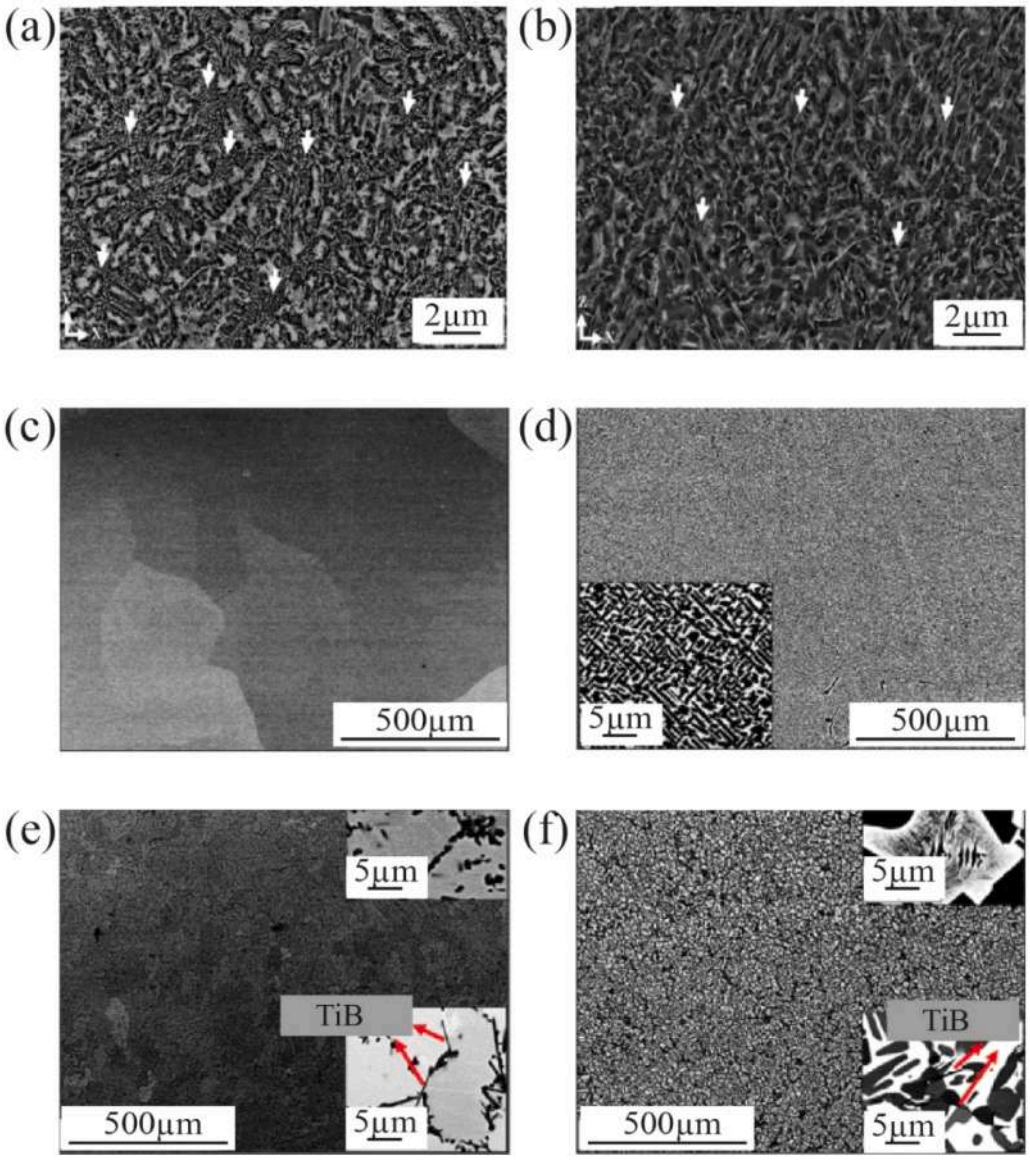


Fig. 17. Microstructures showing in-situ TiB formation in AM-processed Ti alloys: (a,b) L-PBF Ti-TiB_2 composite [155], and BSE micrographs of (c) Ti-20V, (d) Ti-12Mo, (e) Ti-20V-0.5B, and (f) Ti-12Mo-0.5B produced by LENS [158].

provide numerical simulations of in-situ reaction behavior (Ti-B) during L-PBF. They have demonstrated that the chemical heat released during L-PBF is directly proportional to the laser's input energy. The study considered a stoichiometric Ti: B ratio of 1:2 and assumed TiB_2 as the sole product, based on its most negative Gibbs free energy ($\Delta G = -308$ kJ mol^{-1}). Using COMSOL Multiphysics, they modeled the dynamic evolution of the molten pool, considering surface tension, Marangoni effects, and mass diffusion between Ti and B particles. The results showed that the exothermic $Ti + 2B \rightarrow TiB_2$ reaction provides sufficient heat to sustain the process even at modest power (35–45 W), significantly reducing the external energy demand. Increasing both power and the chemical reaction rate enlarged the molten pool and prolonged its lifetime, confirming the strong synergy between reaction heat and external laser input. Simulations also revealed localized temperature peaks and discontinuities in the melt pool boundary caused by TiB_2 solidification ahead of the laser track, a phenomenon later verified by Hu and Li [102]. Overall, Ye et al. demonstrated that the exothermic reaction dominates heat transfer during L-PBF and can effectively drive in-situ TiB_2 formation, making it a thermally efficient route for Ti-B AM.

6.2.2. *Ti-Zr*

The binary Ti-Zr system is rare in terms of in-situ production of alloys [160,161], and most often Zr is used as a third and additional alloying element in multicomponent Ti systems [15]. Due to similarities in atomic radius and crystal structure, Zr completely dissolves in the Ti-α lattice. Thus, Zr exhibits the characteristics of a weak β-stabilizer and refines the α-Ti grains due to solute drag and recrystallization effects, which ultimately results in a better balance of strength and ductility. For example, Kondoh et al. [160] demonstrated that Zr substitution increases the HCP lattice parameters and refines the α-Ti grains; likewise, Xie et al. [161] found that Zr additions decrease the rate of transformation from α′ to α and provide microstructural stability during the AM process. Due to the low β-stability of Zr and the narrow solidification range of the alloy, the alloy primarily resides in the α-phase field, thereby providing high biocompatibility and corrosion resistance, as well as good microstructural stability.

In-situ fabricated biomedical Ti-Nb and Ti-Zr-Nb alloys were made by González et al. [162] using a L-DED method with elemental Ti, Nb, and Zr powders. The authors employed a 1000 W diode laser in an Ar (<50 ppm O_2) atmosphere to fabricate dense deposits with

homogeneous composition (≤1.5 wt% standard deviation (SD)). Although there are significant differences in melting points among Ti, Nb, and Zr, the authors demonstrated adequate convective mixing of the melt pool, resulting in uniform β-phase microstructures.

The L-DED Ti-Zr-Nb alloys exhibited large columnar β-grains oriented parallel to the build direction with a thin equiaxed layer on top, indicating that L-DED results in directional solidification. Alloys with $Mo_{eq} > 10$ wt% have completely solidified as β-Ti, while Nb-lean compositions retain some amount of α″. Ti-35Zr-25Nb has E of 70 GPa, hardness of 3 GPa, and stable TiO_2/ZrO_2 passive layers (The corrosion current density (I_{corr}) of 0.02 μA cm^{-2}). Cell viability assays on SaOS-2 cells indicate excellent adhesion and viability comparable to those of cp-Ti. These results demonstrate that in-situ L-DED can efficiently produce dense Ti-Zr-Nb alloys with a single β-phase, low E, and high biocompatibility.

Lee et al. [163] extended this approach to in-situ L-DED of a Ti-Zr-Nb-Sn alloy using blended powders. Despite the use of refractory constituents, the deposits showed generally homogeneous elemental distributions, porosity below 0.1%, and less than 4% residual unmelted Nb. The optimized condition reached a UTS of 878 MPa and an elongation of 20.4%, while nanoscale ω formation and deformation-induced martensitic transformation contributed to the mechanical response and a recovery strain of about 2.5%. However, residual unmelted particles were also identified as preferential sites for localized corrosion, emphasizing the importance of energy input and homogenization.

In Ti-Nb-Zr systems, Souza et al. [164] found that Zr has a neutral-to-weak β-stabilizing effect and that it slightly reduces the formation of the ω-phase but is unable to suppress it altogether. Using in-situ synchrotron diffraction, the authors demonstrated that Zr delayed the precipitation of ω and reduced the hysteresis associated with the β ↔ α″ (of 30–45 °C) and β ↔ ω (of 120–240 °C) transformations, resulting in greater phase stability and elasticity in Nb-lean compositions.

Li et al. [34] designed a metastable β-type Ti-14Nb-6Zr-3Fe (TNZF) alloy using an L-PBF in-situ alloying method from elemental Ti, Nb, ZrH_2, and Fe powders. By applying the *Bo-Md* electronic structure map criteria close to the β/β + ω boundary (*Bo* = 2.821, *Md* = 2.419), the alloy was produced with almost complete density (99.97%) and a uniform composition (Ti-13.9Nb-6.1Zr-3.1Fe). Zr and Fe had a synergistic effect: Zr suppressed the β to ω transformation, while Fe refined the grains due to constitutional undercooling. The EBSD-IPF maps in Fig. 18 (a & b) demonstrate that the chessboard scanning strategy generated equiaxed β-grains with minimal texture and an aspect ratio of 2.0. TEM analysis revealed a β matrix containing partially collapsed ω precipitates (2–5 nm). The mechanical test data showed a YS of 1.1 GPa, an E of 68–71 GPa, and a fracture strain of 11–17%, demonstrating an exceptional synergy of strength, ductility, and E.

Kong et al. [165] produced in-situ Ti-34Nb-13Ta-xZr (x = 0, 5, 9 wt %) alloys using a L-PBF method employing elemental Ti, Nb, Ta, and Zr powders. They optimized the processing conditions (*P* = 240–300 W, *v*

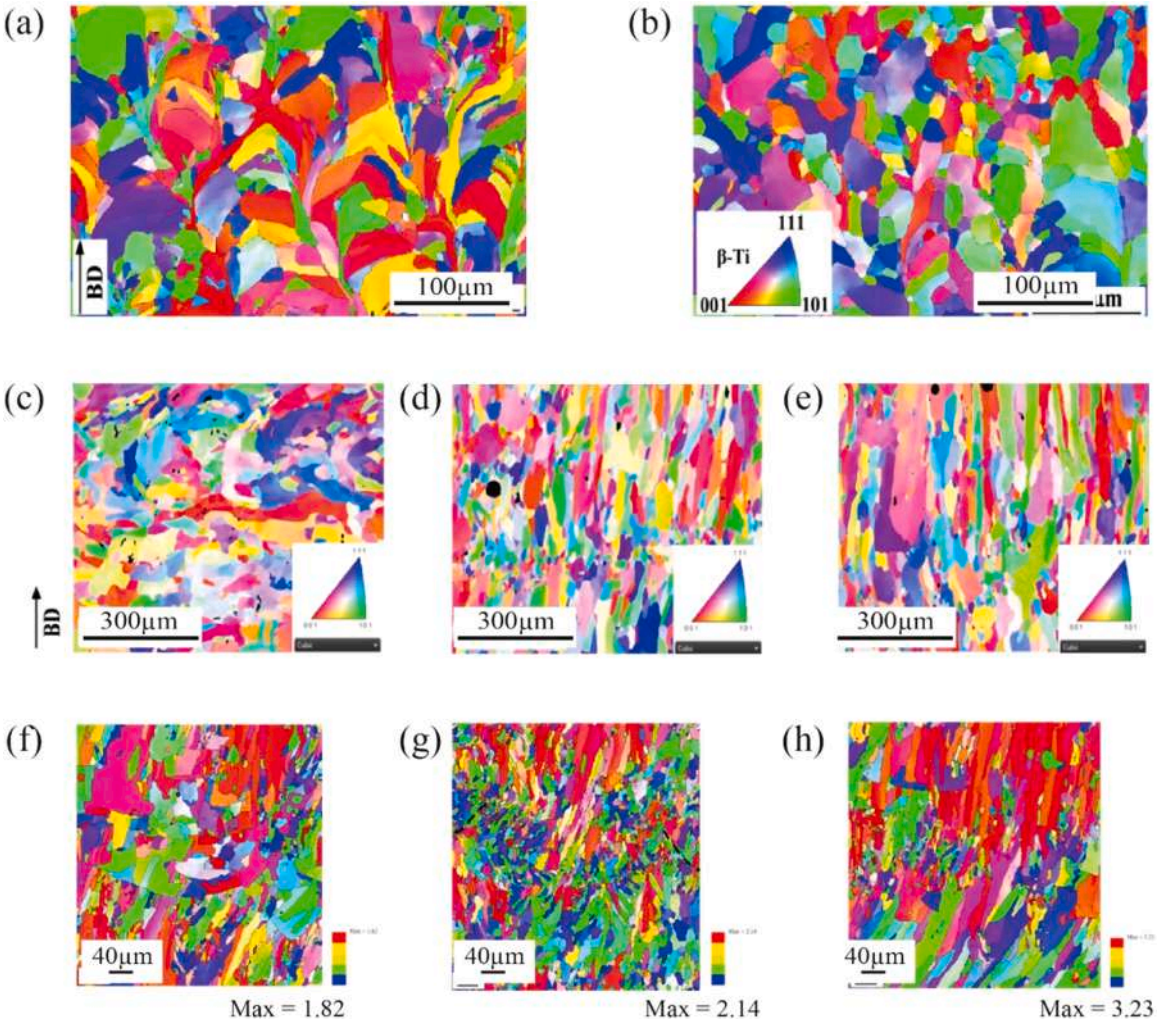


Fig. 18. EBSD maps of Zr-containing in-situ Ti alloys: (a) AS-TNZF and (b) CS-TNZF [34]; (c) Ti-29Nb-13Ta, (d) Ti-29Nb-13Ta-5Zr, and (e) Ti-29Nb-13Ta-9Zr [165]; and T3515 fabricated at (f) 250, (g) 275, and (h) 300 W [166].

= 400–1000 mm s-1, h = 35–65 μm, t = 20 μm) to achieve densities above 99.97%. XRD and TEM analyses confirmed a single β-phase without evidence of α″ or ω phases. As shown in Fig. 18(c-e), as the Zr content increases from 0 to 5 wt%, then to 9 wt%, the microstructure evolves from coarse, columnar β-grains with slight α″ traces to fully refined, homogeneous equiaxed β-grains, indicating enhanced grain refinement (about 30 μm) and complete suppression of secondary phases. The YS increased (681 → 772 MPa), hardness values increased (208 → 260 $HV_{0.1}$ (Measured as Vickers microhardness at 0.1 kgf load)), E ranged from 52 to 66 GPa, and ductility remained at 11–14%. Ion release experiments indicated less than 10 μg L^{-1}, and cell viability was greater than 95%, demonstrating excellent cytocompatibility.

Zhou et al. [166] fabricated in-situ Ti-35Nb-15Zr (T3515) β-type alloys by L-PBF of elemental Ti, Nb, and Zr powders to investigate the influence of P on anisotropy. When the power was set at 250–300 W, and the scan speed at 400 mm s^{-1}, fully dense β-phase alloys were obtained. EBSD images presented in Fig. 18(f-h) show fine equiaxed β-grains (about 8.8 μm) in the xy-plane, indicating a transition to stronger textures with higher power. Samples deposited horizontally displayed higher UTS and lower E compared to vertically deposited samples. Nanohardness measurements revealed slight decreases (xy: 7.12–6.49 GPa, and xz: 5.4–5.6 GPa), while cell viability (about 97.8%) and bone-like apatite formation confirmed the high bioactivity of these alloys. Therefore, Zr functions as a neutral β-stabilizer, enhancing phase uniformity and biocompatibility.

Jing et al. [167] found that adding a small amount of zirconium to the titanium alloy (Ti-6Al-4V) can partially replace titanium, forming TiZrAlV alloys. Since zirconium has an atomic radius and complete solid solubility like those of titanium, it acts primarily as a solid-solution strengthening element, refining the α/β microstructure and expanding the β-phase region. Jiang et al. [168] investigated the effect of Zr (0–45 wt%) content on the microstructure, mechanical behavior, and corrosion resistance of Ti-6Al-4V alloy produced by laser-based AM. The addition of Zr transformed the fine α′/α laths (about 0.3 μm) into equiaxed β-grain structures, thereby activating stress-induced α″ phase development. The UTS increased from 1044 MPa to 1360 MPa. The E decreased from 110 GPa to 92 GPa, but ductility was restored at higher Zr contents (about 12.5%). This restoration of ductility occurred due to the reversible β to α″ transformation. The I_{corr} decreased substantially (from 6.7 $\times 10^{-7}$ A cm^{-2} to 1.2 $\times 10^{-7}$ A cm^{-2}) due to the formation of a dense passive layer composed of TiO_2/ZrO_2. Therefore, Zr refined the martensitic structure, stabilized the β phase, and improved the mechanical and electrochemical properties of AM Ti-6Al-4V.

6.3. *In-situ alloying with eutectoid β-stabilizers*

Unlike isomorphous β-stabilizers, eutectoid β-stabilizers generally have more limited solid solubility in Ti and can increase the risk of intermetallic formation. At the same time, elements such as Fe and Cu can generate strong constitutional supercooling during laser-based AM, which helps suppress columnar growth and promotes finer, more uniform microstructures [19].

6.3.1. *Ti-Cu*

Titanium alloys are widely used in medical implants, but they exhibit poor tribological properties and low shear strength. The addition of Cu alleviates these disadvantages, resulting in enhanced mechanical properties, increased corrosion resistance, and antibacterial activity. Compared with silver (Ag), Cu is a more economical and safer metal. It is advantageous for the processability of the alloy in question and affords microstructural control during cooling of the liquid-phase sintered alloy. This advantage makes Ti-Cu alloys very attractive for orthopedic and dental implants, as they exhibit greater wear resistance and sintering efficiency [121].

Cu is a strong β-eutectoid stabilizer in titanium alloys, promoting the formation of the β phase and the precipitation of intermetallic phases, such as Ti_2Cu. For this reason, Ti-Cu alloys can be classified as β alloys. The addition of Cu reduces the melting point of the alloy, thereby improving manufacturability and enabling its utilization for structural purposes. These alloys also exhibit good ductility and a favorable heat-treatment response. Much work has been done on the Ti-Cu phase diagram and intermetallic compounds, but uncertainties remain regarding the number, stability, and crystal structure of the phases due to such difficulties as the high reactivity of titanium with atmospheric oxygen, the limited data on the liquidus at high temperatures, and the difficulty of distinguishing Ti_2Cu from Ti_3Cu in XRD patterns. There are several intermetallics in the Ti-Cu system (Ti_2Cu, TiCu, Ti_3Cu_4, $TiCu_2$, $TiCu_3$), but Ti_2Cu is the most promising for biomedical applications because of its Ti-rich composition [121].

Qin et al. [169] examined the effect of heat treatment on the microstructure and corrosion resistance of in-situ L-PBF Ti-5 wt% Cu, produced from mixed elemental Ti and Cu powders (40–65 μm, 99.7% purity) using a Realizer L-PBF 100 system (200 W power Yb: YAG, scan speed of 1000 mm s^{-1}, spot size of 40 μm, Ar atmosphere). As-built and heat-treated samples were compared after air cooling and furnace cooling from 900 °C (in the β-phase region) for 2 hrs. XRD and SEM revealed that the as-built microstructure contained non-uniform Ti_2Cu and α′ phases concentrated along melt pool boundaries due to rapid solidification. At the same time, the heat-treated alloys exhibited more uniform α + Ti_2Cu lamellae. A slower cooling rate (furnace-cooled) increased the Ti_2Cu interphase spacing from about 0.75 μm (air-cooled) to several microns and reduced α′ remnants, thereby improving corrosion resistance. Electrochemical testing (3.5 wt% NaCl and Hank's solution) showed that furnace-cooled Ti-5Cu achieved the highest polarization resistance (R_p of 7.7 MΩ cm^2) and the lowest Cu-ion release (of 232 μg L^{-1}), compared with the as-built condition (R_p of 3.5 MΩ cm^2, Cu of 310 μg L^{-1}). The enhanced performance was attributed to the coarse, well-spaced Ti_2Cu network, which limited microgalvanic coupling with α-Ti and promoted the formation of a stable TiO_2 film. In contrast, the as-L-PBF fabricated alloy displayed localized pitting near the Cu-rich melt-pool zones. The study concluded that heat treatment, especially slow furnace cooling, suppresses α′-Ti formation, homogenizes the Ti_2Cu distribution, and restores the corrosion resistance of L-PBF Ti-Cu alloys to levels comparable to those of CP-Ti, making them suitable for biomedical use.

Similarly, L-PBF has been utilized in a study on Ti-5 wt% Cu by Mosallanejad et al. [170]. They used a Concept Laser Mlab system (power of 100 W, spot size of 50 μm, layers of 25 μm, striping with a 67° rotation, $O_2 < 0.1\%$) and adjusted the VED to 50–78 J mm^{-3} . Since the Ti powder particles (about 30 μm) were significantly larger than the Cu ones (about 6 μm), the laser first melted the Ti, creating a molten pool that gradually dissolved the finer Cu particles. At the same time, direct Cu melting was almost negligible. Rosenthal heat-transfer calculations showed that as the energy density increased, the melt pool depth for Ti increased from 46 to 54 μm, whereas for Cu it remained around 3 μm. They noted that a higher energy input resulted in fewer partially molten Ti particles, thereby improving the chemical homogeneity of the alloy. XRD analysis indicated the presence of only α-Ti, but with larger crystallites, higher microstrain, and a slightly higher c/a ratio (the Ratio of the lattice parameters c and a in an HCP crystal; deviations from the ideal 1.633 affect slip and mechanical behavior) at higher VEDs. Additionally, the lower-intensity (002) texture demonstrated less directional solidification and a greater Cu distribution within the alloy. As shown in Fig. 19(a-c), optical images at different VEDs reveal the gradual disappearance of Ti remnant particles (marked with red arrows). At the same time, EDS mapping confirms the diffusion of Cu into the surrounding α-Ti matrix. This study highlighted the importance of achieving the optimal balance between particle size and energy input for uniform in-situ Ti-Cu alloying.

In-situ L-PBF processing of titanium alloys with a 5% weight addition of copper was subjected to heat treatments by Talebi et al. [171]. They found that Cu addition refined the microstructure by promoting a clear

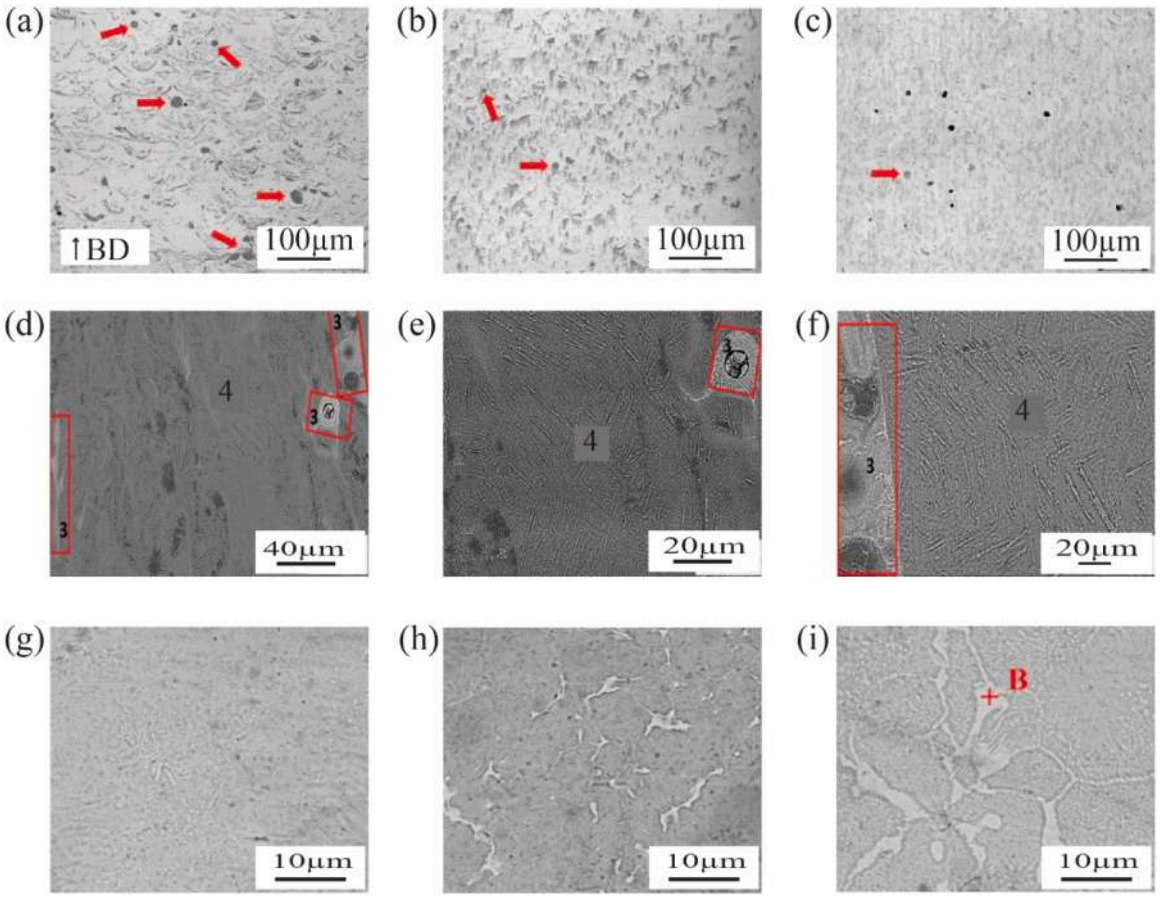


Fig. 19. Microstructures of in-situ L-PBF Ti-Cu alloys: optical micrographs at VEDs of (a) 55.39, (b) 61.68, and (c) 77.55 J mm^{-3} [170]; SEM micrographs of (d-f) Ti-2.5Cu [172]; and Ti-xCu with (g) 3, (h) 5, and (i) 10 wt% Cu [174].

CET in the β grains (about 80–15 μm) and produced much finer α′ laths (about 5.8 μm vs 15.9 μm in Ti) because of Cu strong *Q* of 35 K. EDS still revealed partial Ti-Cu mixing, with some Cu-rich spots (about 16 wt%). After heat treatment at 1050 °C for 3 hrs, the structure became fully equiaxed β (about 125 μm) with uniform α + Ti_2Cu lamellae, and various Ti_2Cu morphologies formed during slow cooling: blocky, submicron, lath, and lamellar. The hardness increased significantly from a value of 290 HV for Ti to a value of roughly 415 HV for as-built Ti-5Cu due to an increase in grain size uniformity, and it decreased to a value of 312 HV after a heat treatment was performed, as grains grew larger and the residual strain within the material was reduced.

Terceiro et al. [172] investigated the differences in the mechanical properties of Ti-2.5 wt%Cu produced via L-PBF and Ti-2.5 wt%Cu produced through conventional powder metallurgy using mixed Ti and Cu powders (each with purity > 99.99% and spherical Cu). L-PBF builds were printed with power ranging from 85 to 145 W, scan speeds of 800–1000 mm s^{-1}, hatch spacing of 80 μm, thickness of 30 μm, and VED of 35–75 J mm^{-3} , in Ar with a 67° rotation. Powder Metallurgy (P/M) samples were pressed at 750 MPa and sintered at 1000–1200 °C for 2 hrs. Optimal densification occurred at a VED of 65 J mm^{-3} , producing parts with < 0.5% porosity, while P/M parts retained 10–25%. Both routes produced heterogeneous structures: P/M because of Cu-rich liquid formation, and L-PBF because of Cu's low absorptivity. XRD and EDS showed that P/M samples contained α-Ti + Ti_2Cu + TiCu, whereas L-PBF samples mainly had α′-Ti + Ti_2Cu + TiCu due to faster cooling. Thermodynamic simulations confirmed the solidification sequence β → Ti_2Cu → TiCu. The best L-PBF condition (AM2, VED of 65 J mm^{-3}), gave a fine α′ martensitic matrix with uniformly distributed Ti_2Cu, hardness of 64 HRA (of 311 HV matrix, 511 HV intermetallic), and 0.5% porosity. Fig. 19(d-f) shows SEM images of this sample, where α′-Ti laths and small Ti_2Cu precipitates form a uniform structure with minimal Cu-rich segregation. The study emphasized that careful control of energy input and particle-size distribution can produce dense, homogeneous in-situ Ti-Cu alloys.

Han et al. [173] analyzed the microstructure and corrosion resistance of L-PBF Ti-5 wt% Cu produced using gas-atomized pre-alloyed powder compared with mechanically mixed Ti + Cu elemental powders. Samples were built on an L-PBF Solutions 280 HL system (power of 200 W, scan speed of 1150 mm s^{-1}, spot size of 90 μm, layers of 30 μm, hatch spacing of 100 μm, and Ar gas). The pre-alloyed builds showed a homogeneous acicular α/α′ structure without visible Ti_2Cu, while the mixed-powder builds contained coarse Ti_2Cu segregations. The uniform α/α′ matrix in the pre-alloyed material suppressed micro-galvanic corrosion and gave much better resistance in Hank's solution at 37 °C. The passive region ranged from 0.2 to 0.6 V with a primary passivation current density (I_p) of 2.8 μA cm^{-2}, and the charge-transfer resistance (R_{ct} of 10 MΩ cm^2) was about twice that of the mixed-powder alloy. The protective TiO_2 film was n-type semiconducting (0.87 nm thick, Donor Density (ND) of 5 × 10^{19} cm^{-3}). The study demonstrated that using pre-alloyed Ti-5Cu powder results in a uniform α/α′ microstructure and improves corrosion behavior by preventing Ti_2Cu-related galvanic effects.

Ji et al. [174] produced L-PBF Ti-xCu (x = 0, 3, 5, 7, 10 wt%) alloys using mixed Ti + Cu powders to examine how Cu content affects structure, corrosion, antibacterial properties, and cytocompatibility. The custom L-PBF setup (power of 95 W, scan speed of 45 mm s^{-1}, SF_6 + CO_2 gas) produced parts with an approximate density of 95–97%. Grain size decreased from 7.4 to 5.3 μm, and Ti_2Cu precipitates became more numerous as Cu increased. SEM/EDS showed strong Cu enrichment (of 41 wt%) at grain boundaries and of 5 wt% Cu in solid solution within

α-Ti. XRD revealed only α-Ti and Ti_2Cu. Hardness increased from 365 to 535 HV. In Hank's solution (37 °C), Ti-5Cu exhibited the lowest corrosion rate (0.011 mm y^{-1}) and current (1.31 μA cm^{-2}), while Ti-10Cu showed more corrosion and Cu^{2+} release (of 90 μg L^{-1}). Antibacterial tests with E. coli showed about 99% effectiveness for Ti-3Cu and of 100% for 5–10 Cu. All samples had a Relative Growth Rate (RGR) greater than 90%. As illustrated in Fig. 19(g-i), SEM micrographs of L-PBF-processed Ti-xCu alloys with Cu contents of 3, 5, and 10 wt%. The microstructure consists of a Ti matrix with Ti_2Cu intermetallic particles distributed mainly along grain boundaries. With increasing Cu content, the amount of Ti_2Cu second phase becomes more pronounced. These precipitates inhibit grain boundary movement and contribute to grain refinement in the Ti-Cu alloys. The results indicate that adding 3–5 wt% Cu gives the best balance of corrosion resistance, hardness, and antibacterial performance.

Wang et al. [175] studied in-situ L-PBF Ti-Cu alloys containing 1.25, 2.5, and 5 wt% Cu fabricated from mixed Ti + Cu powders (Ti of 39 μm, Cu of 7 μm) on a Concept Laser M2 ($P = 100$ W, $h = 80$ μm, $t = 25$ μm, VED = 55.6 J mm^{-3}, Ar gas). BSE-SEM images revealed a martensitic microstructure where α′ plates nucleate along prior-β grain boundaries and become progressively finer with increasing Cu content. XRD showed only α/α′ phases. The microstrain (Williamson-Hall) increased from 0.176% to 0.261%, suggesting Cu supersaturation in α′. SEM/EBSD revealed martensitic plates refined from 0.9 μm (1.25 Cu) to 0.76 μm (5 Cu) and 14–20% {10 1 1} < 10 1 2 > twins. TEM and High-Angle Annular Dark-Field Scanning Transmission Electron Microscopy (HAADF-STEM) identified α′ martensite with nanometric Ti_2Cu precipitates ([12 10]α′ // [010]Ti_2Cu) forming fine α′ + Ti_2Cu lamellae during β → α′ + Ti_2Cu decomposition. Hardness rose from 258 to 356 HV, UTS from 842 to 1242 MPa, while ΔL fell from 12% to 2.5%. Strengthening came from grain, solution, and precipitation effects; ductility dropped due to brittle Ti_2Cu.

6.3.2. Ti-Fe

Fe is recognized as one of the most valuable and economical β-stabilizers for titanium alloys used in in-situ alloying during AM. The very high Q of iron produces strong constitutional undercooling at the solid-liquid interface, which is beneficial to the CET and corresponds to substantial refinement of β grains. If added in moderate quantities, Fe increases solidification homogeneity, suppresses β-flecks, and inhibits intermetallic segregation, which results from the rapid solidification inherent to AM. It is known to partition into the β phase during alloying, which lowers the β-transus temperature, stabilizing β at room temperature, and promoting the precipitation of fine α upon cooling. This delicate balance between β stabilization and solid-solution strengthening provides greater mechanical isotropy and an improved α + β dual-phase microstructure, resulting in high strength and ductility. The thermal, physical, and metallurgical compatibility of Fe with Ti, along with its low cost and improved solute efficacy, make it an ideal candidate for inclusion in the next generation of in-situ AM Ti alloys, targeting controlled solidification, microstructural uniformity, and defect-free builds [79].

Beyond metallurgical efficacy, Fe has been recognized as a sustainable alloying element for Ti, arising from unavoidable impurities in the sponge and offering environmental and economic advantages when retained in controlled amounts [176]. Fe uniquely combines metallurgical efficiency and economic usefulness, as it is four orders of magnitude more abundant than rare β-stabilizers such as V, Nb, or Mo. Its slow TiFe intermetallic formation kinetics and high solubility in Ti permit complete dissolution on the timescale of rapid solidification, providing excellent β stabilization and a cost advantage simultaneously [177]. In addition, Fe has roughly four times the β-stabilizing capability of V based on Mo_{eq}, resulting in similar β stability at one-quarter of the solute level. Its abundance, low cost, and recyclability as a common impurity in Ti feedstocks make Fe a good sustainable replacement for V for AM-produced titanium. With its high β-stabilizing ability and economic viability, Fe is a valuable strategic alloying constituent for producing strong and ductile in-situ AM Ti alloys [178].

Recently, it has also been shown that the rapid solidification of AM prevents detrimental Fe segregation, allowing Fe to act as an effective β-stabilizer and grain refiner without forming harmful intermetallic compounds [179].

Issariyapat et al. [176] demonstrated sustainable alloy design concepts using Fe as a strengthening solute in L-PBF-produced titanium. A gradual increase of Fe from 0 up to 3 wt% caused a remarkable change in grain morphology, from large columnar α grains in Fe-free Ti to fine acicular α/α′ structures at ≥ 0.1 wt% Fe, with grain size reduced from > 100 μm to < 5 μm and about a doubling of strength (UTS of 1.0 GPa). This evolution is evident in the EBSD grain-size maps in Fig. 20(a & b), where even a minor Fe addition (0.03 wt%) triggers a columnar-to-acicular change and extensive refinement along the build direction, confirming the decisive role of Fe as a β-stabilizing, growth-restriction solute during L-PBF solidification. Huang et al. [177] presented low-cost in-situ alloying of Ti-1Fe by L-PBF using pre-mixed Ti and Fe powders, demonstrating that alloy homogeneity is primarily governed by Fe particle size and contamination. As illustrated in Fig. 20 (c & d), the use of coarse Fe powders results in Fe-rich β bands and poor mixing. In contrast, fine Fe powders ensure uniform dissolution and a homogeneous α/α′ martensitic microstructure after L-PBF. Wang et al. [180] produced a low-cost, biocompatible Ti-5Fe (0.2 wt% Y) alloy by L-PBF using HDH-Ti powders, achieving a density of 99.6%. Annealing enhanced ductility via oxygen scavenging by Y_2O_3. Huang et al. [178] further confirmed the industrial feasibility of in-situ Ti-1Fe as a low-cost alternative to Ti-6Al-4V. Using fine Fe powder and optimized L-PBF parameters (180 J mm^{-3}), they obtained a highly homogeneous acicular α/α′ + β microstructure with a firm {001}β||Z texture, like that of Ti-6Al-4V built under the same conditions as shown in Fig. 20(e & f). These results show that Fe, despite its simplicity and abundance, can reproduce the key microstructural and textural features of conventional α + β titanium alloys through proper process design.

Chen et al. [181] reported in-situ elimination of β-flecks in additively manufactured Ti-3.5 wt% Fe produced by L-DED. By coupling finite-element temperature-field simulation with a dynamic diffusion model, they showed that successive thermal cycles after solidification promote rapid Fe diffusion and progressive homogenization, converting Fe-rich dendritic β bands into an entirely uniform α + β microstructure within just a few layers. The initially Fe-rich β-flecks (Fe = 2–5 wt%) observed in the fusion zone were removed entirely in the underlying heat-affected region, defining a β-fleck-free zone formed in-situ during AM.

The compositional flexibility of L-DED has also been used to extend binary Ti-Fe toward ternary alloy design. Pang et al. [182] fabricated Ti-2Fe-xCu (x = 0–3 wt%) from blended powders and obtained predominantly equiaxed prior-β grains with α, retained β, and Ti_2Cu phases. Increasing Cu refined the α laths and increased the UTS from 740 to 800 MPa. The best strength-ductility balance was obtained for Ti-2Fe-1Cu, which reached a UTS of 760 MPa with 20% elongation. Higher Cu contents continued to increase strength but gradually reduced ductility, demonstrating the ability of L-DED to tune multicomponent Ti alloys through direct feedstock adjustment.

Fe thus appears to be a highly effective, low-cost, and sustainable β-stabilizer for in-situ AM titanium alloys, yielding grain refinement, microstructural homogeneity, and β-phase stability, in addition to strong, ductile, defect-free microstructures across L-PBF and L-DED routes.

6.3.3. Other eutectoid β-stabilizers: Ni, Cr, Mn, and Co

Eutectoid β-stabilizers such as Ni, Cr, Mn, and Co differ from isomorphous β-stabilizers because their solid solubility in Ti is more limited, and they can promote intermetallic compound formation. This gives them a strong ability to modify β-phase stability and solidification behavior at relatively low additions, but it also narrows their processing

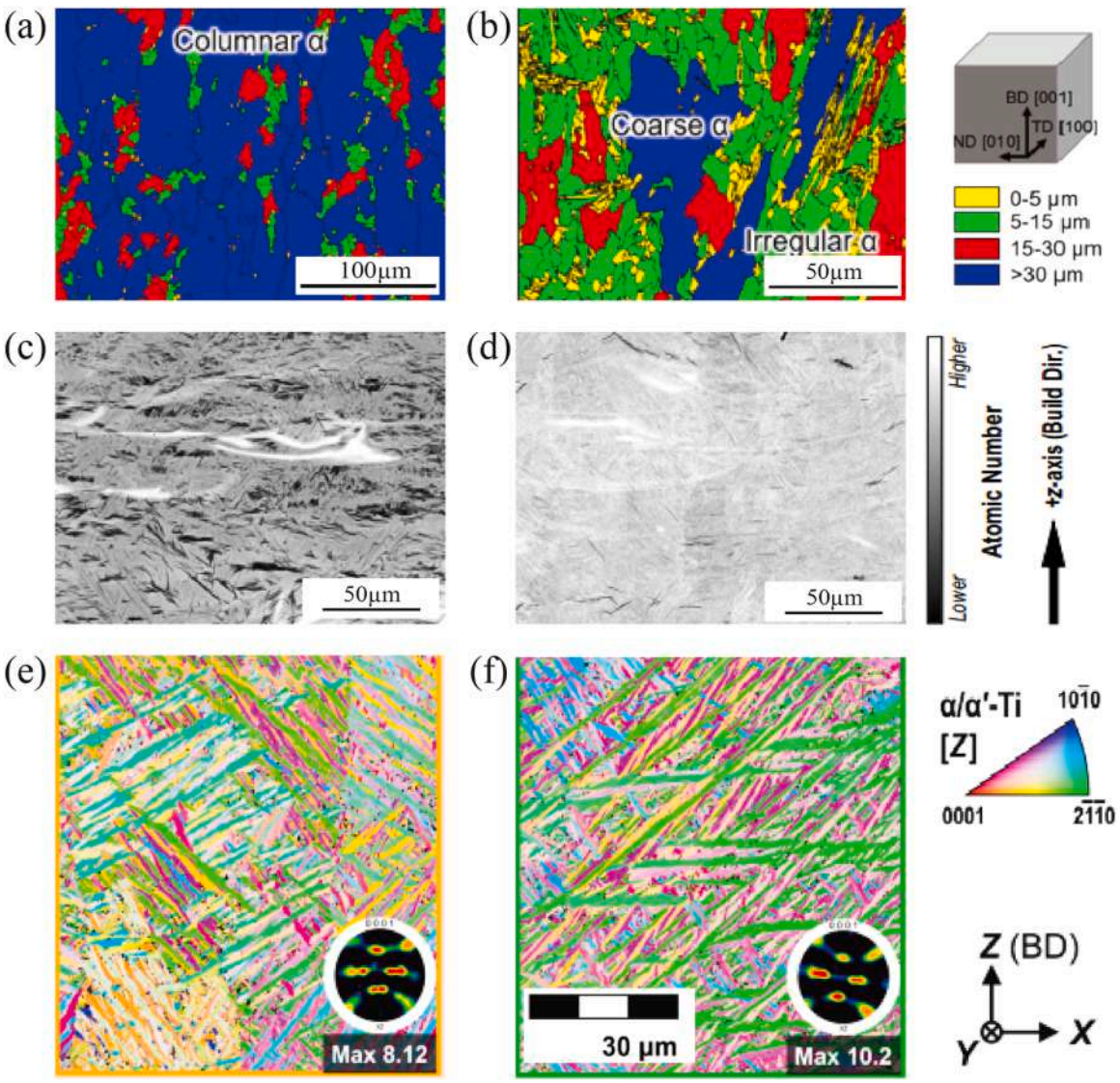


Fig. 20. Microstructural evolution of Fe-containing Ti alloys: EBSD grain-size maps of L-PBF (a) Ti and (b) Ti-0.03Fe [176]; BSE images of Ti-1Fe produced using (c) coarse and (d) fine Fe powders [177]; and EBSD IPF-Z maps of L-PBF (e) Ti-1Fe and (f) Ti-6Al-4V [178].

window during in-situ laser-based AM. In these systems, β stabilization and columnar-to-equiaxed transition must therefore be balanced against intermetallic formation, segregation, and possible ductility loss [118].

Nickel is one of the strongest eutectoid β-stabilizers for promoting constitutional undercooling in Ti-based LAM. The Ti-Ni system has a wider freezing range and a higher growth restriction factor than Fe, Cr, and Mn, meaning that a lower Ni addition can be sufficient to trigger β-grain refinement [183].

In-situ Ti-Ni alloying has been investigated mainly through the fabrication of NiTi shape-memory alloys from premixed elemental powders. Wang et al. [184] compared different AM routes, including L-DED, L-PBF, and EB-PBF, and showed that the processing route strongly affects chemical homogeneity, phase formation, and thermo-mechanical response. Their study reported that L-DED could successfully fabricate NiTi alloys with suitable phase transformation behavior, whereas L-PBF exhibited limitations in porosity, compositional uniformity, and process stability. This behavior is linked to the reactive nature of Ti-Ni alloying during melting, which can lead to local heat release, increased Ni evaporation risk, and rapid solidification, thereby disturbing melt-pool stability and making homogenization difficult. Therefore, although Ni is useful for functional Ti-based alloys, Ti-Ni in-situ alloying requires careful control of heat input, process route, and solidification conditions.

Binary Ti-Cr alloys have also been produced directly by in-situ L-DED. Zhang et al. [185] fabricated Ti-(6–15 wt%)Cr alloys from blended elemental powders and showed that increasing Cr progressively stabilized the β phase and refined the β grains from about 536–212 μm. Ti-10Cr provided the highest UTS, above 1.0 GPa, whereas Ti-15Cr developed a β-dominated microstructure with a YS of about 920 MPa and elongation of 20.3%. In contrast, Ti-13.4Cr showed severe embrittlement associated with ω formation, demonstrating that the mechanical response is highly sensitive to Cr content.

For Mn and Co, the strongest AM evidence is currently found mainly in Ti-6Al-4V-based or other multicomponent Ti systems rather than in simple binary Ti-X alloys. These additions are therefore discussed later, together with Ti-6Al-4V-based in-situ alloyed systems, where their roles in β-grain refinement, CET, intermetallic formation, and the strength-ductility balance can be assessed more directly.(Table 2)

6.4. *Multicomponent and Ti-6Al-4V-Based In-Situ Ti-Alloyed Systems*

After the discussion of binary Ti-X systems, multicomponent and Ti-6Al-4V-based alloys represent the next practical step in in-situ alloy design. In these systems, the final response is rarely controlled by a

Table 2
Summary of in-situ alloying strategies, microstructural responses, representative mechanical and functional properties, and main processing limitations for Ti-based alloy systems fabricated by fusion-based additive manufacturing.

Alloy System	Stabilizer / Role	Process	Key Microstructural Features	Representative Properties	Main Limitation / Challenge
Isomorphous β-stabilizers					
Ti-Mo (7–15 wt %)	Isomorphous β-stabilizer	L-PBF	β stabilization; α′/ω suppression at moderate Mo; α″/ω may persist in the as-built state; homogenization improves after rescanning or short heat treatment.	Ti-12Mo after 900 °C/90 s + WQ: YS 695 MPa*; UTS 820 MPa*; uniform ε 36%*. Ti-10Mo double scan: hardness 420–450 HV‡.	Incomplete Mo dissolution because of the high melting point; segregation at insufficient energy; excessive energy can increase defects.
Ti-Mo (5–12 wt %)	Isomorphous β-stabilizer	L-DED / LENS	Build-height-dependent α/β distribution and columnar β texture; Ti-5Mo shows a basket-weave α/α′ structure with strong solid-solution and dislocation strengthening.	Ti-5Mo: YS 549 ± 30 MPa; UTS 710 ± 22 MPa; ε 12 ± 2% (mean ± SD).	Low energy leaves residual Mo; high energy can cause vaporization, pores, or cracking; thermal cycling can produce microstructural anisotropy.
Ti-Nb (10–42 wt%)	Isomorphous β-stabilizer	L-PBF; EB-PBF	α″ at lower Nb; increasing Nb promotes retained β; Nb-rich/lean regions and residual Nb can persist. EB-PBF Ti-10 at % Nb also retained partially dissolved Nb despite an 880 °C build temperature.	Ti-35Nb from elemental blend: E 85 ± 2 GPa†; YS 636 ± 80 MPa†; UTS 750 ± 51 MPa†; ε 2.2 ± 1.4%†; hardness 241 ± 14 HV (SD reported for hardness).	Slow Nb dissolution and local segregation; residual Nb can act as weak interfaces; ω precipitation can restrict slip at high Nb.
Ti-Ta (10–50 wt%)	Isomorphous β-stabilizer	L-PBF	Increasing Ta promotes α′→α″→β stabilization; high energy and heat treatment improve Ta dissolution; lamellar α + β forms after annealing.	Ti-15Ta: E 110 ± 2 GPa; YS 902 ± 15 MPa; UTS 1102 ± 17 MPa; ε 5.1 ± 0.3% (reported as mean ± SD).	Very large melting-point and density mismatch; residual Ta remains at insufficient energy input.
Ti-W (0–30 wt %)	Isomorphous β-stabilizer; grain refiner	LENS / L-DED	Progressive prior-β grain refinement (>170 to ~30 μm at 23 wt% W) without reported intermetallic formation; refinement arises from combined solute and nucleation effects.	The primary LENS study summarized in Section 6 focused on grain refinement and did not report tensile properties.	High W melting point and density complicate dissolution; local W-rich regions can remain at insufficient energy input.
Neutral solutes and reactive additions					
Ti-B / TiB / TiB_2 (≤5 wt% B or TiB_2)	Reactive addition; in-situ reinforcement former	L-PBF; LENS	Rapid Ti + B reaction forms TiB/TiB_2; TiB whiskers strongly refine prior-β grains and weaken the typical ⟨001⟩β texture.	TiB/Ti composite: hardness ~402 HV*; YS ~1.1 GPa*; UTS ~1.42 GPa*.	The exothermic reaction requires precise energy control; excessive TiB networks can reduce ductility.
Ti-Zr (binary or Zr as tertiary addition)	Neutral solute / weak β stabilizer	L-PBF; L-DED	Zr dissolves readily in Ti; refines α/β microstructures and can delay α′→α transformation. In multicomponent systems it assists phase stabilization with Nb/Ta/Mo.	Ti-6Al-4V-Zr: UTS up to 1360 MPa*; E ~92 GPa*; Icorr reduced from 6.7×10^{-7} to 1.2×10^{-7} A cm^{-2}*.	Zr alone is insufficient for strong β retention; properties remain strongly composition- and process-dependent.
Eutectoid β-stabilizers					
Ti-Cu (1.25–10 wt %)	Eutectoid β-stabilizer	L-PBF	Cu promotes CET and α′ refinement; Ti_2Cu forms with increasing Cu and can segregate near grain/melt-pool boundaries.	Across Ti-1.25–5Cu: UTS 842→1242 MPa‡; ε 12→2.5%‡; hardness 258→356 HV‡. Ti-5Cu corrosion rate ~0.011 mm y^{-1} *; antibacterial efficacy ~100% at 5–10 wt% Cu*.	Excess Ti_2Cu reduces ductility and can promote micro-galvanic corrosion; Ti/Cu particle-size mismatch complicates homogenization.
Ti-Fe (0.03–5 wt%)	Eutectoid β-stabilizer; grain refiner	L-PBF; L-DED	Strong constitutional undercooling promotes CET and major grain refinement; fine Fe powders improve chemical uniformity; repeated L-DED thermal cycling can eliminate β-flecks.	Ti-1Fe(F), 180-W: YS 942.8 ± 33.8 MPa; UTS 1030.1 ± 27.2 MPa; ε 12.2 ± 1.1% (mean ± SD, n = 3).	Coarse Fe powder can create Fe-rich β bands; interstitial pickup and local segregation remain process-sensitive.
Ti-Ni / NiTi	Eutectoid β-stabilizer; functional alloying element	L-DED; L-PBF; EB-PBF	Strong constitutional undercooling: process route strongly affects chemical homogeneity, phase formation, and shape-memory response.	Shape-memory / superelastic response is strongly route-dependent; no single cross-route numerical performance value is directly comparable.	Ni evaporation, reactive melting, porosity, and a narrow composition window can destabilize the melt pool and promote Ti_2Ni.
Ti-Cr (6–15 wt %)	Eutectoid β-stabilizer	L-DED	Increasing Cr refines α laths and progressively stabilizes β; Ti-13.4Cr is ω-rich, whereas Ti-15Cr is β-dominated.	Ti-10Cr: YS 995 ± 15 MPa†; UTS 1042 ± 15 MPa†; ε 7.1 ± 2.1%†. Ti-15Cr: YS 920 ± 11 MPa†; UTS 941 ± 11 MPa†; ε 20.3 ± 3.2%†.	ω formation near the eutectoid composition can cause severe embrittlement; response is highly Cr-content dependent.

Notes: Values with ± are reproduced as reported in the original studies. * SD or uncertainty was not reported for the corresponding value. † The source reports an averaged value with ± but does not explicitly identify the ± term as SD. ‡ The reported range or change represents different compositions, processing conditions, or build locations rather than statistical scatter. Where SD is explicitly reported, this is stated in the table.

single solute. Instead, β-phase stability, grain refinement, precipitation behavior, corrosion resistance, antibacterial activity, and mechanical compatibility are adjusted through the combined action of several alloying elements. This makes multicomponent in-situ alloying particularly relevant for translating the mechanisms identified in binary systems into application-oriented titanium alloys for biomedical, aerospace, and structural use.

The dual-phase α + β titanium alloy Ti-6Al-4V is the most widely used titanium alloy, accounting for about 75–85% of global titanium alloy consumption [186]. This wide use is mainly related to its low density, high specific strength, good toughness, corrosion resistance, and relatively good processability [187,188]. In this alloy, Al acts as an α-stabilizer, while V stabilizes the β phase by reducing the β-transus temperature and allowing partial retention of β at room temperature [186,188]. These characteristics have made Ti-6Al-4V a benchmark alloy for aerospace, biomedical, and high-performance engineering applications, and one of the most established titanium alloys for L-PBF and other fusion-based AM routes [179,189].

In AM, Ti-6Al-4V can reach near-full density and mechanical properties comparable to conventionally processed material when suitable processing parameters and post-treatments are used [187,189]. However, the as-built condition still presents several limitations. Gas pores,

lack-of-fusion defects, partially melted particles, and high surface roughness can act as preferential fatigue crack initiation sites. At the same time, the rapid cooling conditions in L-PBF promote columnar prior-β grains and acicular α′/α laths, which can contribute to anisotropy, strain localization, and reduced fatigue reliability [187,190,191]. Because of these issues, Hot Isostatic Pressing (HIP), stress relief, machining, or surface finishing are often required to improve reliability and approach the performance expected from wrought Ti-6Al-4V [189, 192].

These limitations have made Ti-6Al-4V a useful benchmark matrix for in-situ alloy modification. By introducing additional alloying elements during AM, recent studies have tried to adjust β-phase stability, refine the prior-β grains, suppress excessive α′ martensite formation, reduce texture-related anisotropy, and improve the balance between strength, ductility, fatigue resistance, wear behavior, and cost-effectiveness while remaining within practical AM processing windows [179]. The following section first discusses selected multicomponent in-situ alloyed Ti systems then Ti-6Al-4V-based modifications with emphasis on how secondary solutes tune phase stability, microstructure, strength, modulus, and biological response.

Several representative systems illustrate this transition from binary alloying to multicomponent design. These include Mo-containing alloys for β stabilization and modulus control, Nb- and Nb-Zr-based alloys for biomedical compatibility, and Ta-Cu-containing alloys that combine β stabilization with antibacterial response. Beyond the binary range, multicomponent Ti-Mo-x alloys produced in situ by L-PBF have broadened the alloy design space for β-type alloys. Dzogbewu [193] employed Cu as a third element in Ti-10Mo-6Cu, where the combined action of Mo and Cu refined the α + β lamellae and increased the hardness to 460 HV without loss of density. Liu et al. [194] found that the presence of Mo, up to 15%, in Ti-6Al-4V lattices reduced the amount of α′ martensite and produced a continuous β matrix. In an architected simple cubic structure with 72.7% porosity, this resulted in an E of about 7 GPa, which is close to that of cancellous bone. These examples show that adding secondary solutes to Ti-Mo-based systems can extend the β-stabilized design space beyond binary compositions.

A similar design logic is observed in Nb-containing and Nb-Zr-containing systems, where the main objective is to stabilize β-Ti while reducing the elastic modulus and improving corrosion resistance for biomedical applications. Using L-PBF from elemental Ti, Al, and Nb powders, Polozov et al. [195] manufactured Ti-6Al-7Nb. The as-built parts, with a relative density of about 99%, still contained residual Nb particles, but these were fully dissolved after heat treatment at 1350 °C for 3.5 hrs. This produced a fine lamellar α + β structure, with a UTS of 850 MPa and a ΔL of about 2%. Popovich et al. [196] extended this approach to the in-situ L-PBF synthesis of Ti-22Al-25Nb intermetallic alloy. After dual-stage heat treatment at 1250 °C for 2.5 hrs followed by 900 °C for 24 hrs, the alloy developed a homogeneous B2 matrix containing orthorhombic Ti_2AlNb and α_2 precipitates, with microhardness increasing from 338 to 358 HV. These examples show that multicomponent Ti-Nb systems can form either α + β titanium alloys or intermetallic-containing microstructures, depending on composition and post-processing. In both cases, complete homogenization remains essential because residual Nb particles or compositional gradients can persist in the as-built condition.

The same principle has also been applied to Nb-Zr-based biomedical alloys. Arias et al. [162] used L-DED to synthesize Ti-Nb and Ti-Zr-Nb in-situ alloys from elemental powders. The resulting deposits achieved full density, homogeneous β microstructures, and good corrosion resistance, confirming that Ti-Nb-based compositions can be produced through both L-PBF and L-DED routes. In these systems, Zr contributes mainly through solid-solution effects, corrosion resistance, and phase-stability adjustment, while Nb provides stronger β stabilization and modulus reduction.

A further L-DED example was reported by Praveen et al. [197] for Ti-Nb-Ta alloys produced directly from elemental powders. Ti-28Nb-3Ta and Ti-16Nb-3Ta were deposited at 600 and 800 W, with generally uniform Ti, Nb, and Ta distributions above the initial build region. The higher-Nb compositions contained about 73–76% β phase, whereas the lower-Nb alloys were dominated by α″. The Ti-28Nb-3Ta compositions also showed favorable corrosion and tribocorrosion behavior in a simulated physiological environment, demonstrating that L-DED can be extended from binary alloy development to functional multicomponent biomedical Ti alloys.

The ability of L-DED to vary the feed composition during deposition also enables direct fabrication of compositionally graded alloys. Dobbelstein et al. [198] produced a crack-free Ti-Zr-Nb-Ta structure with a controlled gradient from $Ti_{25}Zr_{50}Ta_{25}$ to $Ti_{25}Nb_{50}Ta_{25}$ using elemental powder blends. A two-step strategy combining low-power deposition with higher-power remelting was required to homogenize constituents with strongly different melting points. The resulting gradient allowed several compositions to be screened within a single build, although the final chemistry remained sensitive to evaporation and processing parameters. This example directly demonstrates the compositional flexibility of L-DED for graded Ti-based alloy development.

Following the binary Ti-Ta studies, Polozov et al. [199] further expanded the alloy design space to ternary Ti-Ta-Cu compositions using in-situ L-PBF, with the aim of combining β stabilization with antibacterial response. The introduction of 2–4 wt% Cu into Ti-25Ta resulted in the formation of a nanocrystalline β-phase Ti-Ta-Cu solid solution, along with Cu-rich nanoclusters. This microstructure provided enhanced corrosion resistance and mild antibacterial properties without cytotoxicity. The ternary alloy showed a UTS of 990 MPa, an elastic modulus of 83 GPa, and a corrosion current density of 2.1×10^{-2} μA cm^{-2}, indicating the potential of in-situ L-PBF Ti-Ta-Cu as a bioactive β-stabilized implant material.

Taken together, those examples show that multicomponent in-situ alloying can go beyond simple β-stabilization. By combining β-stabilizing solutes with elements that influence corrosion resistance, antibacterial behavior, precipitation, or elastic modulus, these systems provide a more application-oriented route than binary Ti-X alloying alone.

A related strategy was reported for the metastable β titanium alloy Ti-5Al-5Mo-5V-3Cr, commonly known as Ti-5553. Zhang et al. [200] used Ti-5553 as a model alloy and introduced 2.5 and 5.0 wt% Mo nanoparticles into the powder feedstock before L-PBF. The added Mo acted in a bifunctional manner. Partially dissolved Mo particles provided surviving solid cores that served as heterogeneous nucleation sites, while the surrounding Mo-rich liquid promoted local supercooling and helped form fine equiaxed grains instead of coarse columnar β grains. At the same time, the dissolved Mo increased the β-phase stability and suppressed the formation of spatially heterogeneous α and isothermal ω phases during repeated thermal cycles in L-PBF. As a result, Ti-5553 + 5Mo showed weaker texture, refined equiaxed grains, and more uniform tensile behavior compared with the unmodified Ti-5553 alloy. The improvement in strength and ductility was mainly linked to the combined effect of grain refinement, Mo solid-solution strengthening, and suppression of metastable phase precipitation. This study shows that in-situ modification of an already multicomponent β titanium alloy can address both solidification-related grain morphology and solid-state phase heterogeneity within a single alloy design strategy.

The other group of multicomponent systems uses Ti-6Al-4V or Ti-based matrices as platforms for grain refinement and in-situ reinforcement. In these cases, the added phase or element is used not only to stabilize β-Ti but also to introduce load-bearing particles or to refine the α/β morphology during solidification. Kim et al. [201] prepared Ti-WC composites by L-DED, where WC was partially decomposed in situ to produce TiC and release W into the Ti matrix. The released W acted as a β-stabilizer, while TiC precipitates provided load transfer and dispersion strengthening. At a WC content of 5 wt%, the prior-β grain size was reduced from 440 to 81 μm, the α-lath thickness decreased from 2 to 0.5 μm, and the β-phase fraction increased to 18.5%. This shows that WC-derived additions can combine solute-driven β stabilization with

ceramic reinforcement, although the final response depends strongly on the degree of WC decomposition and the distribution of TiC particles.

Popovich et al. [202] investigated the effect of W addition on the microstructure and tensile properties of Ti-6Al-4V produced by L-DED through in-situ alloying of mechanically mixed Ti-6Al-4V and W powders. This route represents a direct in-situ alloying approach, since mechanically mixed Ti-6Al-4V and W powders were alloyed during deposition. The samples were deposited at 400 W, 10 mm s-1, 1 mm beam diameter, and 1 g min^{-1} feed rate, under < 50 ppm O_2, achieving > 99.8% density. Increasing W content up to 6 at% progressively refined both prior-β grains and α′ martensite, producing a partial CET. BSE-SEM and EDS analysis revealed that the bottom of each melt pool contained W-rich regions, with fine β-Ti surrounding these regions, indicating constitutional undercooling and solute partitioning. The 6 W sample had the smallest α′ martensite, about 310 × 61 nm, and nearly equiaxed β grains. XRD showed the presence of α, β, and Ti-W solid-solution peaks, with no intermetallic phases. TEM showed α′ martensite surrounded by W-Ti solid solution with high dislocation density. Tensile testing showed that the UTS increased from 940 to 1333 MPa and the YS increased from 860 to 1219 MPa, mainly due to solid solution strengthening and grain refinement associated with W's significant growth-restriction factor, *Q* of 22 °C. However, high W contents (>9 at%) led to segregation and reduced ductility, indicating that a moderate W addition of about 6 at% provides the best strength-ductility balance through β stabilization and the formation of a fine α′/β microstructure.

A related but different strategy is interfacial in-situ alloying in Ti-6Al-4V/W bimetallic structures. Wu et al. [203] demonstrated that in-situ interfacial alloying can generate dense Ti-6Al-4V/W bimetallic structures using L-PBF. Using an optimized linear energy density below 0.75 J mm^{-1}, the samples were free of cracks and porosity, with a fully metallurgically bonded interface composed of W, α-Ti, and β-Ti, without detectable intermetallic phases. The partial melting of Ti-6Al-4V during W-layer formation caused mutual diffusion of Ti, Al, V, and W across the interface, resulting in the nucleation of fine equiaxed β-Ti grains around dispersed W particles. The microhardness at the interface reached 503 HV, higher than both base materials, due to the fine β-Ti grains and the inherent hardness of W. Compressive and bending strengths reached 1510 and 2210 MPa, respectively, demonstrating that controlled in-situ interdiffusion between Ti-6Al-4V and W can produce strong and rigid bimetallic structures that combine the ductility of Ti with the hardness of W. Overall, these W-containing and WC-derived systems show that W can refine prior-β grains and stabilize β-Ti in Ti-6Al-4V-based or Ti-based matrices, but the useful composition range remains limited by segregation and ductility loss when the W content becomes excessive.

Among Ti-6Al-4V-based reinforcement strategies, B addition is particularly effective because it reacts in situ with Ti to form TiB, which can act both as a strengthening phase and as a grain-refining constituent. Rahman Rashid et al. [204] investigated the in-situ formation of TiB by L-DED of Ti-6Al-4V + 0.04 wt% B using a 5 kW Trumpf-POM DMD505 laser with 1600 W power and 60 mm min^{-1} scan speed. The presence of amorphous B, about 1 μm in size, promoted the precipitation of nano-scale TiB whiskers and the development of fine, discontinuous α-laths in the Ti-6Al-4V-0.04B clad. The resulting uniform TiB distribution increased the hardness from 400 HV to over 550 HV, without evidence of cracking or segregation.

Verma et al. [157] fabricated Ti-6Al-4V + 0–1.5 wt% B composites via L-PBF using an EOS M280 system with 400 W power, 75 μm hatch spacing, and 30 μm layer thickness. The complete reaction of B to form in-situ TiB whiskers, with dimensions of about 10–30 nm × 50–500 nm, resulted in pronounced grain refinement and a transition from columnar to equiaxed grains. The hardness increased from 370 Vickers hardness number (VHN) in the B-free alloy to 480 VHN at 1.5 wt% B, while the wear loss under 50 N dry sliding decreased nearly fourfold, from 159 to 36 mg. These results showed that in-situ TiB networks can simultaneously improve strength-related response and wear resistance in Ti-6Al-4V.

Sola et al. [205] studied the addition of small B contents, 0.1–0.5 wt %, to L-PBF Ti-6Al-4V using TiB_2 as a precursor. Rapid solidification led to complete reaction of B and the formation of in-situ TiB whiskers, about 10–100 nm in size, uniformly distributed along the α/β interfaces. The microstructure transitioned from columnar β to fine equiaxed grains below 25 μm, with α-laths thinner than 200 nm. The composite reached a hardness of 420 HV and YS of about 1.15 GPa, while maintaining a ΔL of 11%. This indicates that small B additions can refine the β grain structure without completely sacrificing tensile ductility.

Hizli et al. [120] used a thermal condition simulation for L-PBF processing, replicating Laser Glazed Processing (LGP), to conduct a quantitative thermodynamic analysis of in-situ TiB synthesis in Ti-6Al-4V + 0–2.5 wt% B. The results indicated that the exothermic Ti + B → TiB reaction, with an enthalpy change of 2.99 kJ g^{-1}, increased the melt-pool depth and refined the solidified microstructure. TEM analysis revealed nanoscale TiB whiskers with orthorhombic B27 structure and clean interfaces between TiB and α′ in Ti. Hardness increased from 356 HV in the B-free condition to 492 HV at 2.5 wt% B, and when B content was at least 0.2 wt%, a full CET occurred. This confirms that TiB can act as an efficient heterogeneous nucleant during rapid solidification. Overall, B-containing Ti-6Al-4V systems show that in-situ TiB formation contributes to both hardening and solidification control. The main limitation is that the TiB fraction and morphology must remain controlled, since excessive or continuous reinforcement can improve hardness while reducing ductility.

In contrast to B, which mainly acts through in-situ TiB formation and heterogeneous nucleation, Cu modifies Ti-6Al-4V through eutectoid β stabilization, constitutional undercooling, and Ti_2Cu precipitation. This makes Cu-containing Ti-6Al-4V systems useful for studying the balance between grain refinement, precipitation strengthening, antibacterial potential, and ductility loss. Goettgens et al. [206] performed in-situ alloying experiments with high Cu content, 15 wt%, in Ti-6Al-4V to study how Cu influences phase stability and solidification during L-PBF. Spherical Ti-6Al-4V and Cu powders, 15–53 μm, were mixed and processed on system in Ar with oxygen below 100 ppm using a two-step melting strategy: initial melting at 240 W and 800 mm s-1, followed by a pulsed remelting step at 400 W power and 2000 s^{-1} scan speed, with hatch spacing of 140–420 μm and layer thickness of 30 μm. Due to the high thermal conductivity and low absorptivity of Cu, the material contained partial heterogeneity, forming alternating Cu-rich and Ti-rich zones. EBSD and EDS analyses revealed a predominantly β-Ti matrix containing fine intergranular Ti_2Cu precipitates and residual α′/α within incompletely melted Ti-6Al-4V particles. XRD confirmed the coexistence of β-Ti, about 64 vol%, α/α′, about 17%, α″, about 18%, and traces of Ti_2Cu below 1%, clearly showing the strong β-stabilizing effect of Cu and the first identification of nano-orthorhombic α″ in the Ti-Al-V-Cu system. TEM and Fast Fourier Transform (FFT) analyses further characterized the α″ and β phases, which exhibit strong lattice distortion and nanoscale twinning. The authors reported that Cu promoted constitutional undercooling, leading to equiaxed β grains of 5–100 μm and suppressing the α′ martensite typically observed in Ti-6Al-4V. They concluded that the composition $Ti_{76.2}Al_{5.7}V_{3.2}Cu_{14.9}$ behaves as a metastable β alloy suitable for L-PBF, combining strong β stabilization with Ti_2Cu precipitation potential for subsequent age hardening and biomedical applications.

Mosallanejad et al. [207] extended Cu modification of Ti-6Al-4V to the EB-PBF route by producing Ti-6Al-4V-7Cu from a mechanically mixed Ti-6Al-4V and elemental Cu powder blend. In contrast to the strong columnar prior-β grains normally observed in EB-PBF Ti-6Al-4V, the Cu-modified alloy developed fine, fully equiaxed prior-β grains measuring about 38–150 μm. This transition was attributed to the combined effects of Cu rejection ahead of the solidification front, which generated a constitutionally supercooled zone, and the relatively lower thermal gradient in EB-PBF. The large melt pool also supported a more uniform Cu distribution than commonly reported in laser-based in-situ Ti-Cu alloying, although narrow layer-wise Ti_2Cu-rich bands were still

observed because of Cu segregation near successive melt-pool boundaries. XRD and SEM/EDS confirmed the formation of Ti_2Cu precipitates with different morphologies, reflecting the repeated heating, remelting, and ageing cycles of EB-PBF. The average hardness increased from about 307 HV for Ti-6Al-4V to 364 HV for Ti-6Al-4V-7Cu, mainly due to equiaxed grain formation, Cu solid-solution strengthening, and Ti_2Cu precipitation. This study shows that EB-PBF can be an effective route for in-situ Ti-6Al-4V-Cu alloying when grain refinement and chemical homogenization are targeted together.

Li et al. [208] further demonstrated the potential of EB-PBF through in-situ addition of 3.5 wt% Cu to Ti-6Al-4V. The elevated build temperature of about 750 °C reduced the cooling rate and accumulated thermal stress during processing, while Cu promoted the formation of fine equiaxed prior-β grains and weakened the crystallographic texture. The resulting alloy showed less than 5% variation in tensile properties among different build orientations and reached a UTS of 1053 MPa with an elongation of 15.3%, compared with 902 MPa and 13.5% for EB-PBF Ti-6Al-4V. These results demonstrate that EB-PBF in-situ alloying can simultaneously improve strength, ductility, and mechanical isotropy.

Kim et al. [209] further examined Ti-6Al-4V-xCu alloys (x = 0, 4, and 7 wt%) produced by L-DED from powder mixtures. The process employed a Laserline LDM-1000 diode laser with 1 kW power, a 3 mm spot size, a 9 g min^{-1} feed rate, a 1.3 mm hatch spacing, and N_2 + Ar shielding, producing dense deposits of about 99% on Ti-6Al-4V substrates. Because Cu has a high growth-restriction factor, Q of 28 K for 4 wt% Cu and 50 K for 7 wt% Cu, strong constitutional supercooling developed ahead of the solidification front, leading to a clear CET and significant grain refinement. Optical and SEM micrographs showed that unalloyed Ti-6Al-4V displayed coarse columnar β grains with Widmanstätten α colonies, whereas Ti-6Al-4V-4Cu and Ti-6Al-4V-7Cu formed fine equiaxed grains and thinner α laths of about 1 μm. XRD detected α + β + Ti_2Cu phases originating from the β → α + Ti_2Cu eutectoid reaction, with the Ti_2Cu volume fraction increasing with Cu content. EBSD confirmed that the average grain size decreased from 1.34 to 1.05 μm as Cu increased, and EDS mapping showed that Ti_2Cu precipitated preferentially along prior-β boundaries, particularly in the hypereutectoid 7 wt% Cu alloy.

Mechanically, the Ti-6Al-4V-4Cu composition showed the most balanced performance, with UTS of 1325 MPa, about 15% higher than the reference alloy, YS of 1312 MPa, and hardness of 446 $HV_{0.5}$, with only a slight reduction in ductility. The 7 wt% Cu alloy reached a hardness of 510 $HV_{0.5}$ but became brittle, with UTS of 841 MPa and almost no ΔL, due to the formation of continuous Ti_2Cu networks. These results demonstrate that moderate Cu additions, around 4 wt%, can balance grain refinement, solid solution strengthening, and precipitation strengthening in L-DED Ti-6Al-4V-Cu alloys. In comparison, excessive Cu above about 7 wt% leads to coarse or continuous Ti_2Cu formation and a severe loss of ductility. Overall, Cu-modified Ti-6Al-4V studies indicate that Cu can efficiently refine β grains and suppress fully martensitic microstructures, but its useful range is narrow. Moderate additions promote β stabilization and strengthening, whereas excessive Cu encourages continuous Ti_2Cu networks, chemical heterogeneity, and ductility loss.

Fe-containing multicomponent systems provide another route for modifying Ti-Al-V. In Ti-1Al-8V-5Fe, also known as Ti-185, Fe and V jointly stabilize the β phase, while rapid AM solidification can suppress β-fleck segregation, which has historically limited Fe-bearing titanium alloys produced by conventional routes. Farheen et al. [210] used in-situ synchrotron X-ray diffraction and infrared thermography to capture the real-time alloying sequence of L-PBF-fabricated Ti-185 alloys from blended elemental powders. Three stages of alloying were revealed: partial alloying in the melt pool, gradual diffusion into the Heat-Affected Zone (HAZ), and complete alloying at the bottom of the HAZ. Elemental mapping confirmed that repeated thermal cycling promoted full Fe-V dissolution and transformed compositionally banded α′ + β regions into a uniform β-Ti matrix, validating the role of Fe exothermic mixing enthalpy in accelerating in-situ alloying during L-PBF.

Zhou et al. [211] studied Ti-185 produced by EB-PBF and showed in-situ precipitation strengthening within columnar β grains. The inherently high solidification rate, about 10^3-10^5 K s^{-1}, suppressed Fe-stabilized β-flecks through solute trapping, while the elevated powder-bed temperature of 685 °C enabled nanoscale α precipitation during layer-wise reheating. Nanoscale α laths underwent pronounced plastic deformation, whereas microscale α laths and continuous grain-boundary α acted as crack-initiation sites. This indicates that controlling α-lath size to the nanoscale is essential for combining high strength (about 1.2 GPa UTS) with ductility in EB-PBF Ti-185. Azizi et al. [212] fabricated Ti-185 by L-PBF using pure Ti and Fe powders together with an Al-V master alloy. Their aim was to address the long-standing problem of Fe segregation and β-fleck formation in conventionally processed Ti-185. By adjusting the laser parameters, P = 370 W and v = 1035 mm s^{-1}, they produced high-density samples with less than 1% porosity and fine β grains of about 13 μm. Microscopy showed uniform Fe distribution, with a β matrix containing thin α films at grain boundaries and nanoscale α and ω particles inside the grains. The alloy reached a strength of 1.7 GPa in the as-built state and up to 1.8 GPa after heat treatment, while maintaining ductility. This study shows that rapid solidification during AM can reduce Fe segregation problems usually associated with this alloy and produce a strong, relatively uniform α + β microstructure.

A direct comparison of Ti-185 produced by L-PBF and L-DED was reported by Shang et al. [213], who emphasized the role of cooling rate in phase selection and mechanical response. The very high cooling rate in L-PBF, about 10^6 K s^{-1}, suppressed ω formation and produced fine equiaxed β grains of about 8.9 μm with nanoscale α laths, giving UTS of 1.1 GPa and ΔL of 9%. By contrast, the slower cooling rate in L-DED, about 10^2 K s^{-1}, promoted the β to ω to α transformation, coarser prior-β grains of about 27.6 μm, and brittle fracture. This comparison shows that the same nominal Ti-185 chemistry can follow very different phase-selection pathways depending on the AM thermal history. For this system, L-PBF is more favorable for suppressing ω formation and achieving a balanced strength-ductility response, while the slower L-DED thermal cycle can promote embrittling transformations.

The role of Fe in Ti-Al-V systems has recently been extended beyond β stabilization alone through oxygen-assisted alloy design. Song et al. [214] developed Ti-O-Fe alloys by L-DED using blended CP-Ti, Fe, and TiO_2 powders, showing that oxygen can be used as an intentional interstitial strengthening element rather than being treated only as a contamination source. The designed Ti-(0.34–0.50)O-(3.17–3.32)Fe alloys developed fine equiaxed prior-β grains and refined α + β lamellae, while avoiding the Fe-rich β-flecks commonly associated with cast Ti-Fe alloys. This behavior was linked to the complementary partitioning of O and Fe, in which oxygen enriched the α-lath rims near α/β interfaces and strengthened the α phase, while Fe partitioned to the β phase, increasing β stability. In a related L-PBF study, Zhang et al. [94] used a surface-engineered feedstock containing Ti-6Al-4V, CP-Ti, and Fe_2O_3 nanoparticles to reduce the spatial phase heterogeneity usually observed in L-PBF Ti-6Al-4V. In this approach, CP-Ti diluted Al and V, and Fe promoted faster elemental partitioning and β formation; oxygen compensated for the strength loss through interstitial solid-solution strengthening. The resulting alloys showed a uniform lamellar α + β microstructure and more consistent tensile response in both vertical and horizontal directions. These studies show that Fe-O assisted in-situ alloying can be useful for AM-specific Ti alloy design when controlled feedstock preparation, β-stabilizer selection, and thermal history are considered together.

After Fe-containing Ti-Al-V systems, other eutectoid β-stabilizers have also been examined for in-situ modification of Ti-6Al-4V, mainly to promote CET, increase β-phase stability, and improve strength. However, compared with Fe and Cu, these additions often show a narrower useful range because the same solute levels that refine the prior-β grains may also promote brittle intermetallic formation or reduce tensile

ductility. Nickel is one of the most effective eutectoid additions for promoting grain refinement in Ti-6Al-4V during laser-based DED. In L-DED Ti64-Ni alloys, prior-β grain refinement was already observed at about 1 wt% Ni, while a fully equiaxed microstructure was reported at around 3–3.5 wt% Ni [183]. This confirms the strong effect of Ni on constitutional undercooling and CET. However, the same composition range also promotes Ti_2Ni intermetallic formation, which strongly reduces tensile ductility. A lower Ni content, around 0.9 wt%, avoided noticeable intermetallic formation and improved YS compared with L-DED Ti-6Al-4V, but did not achieve the complete CET observed at higher Ni levels. Therefore, Ni is highly effective for refining prior-β grains, but its useful processing window remains narrow because the chemistry required for equiaxed β-grain formation can also introduce brittle intermetallic phases [215].

Cr has also been examined as a eutectoid β-stabilizer for in-situ modification of Ti-6Al-4V during LAM. Compared with Fe, Cr has a lower growth-restriction effect and a narrower liquid + β freezing range, so its grain-refining effect is weaker at comparable alloying levels. Nevertheless, L-DED studies on Ti-6Al-4V-Cr have shown that about 4 wt% Cr can promote a notable CET, producing a near-equiaxed prior-β microstructure [216]. The resulting Ti-6Al-4V-4Cr alloy showed improved hardness and tensile strength compared with additively manufactured Ti-6Al-4V, although the strength remained lower than that of Ti-6Al-4V-4Fe and the ductility was reduced. This suggests that Cr can refine the β-grain structure in in-situ Ti-6Al-4V alloying, but its benefit is mainly strength-oriented and does not fully overcome the ductility limitations usually associated with eutectoid β-stabilizers [217].

Mn shows a similar but less intense grain-refining effect. In Ti-6Al-4V-5.1Mn produced by L-DED complete CET was reported, with fully equiaxed β grains of about 70 μm and a random β texture along the build direction. Mn also improved β-phase stability at room temperature, consistent with its relatively high Mo-equivalent contribution. The strengthening response was partly attributed to the formation of the Mn_2Ti intermetallic via the eutectoid reaction, which increased hardness and compressive strength relative to Ti-6Al-4V. However, as in Ni-containing systems, intermetallic formation reduced ductility, and tensile data for AM-built Ti-6Al-4V-Mn remain limited. Since Mn has a lower growth-restriction effect than Ni, a higher alloying level is required to achieve effective CET, which increases the risk of intermetallic-related embrittlement [218].

A different approach is to use more than one eutectoid element at a controlled level rather than relying on a high amount of a single addition. The combined addition of Co, Cr, and Ni has been explored as a multi-eutectoid strategy for in-situ alloying of Ti-6Al-4V. In L-DED, the introduction of a small amount of CoCrNi medium-entropy alloy powder into Ti-6Al-4V promoted a refined α/β microstructure and improved the strength-ductility balance. The refinement was mainly attributed to the high combined growth-restriction effect of the eutectoid solutes and to the in-situ decomposition of α′ martensite into ultrafine α/β lamellae. Unlike high single-solute eutectoid additions, the controlled multi-eutectoid route was reported to suppress obvious brittle intermetallic formation. The alloy reached a tensile strength of about 1.34 GPa with ductility around 5.1%, indicating that small multi-element eutectoid additions may offer a more balanced route than excessive single-element Ni, Co, or Cr additions [103].

Overall, multicomponent and Ti-6Al-4V-based in-situ alloyed systems demonstrate that the mechanisms identified in binary Ti-X alloys can be transferred to more practical alloy platforms. Isomorphous β-stabilizers such as Mo, Nb, Ta, and W mainly support β-phase retention and, in some cases, modulus reduction. Eutectoid elements such as Cu, Fe, Ni, Cr, and Mn introduce stronger constitutional undercooling, precipitation effects, and functional advantages such as antibacterial response or lower alloying cost, but they also increase the risk of intermetallic formation and ductility loss. Reactive additions, such as B, and ceramic-derived additions, such as WC, provide another pathway through in-situ TiB or TiC formation, where grain refinement is combined with reinforcement strengthening. The main challenge is that these benefits remain strongly composition-and process-dependent. Moderate additions can refine grains and improve the strength-ductility balance, whereas excessive additions or incomplete dissolution can promote segregation, brittle intermetallic or reinforcement networks, and loss of ductility. For this reason, multicomponent in-situ alloying should be treated as a coupled design problem involving feedstock architecture, melt-pool mixing, phase stability, and post-solidification transformations.

6.5. Comparison of in-situ and pre-alloyed feedstocks

The choice between in-situ alloying and pre-alloyed powders involves a balance between compositional flexibility and process reliability. Pre-alloyed powders already contain the target composition within each particle and therefore do not require complete dissolution and redistribution of separate alloying constituents during the short lifetime of the melt pool. In contrast, in-situ alloying depends on the melting, dissolution, and mixing of powders that may differ considerably in particle size, density, and melting temperature. These differences can introduce additional sources of heterogeneity, including unmelted particles, local segregation, and variations in phase formation. The extent of these effects is strongly dependent on the alloy system and on the preparation of the feedstock.

A direct comparison is available for Ti-35Nb produced by L-PBF from elemental powder mixtures and pre-alloyed powder. The material produced from mixed powders contained undissolved Nb and showed clear chemical and microstructural heterogeneity, while the pre-alloyed powder produced a more uniform microstructure without detectable residual Nb particles. This difference was also reflected in the tensile behavior. The mixed-powder material showed higher yield and tensile strengths, but its elongation was only 2.2 ± 1.4%, compared with 23.5 ± 2.2% for the material produced from pre-alloyed powder [36]. The lower ductility was associated with weak interfaces around undissolved Nb particles, which promoted crack initiation and brittle fracture. Heat treatment can reduce these differences by improving Nb diffusion and chemical homogeneity, although this introduces an additional processing step [142].

A similar effect of feedstock condition has been observed in Ti-Cu alloys. Han et al. [173] reported a more uniform α/α′ microstructure when Ti-5Cu was produced from atomized pre-alloyed powder, while processing of mixed Ti and Cu powders resulted in a non-uniform distribution of Ti_2Cu. This difference was important for corrosion behavior. The pre-alloyed material showed stable passivation and a charge transfer resistance of 10.09 ± 2.63 MΩ cm^2, compared with 4.76 MΩ cm^2 for the material produced from mixed powders. The mixed-powder condition also showed more severe pitting due to local micro-galvanic effects. This example shows that chemical heterogeneity introduced during in-situ alloying can affect not only the initial microstructure and mechanical response, but also properties that are relevant during service.

The same limitation appears in other systems, although direct comparisons with pre-alloyed feedstocks are less common. In Ti-Mo, the high melting temperature of Mo makes complete dissolution difficult, and chemical homogeneity depends strongly on particle size, energy input, and repeated melting [126,130]. In Ti-Ta, residual Ta particles are frequently observed because of the large difference in melting temperature between Ti and Ta. Both heat treatment and higher energy input can improve Ta dissolution and produce a more uniform microstructure [145,149]. The importance of this control is also evident under cyclic loading, where unmelted Ta particles can act as weak regions for crack initiation and reduce fatigue life [149]. In Ti-Fe, the problem is less severe when sufficiently fine Fe powder is used. Coarse Fe particles produce local Fe-rich regions, whereas fine particles distribute more uniformly and can produce in-situ Ti-1Fe with mechanical properties

comparable to conventional Ti alloy benchmarks [177,178] These results show that the limitations of in-situ alloying are not the same for all alloying elements and can often be reduced through suitable powder and process design.

Property repeatability is therefore another important difference between the two feedstock strategies. However, systematic build-to-build comparisons are still limited for most in-situ Ti alloy systems. The same limitation applies to long-term stability. Corrosion and fatigue studies for Ti-Cu and Ti-Ta show that local chemical or microstructural heterogeneity can influence performance during service [149,173], but equivalent long-term comparisons between in-situ and pre-alloyed materials are not yet available for most of the alloy systems discussed in this review. More comparative studies are therefore needed before the long-term reliability of in-situ alloyed Ti components can be assessed at the same level as established pre-alloyed feedstocks.

7. Challenges

7.1. Feedstock supply, powder quality, and homogenization

Several factors, including melting points, PSD, flow characteristics, recycling characteristics, and chemical composition, constrain the use of elemental blends as AM feedstocks [15]. Powder blending using dry methods (shaker, ball, tumbler, and centrifugal) is typically preferred for achieving a homogeneous mixture, although solvent-based wet blending has not performed well in many prior studies. In addition to the effects of constituent differences in melting point, light absorption, heat absorption, size and shape, and flow properties, the potential for oxidation and contamination during handling of the powders can make achieving homogeneity difficult [18]. Surface oxides and carbides that may be formed via gas phase surface modification techniques (such as N_2 plasma treatment) may have some benefit to the material. However, such techniques require careful control of atmosphere conditions to prevent reaction hazards, which limits their use on large-scale systems, particularly when dealing with hygroscopic powders [79]. Finally, supply chain issues exist, as the availability of Ti powders varies widely across regions and resource bases [44]. If high melting nucleates, such as Mo, are selected to enhance solidification behavior, submicron powder sizes are typically needed to ensure melting during processing. This increases cost and can compromise final part integrity if these additions do not fully dissolve [50].

7.2. Composition control, segregation, and incomplete alloying

Although in situ alloying enables rapid exploration of new chemistries, its practical implementation is limited by the difficulty of maintaining composition control during melting, mixing, and solidification. Control over composition is difficult because segregation and partially dissolved particles affect local chemistry, complicating post-processing treatments and increasing the likelihood of crack formation. The element-specific effects of laser processing are highly system-dependent. For example, enriching Mo and W near α-β interfaces may hinder microvoid development [15].

In addition to chemical inhomogeneities and segregation, these inhomogeneities are typically associated with spatially variable properties and several post-treatment difficulties. Unmelted particles can act as initiation sites for cracks, leading to early failure of the product. These issues show that composition control cannot be treated only as a feedstock problem, but must be managed across powder preparation, melting, and solidification. Mitigating these issues requires control throughout the full processing route. This begins with controlled premixing to reduce segregation in the powder blend, followed by in-process control of thermal conditions, melt-pool flow, and scan strategy. When necessary, additional scanning or remelting passes can be applied to improve liquid-state mixing and dissolve remaining unmelted particles [15].

7.3. Process-window sensitivity and laser-material coupling

Powder compositions vary significantly with respect to their absorptive properties and temperature response characteristics. Therefore, process parameters such as spot size (h, v), and the scanning strategy must be optimized to find an energy range that produces a safe melting zone and avoids under-melting, vaporization, over-melting, or pore formation from recoil pressure [219]. Even under the same power output and scan speed, differences in elemental absorption can produce different melting and mixing responses, requiring process parameters to be adjusted based on composition [79].

Increasing Marangoni circulation in the liquid state, for example by changing laser power and speed, adjusting scan-path proportions, applying multiple remelting passes, or preheating the substrate, is generally effective in improving liquid-state homogeneity during melting. However, strong convective flows can also segregate the liquid [79]. Additionally, increasing laser energy density and decreasing powder particle size can reduce partially molten debris, but trade-offs remain. For example, in L-DED, increasing v to improve CET may increase the risk of unmelted powder and pore formation. Therefore, the process window must be balanced between defect formation and mixing [16,50].

The same process complexity also limits the predictive capability of current numerical models for in situ alloying. In Ti-W, Rolchigo et al. [154] showed that coupling heat, fluid flow, and solute transport across different length and time scales required substantial simplification, while effects such as multilayer deposition, reheating-induced solid--state diffusion, unmelted particles, and deviations from local-equilibrium compositions and phases were not included. More recent thermal-fluid-solute modelling of in situ Ti-Nb L-PBF has incorporated local composition-dependent solidification paths, but still involves assumptions concerning evaporation, powder motion, and interlayer thermal history, with broader applicability requiring further validation [16]. Far-from-equilibrium kinetics introduce an additional difficulty in predicting microstructure and phase evolution [99].This is illustrated by the in-situ Ti-Al-Fe study of Cai et al. [220], where Scheil calculations predicted a terminal solidification reaction involving the formation of HCP and face-centered cubic (FCC) phases from the remaining liquid, whereas experimental analysis indicated that FCC-Ti formed through a stress-induced solid-state transformation from HCP to FCC. Therefore, complete transient solute redistribution and non-equilibrium phase selection in multielement Ti systems remain difficult to predict reliably.

7.4. Microstructural heterogeneity, anisotropy, and property scatter

At the component level, heterogeneously built products may exhibit position-dependent distributions of dissolved solutes and volatile-element loss, leading to degraded properties. Embrittlement has also been shown to occur when parts are fabricated using short, low-temperature processing windows. Therefore, stabilizing performance requires tight control over both the chemistry and the thermal history throughout all phases of production [37,44].

Composition strategies that increase growth restriction to promote CET, often using β-stabilizers, are attractive options. However, the optimal stabilizer level depends on the type of β-stabilizer used, and partially melted additions can further exacerbate anisotropy. High-quality, fully equiaxed microstructures may also result in a loss of ductility due to lattice distortion and brittle second phases. This highlights the need to achieve CET targets within mechanical tolerance windows [16,50]. Microstructural heterogeneity can also influence service-related wear response, as demonstrated in other advanced alloy systems [221].

7.5. Post-processing burden and microstructure stability

Partial reduction of chemical inhomogeneity and anisotropy through heat treatment after fusion-based AM processing is often cited for in-situ alloyed builds. However, results depend strongly on the alloy and its build history. Therefore, the additional time and cost required to produce even modest reductions in inhomogeneity and anisotropy through heat treatment can be significant. Measures taken to induce in-process liquid-state mixing, such as preheating elemental blends before L-PBF processing or deliberate scanning with multiple melt passes, can be used independently or together to provide a more uniform composition before heat treatment [15].

HIP can also be applied after L-PBF to seal interfacial defects formed during solidification. However, it is time-consuming and expensive and can potentially alter the microstructure of grain interfaces at elevated temperatures. The residual stresses induced in AM products by thermal cycling promote recrystallization and grain growth during subsequent heat treatments. Introducing small amounts of second-phase particles, such as oxides, carbides, and nitrides, has been shown to help control recrystallization and grain growth under the transient processing conditions typical of AM [79]. The post-processing-induced microstructural state may also affect service performance, since controlled partial recrystallization has been shown to markedly alter wear resistance under demanding conditions [222].

7.6. Scale-up, standardization, and qualification barriers

Industrialization is hampered by an overall lack of process standards, a lack of acceptable standards for in situ alloying, high Research and Development (R&D) costs for developing new processes, and fragile process control and quality assurance (QA), all of which have slowed industrialization [79].

The cost of pre-alloyed powders is too high for fast alloy development. In contrast, in situ alloying offers a less expensive route for alloy chemistry studies, feasibility studies of new alloys, and evaluation of new commercial-grade alloys through targeted elemental additions [15]. However, this cost advantage does not remove the need for reliable powder supply chains, validated feedstock specifications, and reproducible processing windows.

8. Future perspectives

8.1. In situ monitoring and closed-loop composition control

Current monitoring techniques can detect anomalies in melt-pool characteristics. However, they cannot determine whether compositional defects are present within the melt pool. Optical and thermal sensing devices, such as high-speed cameras and optical emission spectrometry, can indicate when melting becomes unstable, but they cannot detect localized elemental segregation or unmelted material. This limits the possibility of true in situ closed-loop composition control [79].

Therefore, researchers are combining hyperspectral and acoustic signals with ML algorithms to relate plume and melt-pool characteristics to chemistry. Laser-induced breakdown spectroscopy (LIBS) is also being explored to obtain element-by-element readouts, allowing L-PBF parameters to be adjusted in real time [223]. At the same time, ML-assisted laser AM of titanium has been identified as a priority for rapid parameter development and QA across different chemistries [29].

Since laser recipes for new alloys are often developed through empirical trials, structured laser-parameter databases need to be established. Complementary research has also focused on online monitoring and machine-learning-based methods to identify anomalies and defects, which can reduce scrap and manual rework [43,44].

8.2. Multiscale modelling, non-destructive evaluation, and physics-informed data integration

To reduce trial-and-error approaches, simulations of melting and solidification in powder blends have been developed to predict how different AM processes behave under non-equilibrium conditions [119]. Concurrently, in situ X-ray imaging, dynamic transmission electron microscopy (DTEM), and Graphics Processing Unit (GPU)-accelerated computational fluid dynamics (CFD) using the volume-of-fluid (VOF) method have enabled closer links between process physics and structural evolution across broader time and length scales [79].

Micro-computed tomography (micro-CT) is an effective tool for determining porosity in AM structures. However, its sensitivity to very small pores, especially those below 100 μm, can be limited depending on scan resolution and sample geometry. This is important because small defects can strongly influence fatigue failure. ML has significantly improved defect identification in AM structures, but ML alone provides correlations rather than mechanisms that link parameters, defect types, and properties [79].

These limitations point toward hybrid workflows rather than reliance on any single tool. Such approaches combine physics-based simulation to predict expected material behavior, in situ measurement techniques such as imaging to constrain transient process information, and ex situ measurement techniques such as micro-CT to measure final structure and establish process-structure-property-performance relationships across multiple length and time scales [79].

Future multiscale frameworks should therefore combine composition-dependent melt-pool dynamics and solute redistribution with more complete treatments of far-from-equilibrium solidification kinetics, while progressively incorporating realistic multitrack and multilayer thermal histories. Their predictive capability should also be validated across different alloy compositions and processing conditions [98,99].

8.3. Alloy design frameworks and CET-oriented strategies

Design-for-LAM frameworks establish target compositions and microstructures from the beginning, ensuring that they fit within the processing boundaries of titanium alloys and titanium matrix composites rather than requiring retroactive correction after printing [29]. Within this framework, in situ additions can be deliberately selected to induce heterogeneous nucleation and promote columnar-to-equiaxed transition during solidification. This approach can also help mitigate cracking in as-built components [15]. CET mechanisms therefore complement in situ additions and can be integrated into design-for-LAM programs that pair chemical options with process windows from the beginning [29].

Adjusting the solidification window and the final-stage eutectic liquid fraction provides additional control over crack susceptibility, enabling designers to balance printability and post-print integrity [15]. Long-term development should also expand growth-restriction theories to multicomponent systems, and define the critical thermal excursions or indicative Q levels that describe where CET can occur while maintaining nucleant stability during solidification of reactive Ti melts [50]. Integrating high-melting particulates such as TiB_2 and TiC with growth-restriction strategies, together with machine-assisted methodologies, can guide the formation of equiaxed microstructures in viable powder-processing environments [45].

8.4. Field-assisted, hybrid, and multi-material additive manufacturing

Advanced field-assisted approaches for Ti alloys, such as ultrasonic assistance, have been discussed within broader hybrid and multi-material AM technologies that may yield property combinations not achievable through AM alone [29]. External fields can promote CET and provide additional control over microstructure. However, their

application to AM still faces challenges related to attenuation of the applied field as the build height increases and scaling to larger or more complex parts [50].

Most hardware used for field-assisted laser AM is bespoke and nonstandard, which can produce disparate results under nominally identical conditions. Reported magnetic-field effects vary from refinement to coarsening, ultrasonic intensity generally decreases as build height increases, and many electric-current studies primarily heat the melt rather than acting as a separate auxiliary field. These issues limit the ability to fabricate large or complex parts using field-assisted methods and limit automation. When auxiliary fields are used, recipes developed without auxiliary fields typically do not translate well, and synchronized or beam-tracked control is required to couple the field consistently and stably [224]. Future work, therefore, needs to connect auxiliary-field design with parameter re-optimization, process monitoring, and reproducible equipment configurations.

8.5. Post-processing reduction, automation, and application-driven development

While various methods exist to correct defects after AM, it is equally important to bias microstructural development in the as-built condition. Selecting alloying additions and AM processes that influence the as-built microstructure can reduce the need for extensive post-processing. For example, the combination of EB-PBF and hot deformation has been suggested to improve both ductility and workability in Ti alloys [37]. Additionally, the capability of AM to create multi-material products provides broader opportunities for designing Ti alloys with combinations of strength, ductility, and elastic modulus that would be difficult to achieve using single-addition techniques [16].

Downstream from the AM equipment, the workflow for creating functional parts still suffers from friction. Surface finishing operations remain labor-intensive, expensive, and time-consuming. Therefore, manufacturers are increasingly adopting automated surface finishing technologies, including robots and other forms of automation, to improve product-quality stability and increase production rates [43]. Surface engineering may also be required when surface properties limit service performance, particularly where improved hardness, friction behavior, and wear resistance are needed [225].

The healthcare industry, including orthopedics and dentistry, is seeking new customized, low-toxicity materials that meet both mechanical and chemical requirements for personalized orthodontic and dental components. For such applications, long-term performance should also account for the combined effects of wear and corrosion under physiological conditions [226]. In situ alloying through blended powder feedstocks has the potential to reduce waste and enable rapid creation of patient-specific items. Survey trends highlight sustained focus on Ti-Nb and rising interest in Ti-Mo, Ti-Zr, and Ti-matrix composites such as TiC, ZrC, and Mo_2C, with exploratory additions such as Ta, Cu, and Fe also investigated. However, practical hurdles in process control and consistency still motivate further work [119]. Service-induced surface evolution can also modify tribological performance and should therefore be considered in application-oriented material development [227].(Fig. 21)

9. Conclusion

In situ alloying in fusion-based metal additive manufacturing has been shown to be a practical route for expanding the titanium alloy design space beyond the limited set of certified compositions that can be processed reliably as pre-alloyed powders. Across laser and electron beam powder bed fusion, alloy development has been accelerated using powder blends, enabling compositional tuning without the cost and lead time associated with atomized pre-alloyed feedstocks. At the same time, this approach shifts much of the processing uncertainty onto the feedstock itself. Printability and repeatability are closely linked to powder quality, thermophysical mismatch between constituents, and the level of compositional homogeneity achieved during spreading, melting, and solidification. As a result, alloy performance is not determined solely by nominal chemistry, but by the combined effects of blending route, powder-scale distribution, melt-pool transport, solidification path, and local thermal history.

Across the studies reviewed, three linked factors repeatedly control the final response of in-situ alloyed titanium systems: mixing, defect formation, and microstructure development. Effective melt-pool mixing improves chemical uniformity and reduces the persistence of solute-rich and solute-lean regions, while insufficient dissolution can leave high-melting additions as residual particles or localized segregation zones. Defect formation is also strongly tied to the local processing window, since lack of fusion and keyhole porosity are governed by the balance between energy input, track overlap, powder-bed condition, and melt-pool stability. Microstructure development then connects these processing conditions to the final properties, because solute effects and thermal history can alter β-phase stability, promote or suppress columnar-to-equiaxed transition, modify texture, and change the morphology of α, β, martensitic, or reinforced phases. When these

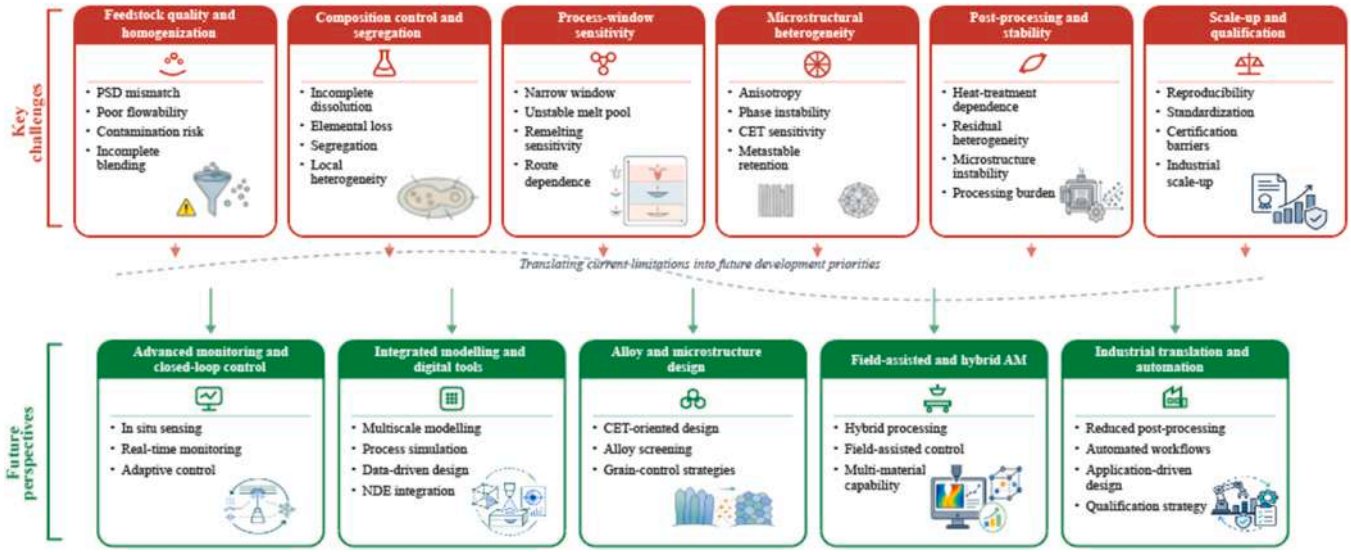


Fig. 21. Schematic overview of the main challenges and future directions for in-situ alloying of Ti alloys in fusion-based AM.

factors are controlled together, β-stabilized alloys and titanium matrix composites can develop refined microstructures and improved strength, ductility, modulus, or functional response. However, broader qualification remains limited by chemistry drift, incomplete alloying, intermetallic formation, property scatter, and scale-dependent changes in thermal history. Future progress, therefore, requires tighter feedstock specifications, real-time monitoring of both melt-pool stability and composition, and modelling frameworks that connect composition, defects, microstructure, and properties in a form suitable for certification and industrial translation.

CRediT authorship contribution statement

Mina Bakhshi: Writing – original draft, Visualization, Methodology, Investigation, Formal analysis, Data curation. **Eleonora Atzeni:** Writing – review & editing, Validation, Supervision. **Abdollah Saboori:** Writing – review & editing, Validation, Supervision, Resources, Project administration, Investigation, Formal analysis, Conceptualization. **Farnam Ranjkesh:** Writing – original draft, Visualization, Methodology, Investigation, Formal analysis, Data curation. **Amir Behjat:** Writing – review & editing, Validation, Supervision, Project administration, Investigation, Formal analysis, Conceptualization.

Declaration of Competing Interest

The authors declare that they have no known competing financial interests or personal relationships that could have appeared to influence the work reported in this paper.

References

[1] M.H. Mosallanejad, A. Abdi, F. Karpasand, N. Nassiri, L. Iuliano, A. Saboori, Additive manufacturing of titanium alloys: processability, properties, and applications, Adv. Eng. Mater. 25 (2023), https://doi.org/10.1002/adem.202301122.

[2] A. Behjat, M. Shamanian, F. Sadeghi, L. Iuliano, A. Saboori, Additive manufacturing of a novel in-situ alloyed AISI316L-Cu stainless steel: microstructure and antibacterial properties, Mater. Lett. 355 (2024), https://doi.org/10.1016/J.MATLET.2023.135363.

[3] V. Viale, J. Stavridis, A. Salmi, F. Bondioli, A. Saboori, Optimisation of downskin parameters to produce metallic parts via laser powder bed fusion process: an overview, 2022 1237, Int. J. Adv. Manuf. Technol. 123 (2022) 2159–2182, https://doi.org/10.1007/s00170-022-10314-z.

[4] N. Guo, M.C. Leu, Additive manufacturing: technology, applications and research needs, Front. Mech. Eng. 8 (2013) 215–243, https://doi.org/10.1007/S11465-013-0248-8.

[5] K. Wei, F. Li, G. Huang, M. Liu, J. Deng, C. He, X. Zeng, Multi-laser powder bed fusion of Ti–6Al–4V alloy: defect, microstructure, and mechanical property of overlap region, Mater. Sci. Eng. A 802 (2021) 140644, https://doi.org/10.1016/j.msea.2020.140644.

[6] R.R. Boyer, Introduction and overview of titanium and titanium alloys, Met. Handb. Desk-.-. Ed. (1998) 575–578, https://doi.org/10.31399/ASM.HB.MHDE2.A0003140.

[7] N. H.A. Besisa, T. Yajima, N. H.A. Besisa, T. Yajima, Titanium-based alloys: classification and diverse applications, Titan. -Based Alloy. - Charact. Appl. (2024), https://doi.org/10.5772/INTECHOPEN.1005269.

[8] A. Li, Q. Wang, R. Chen, X. Ding, Y. Su, H. Fu, Application of alloying for enhancing the corrosion resistance of titanium alloys: A review, Mater. Today Commun. 42 (2025), https://doi.org/10.1016/j.mtcomm.2024.111111.

[9] M. Correa-Rossi, L. Romero-Resendiz, D. Leal-Bayerlein, A.L. Garcia-Alves, F. Segovia-López, V. Amigó-Borrás, Mechanical, Corrosion, and Ion Release Studies of Ti-34Nb-6Sn Alloy with Comparable to the Bone Elastic Modulus by Powder Metallurgy Method, 3–17, Powders 2022 1 (1) (2022) 3–17, https://doi.org/10.3390/powders1010002.

[10] S. Alipour, A. Emdadi, J. Li, Recent advances toward damage-tolerant 3D-printed titanium alloys: Alloy design perspective, J. Appl. Phys. 139 (2026), https://doi.org/10.1063/5.0287936.

[11] R.K. Gupta, V.A. Kumar, C. Mathew, G.S. Rao, Strain hardening of Titanium alloy Ti6Al4V sheets with prior heat treatment and cold working, Mater. Sci. Eng. A 662 (2016) 537–550, https://doi.org/10.1016/j.msea.2016.03.094.

[12] D. Eylon, F.H. Froes, R.W. Gardiner, Developments in Titanium Alloy Casting Technology, JOM 1983 352 35 (2013) 35–47, https://doi.org/10.1007/BF03338203.

[13] M. Hourmand, A.A.D. Sarhan, M. Sayuti, M. Hamdi, A Comprehensive Review on Machining of Titanium Alloys, Arab. J. Sci. Eng. 46 (2021) 7087–7123, https://doi.org/10.1007/S13369-021-05420-1.

[14] C. Sun, Y. Wang, M.D. McMurtrey, N.D. Jerred, F. Liou, J. Li, Additive manufacturing for energy: A review, Appl. Energy 282 (2021) 116041, https://doi.org/10.1016/J.APENERGY.2020.116041.

[15] M.H. Mosallanejad, B. Niroumand, A. Aversa, A. Saboori, In-situ alloying in laser-based additive manufacturing processes: A critical review, J. Alloy. Compd. 872 (2021) 159567, https://doi.org/10.1016/J.JALLCOM.2021.159567.

[16] I. Mohanty, S.K. Kar, A comprehensive review of aspects of columnar to equiaxed transition, phase stability, and properties in novel Ti-alloys developed by additive manufacturing, J. Alloy. Compd. 1038 (2025), https://doi.org/10.1016/j.jallcom.2025.182642.

[17] Y.P. Dong, Y.L. Li, S.Y. Zhou, Y.H. Zhou, M.S. Dargusch, H.X. Peng, M. Yan, Cost-affordable Ti-6Al-4V for additive manufacturing: Powder modification, compositional modulation and laser in-situ alloying, Addit. Manuf. 37 (2021), https://doi.org/10.1016/j.addma.2020.101699.

[18] Z. Hua, L. Xiong, M. Zhang, C. Wang, G. Mi, P. Jiang, Microstructure evolution and tribological properties of (TiB+TiC)/Ti–6Al–4V composites fabricated via in situ laser-directed energy deposition of wire and powders in an underwater environment, Compos. Part. B Eng. 263 (2023) 110817, https://doi.org/10.1016/j.compositesb.2023.110817.

[19] M. Geetha, A.K. Singh, R. Asokamani, A.K. Gogia, Ti based biomaterials, the ultimate choice for orthopaedic implants – A review, Prog. Mater. Sci. 54 (2009) 397–425, https://doi.org/10.1016/j.pmatsci.2008.06.004.

[20] A.T. Sidambe, Biocompatibility of Advanced Manufactured Titanium Implants—A Review, 8168–8188, Mater 7 (7) (2014) 8168–8188, https://doi.org/10.3390/ma7128168.

[21] Bioscience and Bioengineering of Titanium Materials | Request PDF, (n.d.). https://www.researchgate.net/publication/316588838_Bioscience_and_Bioengineering_of_Titanium_Materials (accessed March 16, 2026).

[22] T. Wang, H.B. Tang, Y.Y. Zhu, D. Liu, H.M. Wang, Laser additive manufacturing of new α+β titanium alloy with high strength and ductility, J. Mater. Res. Technol. 26 (2023) 7566–7582, https://doi.org/10.1016/J.JMRT.2023.09.113.

[23] C. Leyens, M. Peters, Titanium and Titanium Alloys: Fundamentals and Applications, Titan, 1–513, Titan. Alloy. Fundam. Appl. (2005), https://doi.org/10.1002/3527602119.

[24] M. Morinaga, The molecular orbital approach to titanium alloy design (KEM), Key Eng. Mater. 770 (2018) 217–223, https://doi.org/10.4028/www.scientific.net/KEM.770.217.

[25] M. Abdel-Hady, K. Hinoshita, M. Morinaga, General approach to phase stability and elastic properties of β-type Ti-alloys using electronic parameters, Scr. Mater. 55 (2006) 477–480, https://doi.org/10.1016/j.scriptamat.2006.04.022.

[26] M. Morinaga, The molecular orbital approach and its application to biomedical titanium alloy design, Elsevier Inc, 2018, https://doi.org/10.1016/B978-0-12-812456-7.00003-2.

[27] T.M. Pollock, A.J. Clarke, S.S. Babu, Design and Tailoring of Alloys for Additive Manufacturing, Metall. Mater. Trans. A Phys. Metall. Mater. Sci. 51 (2020) 6000–6019, https://doi.org/10.1007/s11661-020-06009-3.

[28] Z. Fan, F. Gao, L. Zhou, S.Z. Lu, A new concept for growth restriction during solidification, Acta Mater. 152 (2018) 248–257, https://doi.org/10.1016/j.actamat.2018.04.045.

[29] M. Bermingham, D. StJohn, M. Easton, L. Yuan, M. Dargusch, Revealing the Mechanisms of Grain Nucleation and Formation During Additive Manufacturing, JOM 72 (2020) 1065–1073, https://doi.org/10.1007/s11837-020-04019-5.

[30] M.J. Bermingham, D.H. StJohn, J. Krynen, S. Tedman-Jones, M.S. Dargusch, Promoting the columnar to equiaxed transition and grain refinement of titanium alloys during additive manufacturing, Acta Mater. 168 (2019) 261–274, https://doi.org/10.1016/j.actamat.2019.02.020.

[31] E. Alabort, Y.T. Tang, D. Barba, R.C. Reed, Alloys-by-design: A low-modulus titanium alloy for additively manufactured biomedical implants, Acta Mater. 229 (2022), https://doi.org/10.1016/j.actamat.2022.117749.

[32] X. Chen, C. Qiu, Development of a novel metastable beta titanium alloy with ultrahigh yield strength and good ductility based on laser power bed fusion, Addit. Manuf. 49 (2022), https://doi.org/10.1016/J.ADDMA.2021.102501.

[33] G. Choi, W.S. Choi, J. Han, P.P. Choi, Additive manufacturing of titanium-base alloys with equiaxed microstructures using powder blends, Addit. Manuf. 36 (2020) 101467, https://doi.org/10.1016/J.ADDMA.2020.101467.

[34] Y. Li, L. Wang, H. Wu, F. Ding, M. Lei, J. Yang, J.P. Oliveira, M. Yan, W. Guo, Y. Li, High strength, low modulus, and ductile metastable beta Ti-Nb-Zr-Fe alloys by laser powder bed fusion in-situ alloying, J. Mater. Sci. Technol. 241 (2026) 270–283, https://doi.org/10.1016/J.JMST.2025.02.083.

[35] J. Su, F. Jiang, J. Wu, Y. Li, R. Han, L. Wang, R.C.W. Wong, J. Wang, S.L. Sing, Machine learning driven discovery of low modulus biomedical titanium alloys for additive manufacturing, 2026 171, Nat. Commun. 17 (2026) 5183, https://doi.org/10.1038/s41467-026-71927-6.

[36] J.C. Wang, Y.J. Liu, S.X. Liang, Y.S. Zhang, L.Q. Wang, T.B. Sercombe, L.C. Zhang, Comparison of microstructure and mechanical behavior of Ti-35Nb manufactured by laser powder bed fusion from elemental powder mixture and prealloyed powder, J. Mater. Sci. Technol. 105 (2022) 1–16, https://doi.org/10.1016/j.jmst.2021.07.021.

[37] T.S. Tshephe, S.O. Akinwamide, E. Olevsky, P.A. Olubambi, Additive manufacturing of titanium-based alloys- A review of methods, properties, challenges, and prospects, Heliyon 8 (2022) e09041, https://doi.org/10.1016/J.HELIYON.2022.E09041.

[38] C. chang LIU, Y. huan zi LI, J. GU, M. SONG, Phase transformation in titanium alloys: A review, Trans. Nonferrous Met. Soc. China (Engl. Ed. 34 (2024) 3093–3117, https://doi.org/10.1016/S1003-6326(24)66597-0.

[39] M.S. Oh, J.Y. Lee, J.K. Park, Continuous cooling β-to-α transformation behaviors of extra-pure and commercially pure Ti, Metall. Mater. Trans. A 2004 3510 35 (2004) 3071–3077, https://doi.org/10.1007/s11661-004-0052-5.
[40] H.Y. Ma, J.C. Wang, P. Qin, Y.J. Liu, L.Y. Chen, L.Q. Wang, L.C. Zhang, Advances in additively manufactured titanium alloys by powder bed fusion and directed energy deposition: Microstructure, defects, and mechanical behavior, J. Mater. Sci. Technol. 183 (2024) 32–62, https://doi.org/10.1016/J.JMST.2023.11.003.
[41] K. Yamanaka, W. Saito, M. Mori, H. Matsumoto, A. Chiba, Preparation of weak-textured commercially pure titanium by electron beam melting, Addit. Manuf. 8 (2015) 105–109, https://doi.org/10.1016/j.addma.2015.09.007.
[42] H.K. Rafi, N.V. Karthik, H. Gong, T.L. Starr, B.E. Stucker, Microstructures and mechanical properties of Ti6Al4V parts fabricated by selective laser melting and electron beam melting, J. Mater. Eng. Perform. 22 (2013) 3872–3883, https://doi.org/10.1007/s11665-013-0658-0.
[43] M.H. Mosallanejad, R. Ghanavati, A. Behjat, M. Taghian, A. Saboori, L. Iuliano, Untapped Opportunities in Additive Manufacturing with Metals: From New and Graded Materials to Post-Processing, Met. (Basel) 14 (2024), https://doi.org/10.3390/met14040425.
[44] M. Liu, C. Lei, Y. Wang, Baicheng Zhang, X. Qu, High-throughput preparation for alloy composition design in additive manufacturing: A comprehensive review, Mater. Genome Eng. Adv. 2 (2024) e55, https://doi.org/10.1002/MGEA.55.
[45] S.L. Sing, S. Huang, G.D. Goh, G.L. Goh, C.F. Tey, J.H.K. Tan, W.Y. Yeong, Title: Emerging Metallic Systems for Additive Manufacturing: In-situ Alloying and Multi-metal Processing in Laser Powder Bed Fusion, n.d.
[46] M. Simonelli, N.T. Aboulkhair, P. Cohen, J.W. Murray, A.T. Clare, C. Tuck, R.J. M. Hague, A comparison of Ti-6Al-4V in-situ alloying in Selective Laser Melting using simply-mixed and satellited powder blend feedstocks, Mater. Charact. 143 (2018) 118–126, https://doi.org/10.1016/j.matchar.2018.05.039.
[47] Y. Thompson, M. Polzer, J. Gonzalez-Gutierrez, O. Kasian, J.P. Heckl, V. Dalbauer, C. Kukla, P.J. Felfer, Fused Filament Fabrication-Based Additive Manufacturing of Commercially Pure Titanium, Adv. Eng. Mater. 23 (2021), https://doi.org/10.1002/adem.202100380.
[48] T. DebRoy, H.L. Wei, J.S. Zuback, T. Mukherjee, J.W. Elmer, J.O. Milewski, A. M. Beese, A. Wilson-Heid, A. De, W. Zhang, Additive manufacturing of metallic components – Process, structure and properties, Prog. Mater. Sci. 92 (2018) 112–224, https://doi.org/10.1016/j.pmatsci.2017.10.001.
[49] J.J. Beaman, D.L. Bourell, C.C. Seepersad, D. Kovar, Additive Manufacturing Review: Early Past to Current Practice, in: J. Manuf. Sci. Eng. Trans, 142, ASME, 2020, https://doi.org/10.1115/1.4048193.
[50] G. Xu, Q. Wang, R. Chen, A. Li, D. Chen, H. Fu, Columnar to equiaxed transition in additively manufactured titanium alloys: A comprehensive review of mechanisms and grain control strategies, J. Alloy. Compd. 1032 (2025) 181196, https://doi.org/10.1016/J.JALLCOM.2025.181196.
[51] R. Bhupal Reddy Donthi, B. Ramannagari, J. Xia, C. Chang, Z. Chen, al, X. Li, L. Li, Q. Liu, M.Talib Mohammed, S. V G, S. A. V, SLM-built titanium materials: great potential of developing microstructure and properties for biomedical applications: a review, Mater. Res. Express 6 (2020) 122006, https://doi.org/10.1088/2053-1591/ab624c.
[52] F. Huber, T. Papke, C. Scheitler, L. Hanrieder, M. Merklein, M. Schmidt, Situ Formation of a Metastable β-Ti Alloy by Laser Powder Bed Fusion (L-PBF) of Vanadium and Iron Modified Ti-6Al-4V, 1067, Met 8 (8) (2018) 1067, https://doi.org/10.3390/MET8121067.
[53] L.E. Murr, S.M. Gaytan, D.A. Ramirez, E. Martinez, J. Hernandez, K.N. Amato, P. W. Shindo, F.R. Medina, R.B. Wicker, Metal Fabrication by Additive Manufacturing Using Laser and Electron Beam Melting Technologies, J. Mater. Sci. Technol. 28 (2012) 1–14, https://doi.org/10.1016/S1005-0302(12)60016-4.
[54] M.F. Zäh, S. Lutzmann, Modelling and simulation of electron beam melting, 2009 41, Prod. Eng. 4 (2009) 15–23, https://doi.org/10.1007/S11740-009-0197-6.
[55] A. Barbas, A.S. Bonnet, P. Lipinski, R. Pesci, G. Dubois, Development and mechanical characterization of porous titanium bone substitutes, J. Mech. Behav. Biomed. Mater. 9 (2012) 34–44, https://doi.org/10.1016/j.jmbbm.2012.01.008.
[56] V. Petrovic, J. Vicente Haro Gonzalez, O. Jordá Ferrando, J. Delgado Gordillo, J. Ramon Blasco Puchades, L. Portoles Grinan, Additive layered manufacturing: sectors of industrial application shown through case studies, Int. J. Prod. Res. 49 (2011) 1061–1079, https://doi.org/10.1080/00207540903479786.
[57] Z. Fu, C. Körner, Actual state-of-the-art of electron beam powder bed fusion, Eur. J. Mater. 2 (2022) 54–116, https://doi.org/10.1080/26889277.2022.2040342;REQUESTEDJOURNAL:JOURNAL:TEMS20;WGROUP:STRING:PUBLICATION.
[58] W.J. Sames, F.A. List, S. Pannala, R.R. Dehoff, S.S. Babu, The metallurgy and processing science of metal additive manufacturing, Int. Mater. Rev. 61 (2016) 315–360, https://doi.org/10.1080/09506608.2015.1116649.
[59] P.C. Collins, R. Banerjee, S. Banerjee, H.L. Fraser, Laser deposition of compositionally graded titanium–vanadium and titanium–molybdenum alloys, Mater. Sci. Eng. A 352 (2003) 118–128, https://doi.org/10.1016/S0921-5093(02)00909-7.
[60] A.V. Gusarov, Radiative transfer, absorption, and reflection by metal powder beds in laser powder-bed processing, J. Quant. Spectrosc. Radiat. Transf. 257 (2020), https://doi.org/10.1016/j.jqsrt.2020.107366.
[61] C.L.A. Leung, S. Marussi, M. Towrie, R.C. Atwood, P.J. Withers, P.D. Lee, The effect of powder oxidation on defect formation in laser additive manufacturing, Acta Mater. 166 (2019) 294–305, https://doi.org/10.1016/j.actamat.2018.12.027.
[62] S.A. Khairallah, A.T. Anderson, A. Rubenchik, W.E. King, Laser powder-bed fusion additive manufacturing: Physics of complex melt flow and formation mechanisms of pores, spatter, and denudation zones, Acta Mater. 108 (2016) 36–45, https://doi.org/10.1016/j.actamat.2016.02.014.
[63] Z. Gan, O.L. Kafka, N. Parab, C. Zhao, L. Fang, O. Heinonen, T. Sun, W.K. Liu, Universal scaling laws of keyhole stability and porosity in 3D printing of metals, Nat. Commun. 12 (2021), https://doi.org/10.1038/s41467-021-22704-0.
[64] V. Juechter, T. Scharowsky, R.F. Singer, C. Körner, Processing window and evaporation phenomena for Ti-6Al-4V produced by selective electron beam melting, Acta Mater. 76 (2014) 252–258, https://doi.org/10.1016/j.actamat.2014.05.037.
[65] J. Ye, N. Semjatov, P. Bidola, G. Lindwall, C. Körner, Revealing the Mechanisms of Smoke during Electron Beam–Powder Bed Fusion by High-Speed Synchrotron Radiography, 8, J. Manuf. Mater. Process. 8 (2024) 2024, https://doi.org/10.3390/jmmp8030103.
[66] U.S. Bertoli, A.J. Wolfer, M.J. Matthews, J.P.R. Delplanque, J.M. Schoenung, On the limitations of Volumetric Energy Density as a design parameter for Selective Laser Melting, Mater. Des. 113 (2017) 331–340, https://doi.org/10.1016/j.matdes.2016.10.037.
[67] R. Cunningham, S.P. Narra, C. Montgomery, J. Beuth, A.D. Rollett, Synchrotron-Based X-ray Microtomography Characterization of the Effect of Processing Variables on Porosity Formation in Laser Power-Bed Additive Manufacturing of Ti-6Al-4V, JOM 69 (2017) 479–484, https://doi.org/10.1007/s11837-016-2234-1.
[68] J.J.S. Dilip, S. Zhang, C. Teng, K. Zeng, C. Robinson, D. Pal, B. Stucker, Influence of processing parameters on the evolution of melt pool, porosity, and microstructures in Ti-6Al-4V alloy parts fabricated by selective laser melting, Prog. Addit. Manuf. 2 (2017) 157–167, https://doi.org/10.1007/s40964-017-0030-2.
[69] A.A. Martin, N.P. Calta, S.A. Khairallah, J. Wang, P.J. Depond, A.Y. Fong, V. Thampy, G.M. Guss, A.M. Kiss, K.H. Stone, C.J. Tassone, J.N. Weker, M. F. Toney, T. van Buuren, M.J. Matthews, Dynamics of pore formation during laser powder bed fusion additive manufacturing, Nat. Commun. 10 (2019), https://doi.org/10.1038/s41467-019-10009-2.
[70] P. Bidare, I. Bitharas, R.M. Ward, M.M. Attallah, A.J. Moore, Fluid and particle dynamics in laser powder bed fusion, Acta Mater. 142 (2018) 107–120, https://doi.org/10.1016/j.actamat.2017.09.051.
[71] M.J. Matthews, G. Guss, S.A. Khairallah, A.M. Rubenchik, P.J. Depond, W.E. King, Denudation of metal powder layers in laser powder bed fusion processes, Acta Mater. 114 (2016) 33–42, https://doi.org/10.1016/j.actamat.2016.05.017.
[72] N. Derimow, J.M. Gorham, M.L. Martin, J.T. Benzing, R.M. White, N. Hrabe, Surface chemistry in Ti-6Al-4V feedstock as influenced by powder reuse in electron beam additive manufacturing, Appl. Surf. Sci. 602 (2022), https://doi.org/10.1016/j.apsusc.2022.154280.
[73] H.A. Murtaza, A. Mukhangaliyeva, B. Golman, A. Perveen, D. Talamona, Quantitative Characterization of Metal Powder Morphology, Size Distribution, and Flowability for Additive Manufacturing, J. Mater. Eng. Perform. 33 (2024) 10853–10867, https://doi.org/10.1007/s11665-023-08761-0.
[74] Y. Mao, J. Hu, Q. Chen, X. Shen, Quantitative Analysis of the Physical Properties of Ti6Al4V Powders Used in a Powder Bed Fusion Based on 3D X-ray Computed Tomography Images, Mater. (Basel) 17 (2024), https://doi.org/10.3390/ma17040952.
[75] J. Elambasseril, T. Song, S. Mendis, E. Lui, M. Leary, M. Brandt, M. Qian, Effect of powder characteristics on layer density, defects, and tensile properties of Ti-6Al-4V via laser powder bed fusion: establishing benchmark parameters for quality, Prog. Addit. Manuf. (2025), https://doi.org/10.1007/s40964-025-01046-z.
[76] P.R. Halani, Y.C. Shin, Situ Synthesis and Characterization of Shape Memory Alloy Nitinol by Laser Direct Deposition, Metall. Mater. Trans. A 2011 432 43 (2011) 650–657, https://doi.org/10.1007/s11661-011-0890-x.
[77] I. Yadroitsev, P. Krakhmalev, I. Yadroitsava, Titanium Alloys Manufactured by In Situ Alloying During Laser Powder Bed Fusion, JOM 2017 6912 69 (2017) 2725–2730, https://doi.org/10.1007/s11837-017-2600-7.
[78] Y. Zhou, X. Chen, F. Zhou, X. Li, Y. Huang, Q. Zhu, The Processing Map of Laser Powder Bed Fusion In-Situ Alloying for Controlling the Composition Inhomogeneity of AlCu Alloy, Met. (Basel) 13 (2023), https://doi.org/10.3390/met13010097.
[79] D. Xu, W. Yang, P. Cao, situ multi-metal alloying in laser-based additive manufacturing: A concise review, Compos. Part. B Eng. 299 (2025) 112443, https://doi.org/10.1016/J.COMPOSITESB.2025.112443.
[80] M. Easton, D. Stjohn, Grain refinement of aluminum alloys: Part I. The nucleant and solute paradigms - a review of the literature, Metall. Mater. Trans. A Phys. Metall. Mater. Sci. 30 (1999) 1613–1623, https://doi.org/10.1007/s11661-999-0098-5.
[81] A.S. Gohardani, G. Doulgeris, R. Singh, Multi-material laser powder bed fusion additive manufacturing of concentrated wound stator teeth, Addit. Manuf. Lett. 7 (2023) 100165, https://doi.org/10.1016/j.paerosci.2010.09.001.
[82] E.G. Brodie, A.E. Medvedev, J.E. Frith, M.S. Dargusch, H.L. Fraser, A. Molotnikov, Remelt processing and microstructure of selective laser melted Ti25Ta, J. Alloy. Compd. 820 (2020) 153082, https://doi.org/10.1016/j.jallcom.2019.153082.
[83] R. Bidulsky, F.S. Gobber, J. Bidulska, M. Ceroni, T. Kvackaj, M.A. Grande, Coated Metal Powders for Laser Powder Bed Fusion (L-PBF) Processing: A Review, 2021, Met 11 (11) (2021), https://doi.org/10.3390/met11111831.
[84] H. Chen, K. Kosiba, C. Suryanarayana, T. Lu, Y. Liu, Y. Wang, K.G. Prashanth, Feedstock preparation, microstructures and mechanical properties for laser-based additive manufacturing of steel matrix composites, Int. Mater. Rev. 68 (2023) 1192–1244, https://doi.org/10.1080/09506608.2023.2258664.
[85] C. Suryanarayana, Mechanical alloying: a critical review, Mater. Res. Lett. 10 (2022) 619–647, https://doi.org/10.1080/21663831.2022.2075243.
[86] C. Suryanarayana, Mechanical alloying and milling, Prog. Mater. Sci. 46 (2001) 1–184, https://doi.org/10.1016/S0079-6425(99)00010-9.

[87] T.Y. Ansell, T. Hanneman, A. Gonzalez-Perez, C. Park, A. Nieto, Effect of high energy ball milling on spherical metallic powder particulates for additive manufacturing, Part. Sci. Technol. 39 (2021) 981–989, https://doi.org/10.1080/02726351.2021.1876192.
[88] S. Khademzadeh, N. Parvin, P.F. Bariani, Production of NiTi alloy by direct metal deposition of mechanically alloyed powder mixtures, Int. J. Precis. Eng. Manuf. 16 (2015) 2333–2338, https://doi.org/10.1007/s12541-015-0300-1.
[89] M.S. Knieps, W.J. Reynolds, J. Dejaune, A.T. Clare, A. Evirgen, In-situ alloying in powder bed fusion: The role of powder morphology, Mater. Sci. Eng. A 807 (2021), https://doi.org/10.1016/j.msea.2021.140849.
[90] D. Bourke, K.T. Selvam, M.A. Obeidi, I.U. Ahad, D. Brabazon, Effect of powder and process parameters on in-situ alloying of nitinol during laser powder bed fusion, J. Mater. Res. Technol. 30 (2024) 7988–7997, https://doi.org/10.1016/j.jmrt.2024.05.178.
[91] K. Zhuravleva, M. Bönisch, K.G. Prashanth, U. Hempel, A. Helth, T. Gemming, M. Calin, S. Scudino, L. Schultz, J. Eckert, A. Gebert, Production of Porous β-Type Ti–40Nb Alloy for Biomedical Applications: Comparison of Selective Laser Melting and Hot Pressing, 5700–5712, Mater 6 (6) (2013) 5700–5712, https://doi.org/10.3390/ma6125700.
[92] E.M. Parsons, S.Z. Shaik, Additive manufacturing of aluminum metal matrix composites: Mechanical alloying of composite powders and single track consolidation with laser powder bed fusion, Addit. Manuf. 50 (2022), https://doi.org/10.1016/J.ADDMA.2021.102450.
[93] P.K. Farayibi, T.E. Abioye, A. Kennedy, A.T. Clare, Development of metal matrix composites by direct energy deposition of 'satellited' powders, J. Manuf. Process. 45 (2019) 429–437, https://doi.org/10.1016/J.JMAPRO.2019.07.029.
[94] J. Zhang, Y. Liu, G. Sha, S. Jin, Z. Hou, M. Bayat, N. Yang, Q. Tan, Y. Yin, S. Liu, J. H. Hattel, M. Dargusch, X. Huang, M.X. Zhang, Designing against phase and property heterogeneities in additively manufactured titanium alloys, 2022 131, Nat. Commun. 13 (2022) 4660, https://doi.org/10.1038/s41467-022-32446-2.
[95] R. Wang, L. Xi, K. Ding, B. Gökce, S. Barcikowski, D. Gu, Powder preparation during ball milling and laser additive manufacturing of aluminum matrix nanocomposites: Powder properties, processability and mechanical property, Adv. Powder Technol. 33 (2022), https://doi.org/10.1016/J.APT.2022.103687.
[96] H. Tan, T. Hu, F. Zhang, Y. Qiu, A.T. Clare, Direct Metal Deposition of Satellited Ti-15Mo: Microstructure and Mechanical Properties, Adv. Eng. Mater. 21 (2019) 1900152, https://doi.org/10.1002/ADEM.201900152.
[97] J. Schmidt, W. Peukert, Dry powder coating in additive manufacturing, Front. Chem. Eng. 4 (2022) 995221, https://doi.org/10.3389/FCENG.2022.995221/FULL.
[98] W. Tang, J. Li, B. Wu, C. Panwisawas, M. Li, J. Wang, N. Ren, L. Zeng, M. Xia, J. Li, Elemental segregation and solute transport in the in-situ alloying of miscible Ti-Nb alloys using laser powder bed fusion, Acta Mater. 299 (2025), https://doi.org/10.1016/J.ACTAMAT.2025.121417.
[99] J. Berry, A. Perron, J.L. Fattebert, J.D. Roehling, B. Vrancken, T.T. Roehling, D. L. Rosas, J.A. Turner, S.A. Khairallah, J.T. McKeown, M.J. Matthews, Toward multiscale simulations of tailored microstructure formation in metal additive manufacturing, Mater. Today 51 (2021) 65–86, https://doi.org/10.1016/J.MATTOD.2021.09.024.
[100] R. Schmid-Fetzer, A. Kozlov, Thermodynamic aspects of grain growth restriction in multicomponent alloy solidification, Acta Mater. 59 (2011) 6133–6144, https://doi.org/10.1016/j.actamat.2011.06.026.
[101] S. Kou, WELDING METALLURGY, SECOND EDITION, Weld. Metall. Second Ed. (2003) 1–461. https://doi.org/10.1002/0471434027.
[102] Y. Hu, J. Li, Selective laser alloying of elemental titanium and boron powder: Thermal models and experiment verification, J. Mater. Process. Technol. 249 (2017) 426–432, https://doi.org/10.1016/J.JMATPROTEC.2017.06.029.
[103] J. Su, F. Jiang, C. Tan, F. Weng, F.L. Ng, M.H. Goh, H. Xie, J. Liu, Y. Chew, J. Teng, Additive manufacturing of fine-grained high-strength titanium alloy via multi-eutectoid elements alloying, Compos. Part. B Eng. 249 (2023), https://doi.org/10.1016/j.compositesb.2022.110399.
[104] H. Wang, H. Liao, L. Hu, C. Zheng, J. Chang, D. Liu, M. Li, J. Zhao, W. Xie, B. Wei, Freezing Shrinkage Dynamics and Surface Dendritic Growth of Floating Refractory Alloy Droplets in Outer Space, Adv. Mater. 36 (2024) 2313162, https://doi.org/10.1002/ADMA.202313162;REQUESTEDJOURNAL:JOURNAL:15214095;ISSUE:ISSUE:DOI.
[105] W. Frieden Templeton, S. Hinnebusch, S.T. Strayer, A.C. To, P.C. Pistorius, S. P. Narra, A mechanistic explanation of shrinkage porosity in laser powder bed fusion additive manufacturing, Acta Mater. 266 (2024) 119632, https://doi.org/10.1016/J.ACTAMAT.2023.119632.
[106] Z. Wang, W. Chen, J. Xu, J. Zhu, Z. Ma, J. Shi, Q. Zhou, Fabrication of TC4 and Ti48Al bimetals by plasma arc additive manufacturing： Microstructure and mechanical properties, J. Mater. Res. Technol. 32 (2024) 2482–2494, https://doi.org/10.1016/j.jmrt.2024.08.101.
[107] H. Wang, L. Hu, W. Xie, J. Chang, C. Zheng, M. Li, Q. Wang, H. Liao, D. Liu, B. Wei, Metastable Liquid Properties and Surface Flow Patterns of Ultrahigh Temperature Alloys Explored in Outer Space, Angew. Chem. - Int. Ed. 63 (2024) e202400312, https://doi.org/10.1002/ANIE.202400312;PAGE:STRING:ARTICLE/CHAPTER.
[108] C. Iantaffi, C.L.A. Leung, Y. Chen, S. Guan, R.C. Atwood, J. Lertthanasarn, M. S. Pham, M. Meisnar, T. Rohr, P.D. Lee, Oxidation induced mechanisms during directed energy deposition additive manufactured titanium alloy builds, Addit. Manuf. Lett. 1 (2021), https://doi.org/10.1016/J.ADDLET.2021.100022.
[109] A. Roy, A.K. Singh, A. Arora, B.A. McWilliams, C. Mock, K.C. Cho, R.S. Mishra, Columnar-to-equiaxed transition in laser fusion additive manufacturing, Scr. Mater. 259 (2025) 116565, https://doi.org/10.1016/J.SCRIPTAMAT.2025.116565.
[110] A. Dass, A. Moridi, State of the art in directed energy deposition: From additive manufacturing to materials design, Coatings 9 (2019), https://doi.org/10.3390/COATINGS9070418.
[111] D. Zhang, D. Qiu, M.A. Gibson, Y. Zheng, H.L. Fraser, D.H. StJohn, M.A. Easton, Additive manufacturing of ultrafine-grained high-strength titanium alloys, 2019 5767785, Nat 576 (2019) 91–95, https://doi.org/10.1038/s41586-019-1783-1.
[112] C.J. Todaro, M.A. Easton, D. Qiu, D. Zhang, M.J. Bermingham, E.W. Lui, M. Brandt, D.H. StJohn, M. Qian, Grain structure control during metal 3D printing by high-intensity ultrasound, 2020 111, Nat. Commun. 11 (2020) 142, https://doi.org/10.1038/s41467-019-13874-z.
[113] Y. Chen, Y. Mao, M. Jiang, X. Chen, H. Wei, T. Han, Z. Wang, Z. Lei, P. He, Y. Chen, Achieving columnar to equiaxed transition in the as-deposited condition via coaxial wire feeding during laser directed energy deposition of Ti-6Al-4V, Addit. Manuf. 102 (2025) 104732, https://doi.org/10.1016/J.ADDMA.2025.104732.
[114] H. Li, Y. Huang, S. Jiang, Y. Lu, X. Gao, X. Lu, Z. Ning, J. Sun, Columnar to equiaxed transition in additively manufactured CoCrFeMnNi high entropy alloy, Mater. Des. 197 (2021), https://doi.org/10.1016/j.matdes.2020.109262.
[115] J. Su, F. Jiang, J. Teng, L. Chen, M. Yan, G. Requena, L.C. Zhang, Y.M. Wang, I. V. Okulov, H. Zhu, C. Tan, Recent innovations in laser additive manufacturing of titanium alloys, Int. J. Extrem. Manuf. 6 (2024), https://doi.org/10.1088/2631-7990/ad2545.
[116] D. Xu, W. Yang, M.P. Behera, S. Singamneni, M.A. Hodgson, P. Cao, Creating heterostructures via laser powder bed fusion using titanium and stainless steel mixtures, Mater. Sci. Eng. A 915 (2024), https://doi.org/10.1016/j.msea.2024.147260.
[117] S. Cao, Y. Zou, C.V.S. Lim, X. Wu, Review of laser powder bed fusion (LPBF) fabricated Ti-6Al-4V: process, post-process treatment, microstructure, and property, Light. Adv. Manuf. 2 (2021), https://doi.org/10.37188/lam.2021.020.
[118] G. Kanapaakala, V. Subramani, A review on β-Ti alloys for biomedical applications: The influence of alloy composition and thermomechanical processing on mechanical properties, phase composition, and microstructure, Proc. Inst. Mech. Eng. Part. L J. Mater. Des. Appl. 237 (2023) 1251–1294, https://doi.org/10.1177/14644207221141768.
[119] A.D. Dobrzańska-Danikiewicz, A. Bączyk, A review of new Ti-based materials manufactured in situ for biomedical applications, J. Achiev. Mater. Manuf. Eng. 121 (2023) 306–319, https://doi.org/10.5604/01.3001.0054.2844.
[120] H. Hizli, Z. Zou, J. Murray, A. Clare, M. Simonelli, Microstructural evolution in laser melted boron alloyed Ti-6Al-4V, J. Alloy. Compd. 981 (2024) 173762, https://doi.org/10.1016/J.JALLCOM.2024.173762.
[121] H. Mousa Mirabad, M.R. Akbarpour, F. Gazani, A. Ahmadi Chadegani, I. Khezri, A. Mirzamohammad, H. Damghani, O. Elahi, M. Nezakati Khameneh, H.S. Kim, The microstructure-mechanical property relationships in Ti–Cu alloys for biomedical applications: A review, J. Mater. Res. Technol. 37 (2025) 3155–3181, https://doi.org/10.1016/J.JMRT.2025.06.184.
[122] P.J. Bania, Beta titanium alloys and their role in the titanium industry, JOM 46 (1994) 16–19, https://doi.org/10.1007/BF03220742/METRICS.
[123] T.C. Dzogbewu, Laser powder bed fusion of Ti15Mo, Results Eng. 7 (2020) 100155, https://doi.org/10.1016/J.RINENG.2020.100155.
[124] N. Kang, Y. Li, X. Lin, E. Feng, W. Huang, Microstructure and tensile properties of Ti-Mo alloys manufactured via using laser powder bed fusion, J. Alloy. Compd. 771 (2019) 877–884, https://doi.org/10.1016/J.JALLCOM.2018.09.008.
[125] N. Kang, X. Lin, C. Coddet, X. Wen, W. Huang, Selective laser melting of low modulus Ti-Mo alloy: α/β heterogeneous conchoidal structure, Mater. Lett. 267 (2020) 127544, https://doi.org/10.1016/J.MATLET.2020.127544.
[126] T.Cephas Dzogbewu, W.Bouwer Du Preez, In situ alloying of Ti10Mo fused tracks and layers via laser powder bed fusion, (n.d.). https://doi.org/10.1051/mfreview/2022022.
[127] T. Krajňák, M. Janeček, J. Kozlík, D. Preisler, J. Stráský, M. Brázda, J. Kout, K. Halmešová, J. Džugan, Influence of the thermal history on the phase composition of laser directed energy deposited Ti-8.5 wt% Mo alloy, Mater. Des. 222 (2022) 111049, https://doi.org/10.1016/J.MATDES.2022.111049.
[128] S.A. Mantri, R. Banerjee, Microstructure and micro-texture evolution of additively manufactured β-Ti alloys, Addit. Manuf. 23 (2018) 86–98, https://doi.org/10.1016/J.ADDMA.2018.07.013.
[129] P. Ding, Y. Liu, C. Zhang, Q. Li, S. Wu, F. Chen, Microstructure and mechanical properties of in-situ Ti-5Mo alloys prepared by laser-directed energy deposition, Mater. Sci. Eng. A 960 (2026) 150127, https://doi.org/10.1016/J.MSEA.2026.150127.
[130] A. Duchaussoy, M. Marteleur, P.J. Jacques, L. Choisez, Improved mechanical properties of β metastable Ti alloys processed by laser powder bed fusion, Mater. Sci. Eng. A 887 (2023) 145755, https://doi.org/10.1016/J.MSEA.2023.145755.
[131] X. Dai, Y. Sun, J. Han, Additive Manufacturing of High-Performance Ti-Mo Alloys Used on a Puncture Needle: The Role of Linear Energy Density in Microstructure Evolution and Mechanical Properties, 2025, Cryst 15 (15) (2025) 149, https://doi.org/10.3390/CRYST15020149.
[132] J. Peterson, S. Kariya, A. Issariyapat, J. Umeda, K. Kondoh, Experimentally mapping the oriented-to-misoriented transition in laser powder bed fusion Ti-10% Mo alloys, Scr. Mater. 231 (2023) 115472, https://doi.org/10.1016/J.SCRIPTAMAT.2023.115472.
[133] K. Zhao, X. Zhou, T. Hu, Y. Li, Z. Ye, F. Zhang, M. Wang, H. Tan, Microstructure characterization and tensile properties of Ti–15Mo alloy formed by directed energy deposition, Mater. Sci. Eng. A 858 (2022) 144103, https://doi.org/10.1016/J.MSEA.2022.144103.

[134] J.M. Borgman, J. Wang, L. Zani, P.P. Conway, C. Torres-Sanchez, The Effect of Energy Density and Nb Content on the Microstructure and Mechanical Properties of Selective Laser Melted Ti-(10–30 wt%) Nb, J. Mater. Eng. Perform. 30 (2021) 8771–8783, https://doi.org/10.1007/S11665-021-06239-5/FIGURES/14.
[135] D. Zhao, C. Han, J. Li, J. Liu, Q. Wei, situ fabrication of a titanium-niobium alloy with tailored microstructures, enhanced mechanical properties and biocompatibility by using selective laser melting, Mater. Sci. Eng. C. 111 (2020) 110784, https://doi.org/10.1016/J.MSEC.2020.110784.
[136] M. Fischer, D. Joguet, G. Robin, L. Peltier, P. Laheurte, situ elaboration of a binary Ti–26Nb alloy by selective laser melting of elemental titanium and niobium mixed powders, Mater. Sci. Eng. C. 62 (2016) 852–859, https://doi.org/10.1016/J.MSEC.2016.02.033.
[137] N. Singh, K.P. Srikanth, V. Gopal, M. Rajput, G. Manivasagam, K.G. Prashanth, K. Chatterjee, S. Suwas, situ production of low-modulus Ti–Nb alloys by selective laser melting and their functional assessment toward orthopedic applications, J. Mater. Chem. B 12 (2024) 5982–5993, https://doi.org/10.1039/D4TB00379A.
[138] S. Huang, P. Kumar, W.Y. Yeong, R.L. Narayan, U. Ramamurty, Fracture behavior of laser powder bed fusion fabricated Ti41Nb via in-situ alloying, Acta Mater. 225 (2022) 117593, https://doi.org/10.1016/J.ACTAMAT.2021.117593.
[139] G.R. Chou, S. Huang, S.L. Sing, The effect of thermal rest time during in situ alloying of Ti41Nb through laser powder bed fusion, 3, Mater. Sci. Addit. Manuf. 2024 3 (3) (2024) 3506, https://doi.org/10.36922/MSAM.3506.
[140] H. Ben Boubaker, P. Laheurte, G. Le Coz, S.S. Biriaie, P. Didier, P. Lohmuller, A. Moufki, Impact of the Loading Conditions and the Building Directions on the Mechanical Behavior of Biomedical β-Titanium Alloy Produced In Situ by Laser-Based Powder Bed Fusion, 2022, Mater 15 (15) (2022) 509, https://doi.org/10.3390/MA15020509.
[141] Y.P. Sharkeev, A.Y. Eroshenko, Z.G. Kovalevskaya, A.A. Saprykin, E.A. Ibragimov, I.A. Glukhov, M.A. Khimich, P.V. Uvarkin, E.V. Babakova, Structural and Phase State of Ti–Nb Alloy at Selective Laser Melting of the Composite Powder, Russ. Phys. J. 59 (2016) 430–434, https://doi.org/10.1007/S11182-016-0790-Z/METRICS.
[142] J.C. Wang, Y.J. Liu, P. Qin, S.X. Liang, T.B. Sercombe, L.C. Zhang, Selective laser melting of Ti–35Nb composite from elemental powder mixture: Microstructure, mechanical behavior and corrosion behavior, Mater. Sci. Eng. A 760 (2019) 214–224, https://doi.org/10.1016/J.MSEA.2019.06.001.
[143] M.A. Surmeneva, A. Koptyug, D. Khrapov, Y.F. Ivanov, T. Mishurova, S. Evsevleev, O. Prymak, K. Loza, M. Epple, G. Bruno, R.A. Surmenev, situ synthesis of a binary Ti–10at% Nb alloy by electron beam melting using a mixture of elemental niobium and titanium powders, J. Mater. Process. Technol. 282 (2020) 116646, https://doi.org/10.1016/J.JMATPROTEC.2020.116646.
[144] D. Zhao, C. Han, Y. Li, J. Li, K. Zhou, Q. Wei, J. Liu, Y. Shi, Improvement on mechanical properties and corrosion resistance of titanium-tantalum alloys in-situ fabricated via selective laser melting, J. Alloy. Compd. 804 (2019) 288–298, https://doi.org/10.1016/J.JALLCOM.2019.06.307.
[145] I. Polozov, V. Nefyodova, A. Zolotarev, V. Sokolova, A. Gracheva, A. Popovich, Development of low-modulus Ti-Ta alloys by in-situ synthesis during selective laser melting for implant applications, J. Alloy. Compd. 1021 (2025) 179682, https://doi.org/10.1016/J.JALLCOM.2025.179682.
[146] N. Soro, H. Attar, E. Brodie, M. Veidt, A. Molotnikov, M.S. Dargusch, Evaluation of the mechanical compatibility of additively manufactured porous Ti–25Ta alloy for load-bearing implant applications, J. Mech. Behav. Biomed. Mater. 97 (2019) 149–158, https://doi.org/10.1016/J.JMBBM.2019.05.019.
[147] S. Huang, S.L. Sing, G. de Looze, R. Wilson, W.Y. Yeong, Laser powder bed fusion of titanium-tantalum alloys: Compositions and designs for biomedical applications, J. Mech. Behav. Biomed. Mater. 108 (2020), https://doi.org/10.1016/j.jmbbm.2020.103775.
[148] S.L. Sing, W.Y. Yeong, F.E. Wiria, Selective laser melting of titanium alloy with 50 wt% tantalum: Microstructure and mechanical properties, J. Alloy. Compd. 660 (2016) 461–470, https://doi.org/10.1016/J.JALLCOM.2015.11.141.
[149] Q. Liu, Y. Zhang, W. Chen, P. He, Y. Tian, Y. Liu, Y. Dou, H. Bian, J. Yang, Q. Yang, X. Li, Bioactive and fatigue-resistant Ti–Ta alloy by additive manufacturing for orthopedic applications, Smart Mater. Manuf. 3 (2025) 100086, https://doi.org/10.1016/J.SMMF.2025.100086.
[150] S.L. Sing, F.E. Wiria, W.Y. Yeong, Selective laser melting of titanium alloy with 50 wt% tantalum: Effect of laser process parameters on part quality, Int. J. Refract. Met. Hard Mater. 77 (2018) 120–127, https://doi.org/10.1016/J.IJRMHM.2018.08.006.
[151] D. Zhao, H. Liang, C. Han, J. Li, J. Liu, K. Zhou, C. Yang, Q. Wei, 3D printing of a titanium-tantalum Gyroid scaffold with superb elastic admissible strain, bioactivity and in-situ bone regeneration capability, Addit. Manuf. 47 (2021) 102223, https://doi.org/10.1016/J.ADDMA.2021.102223.
[152] Y. Xu, Y. Fu, J. Li, W. Xiao, X. Zhao, C. Ma, Effects of tungsten addition on the microstructural stability and properties of Ti-6.5Al-2Sn-4Hf-2Nb-based high temperature titanium alloys, J. Mater. Sci. Technol. 93 (2021) 147–156, https://doi.org/10.1016/J.JMST.2021.02.057.
[153] M.Y. Mendoza, P. Samimi, D.A. Brice, B.W. Martin, M.R. Rolchigo, R. LeSar, P. C. Collins, Microstructures and Grain Refinement of Additive-Manufactured Ti-xW Alloys, Metall. Mater. Trans. A 2017 487 48 (2017) 3594–3605, https://doi.org/10.1007/S11661-017-4117-7.
[154] M.R. Rolchigo, M.Y. Mendoza, P. Samimi, D.A. Brice, B. Martin, P.C. Collins, R. LeSar, Modeling of Ti-W Solidification Microstructures Under Additive Manufacturing Conditions, Metall. Mater. Trans. A Phys. Metall. Mater. Sci. 48 (2017) 3606–3622, https://doi.org/10.1007/S11661-017-4120-Z/FIGURES/11.
[155] H. Attar, M. Bönisch, M. Calin, L.C. Zhang, S. Scudino, J. Eckert, Selective laser melting of in situ titanium–titanium boride composites: Processing, microstructure and mechanical properties, Acta Mater. 76 (2014) 13–22, https://doi.org/10.1016/J.ACTAMAT.2014.05.022.
[156] M.J. Bermingham, D. Kent, H. Zhan, D.H. Stjohn, M.S. Dargusch, Controlling the microstructure and properties of wire arc additive manufactured Ti–6Al–4V with trace boron additions, Acta Mater. 91 (2015) 289–303, https://doi.org/10.1016/J.ACTAMAT.2015.03.035.
[157] P.K. Verma, S. Warghane, U. Nichul, P. Kumar, A. Dhole, V. Hiwarkar, Effect of boron addition on microstructure, hardness and wear performance of Ti-6Al-4 V alloy manufactured by laser powder bed fusion additive manufacturing, Mater. Charact. 172 (2021) 110848, https://doi.org/10.1016/J.MATCHAR.2020.110848.
[158] S.A. Mantri, T. Alam, D. Choudhuri, C.J. Yannetta, C.V. Mikler, P.C. Collins, R. Banerjee, The effect of boron on the grain size and texture in additively manufactured β-Ti alloys, J. Mater. Sci. 52 (2017) 12455–12466, https://doi.org/10.1007/S10853-017-1371-4/METRICS.
[159] W. Ye, Y. Tian, D. Zhou, P. Li, J. Lei, Y. Zhang, Thermal Model and Numerical Simulation of Selective Laser Alloying Process of Elemental Ti and B, Met. Mater. Int. 27 (2021) 2791–2808, https://doi.org/10.1007/S12540-020-00955-8/FIGURES/10.
[160] K. Kondoh, M. Fukuo, S. Kariya, K. Shitara, S. Li, A. Alhazaa, J. Umeda, Quantitative strengthening evaluation of powder metallurgy Ti–Zr binary alloys with high strength and ductility, J. Alloy. Compd. 852 (2021) 156954, https://doi.org/10.1016/J.JALLCOM.2020.156954.
[161] Q. Xie, Y. Cao, J. Huang, N. Li, Y. Liu, Effect of laser energy density on microstructural evolution of selective laser melted Ti-15Zr alloy, J. Alloy. Compd. 934 (2023) 167778, https://doi.org/10.1016/J.JALLCOM.2022.167778.
[162] F. Arias-González, A. Rodríguez-Contreras, M. Punset, J.M. Manero, Ó. Barro, M. Fernández-Arias, F. Lusquiños, F.J. Gil, J. Pou, In-Situ Laser Directed Energy Deposition of Biomedical Ti-Nb and Ti-Zr-Nb Alloys from Elemental Powders, 2021, Met 11 (11) (2021) 1205, https://doi.org/10.3390/MET11081205.
[163] Y. Lee, S. Li, T. Lee, J.S. Oh, T.H. Nam, J.S. Lee, J.G. Kim, Mechanical property of the shape memorable Ti–Zr–Nb–Sn alloy manufactured by in-situ alloying in directed energy deposition, J. Mater. Res. Technol. 28 (2024) 11–21, https://doi.org/10.1016/J.JMRT.2023.11.261.
[164] K. Gama Sales de Souza, K. Pantleon, F.B. Grumsen, R. Caram, M. Villa, In-situ investigation of phase transformations in Ti-Nb-Zr alloys by simultaneous synchrotron diffraction and dilatometry, J. Alloy. Compd. 1024 (2025) 180199, https://doi.org/10.1016/J.JALLCOM.2025.180199.
[165] W. Kong, S.C. Cox, Y. Lu, V. Villapun, X. Xiao, W. Ma, M. Liu, M.M. Attallah, The influence of zirconium content on the microstructure, mechanical properties, and biocompatibility of in-situ alloying Ti-Nb-Ta based β alloys processed by selective laser melting, Mater. Sci. Eng. C. 131 (2021) 112486, https://doi.org/10.1016/J.MSEC.2021.112486.
[166] J. Zhou, Y. Wang, G. Zhi, L. He, Effect of Laser Power on Anisotropic Microstructure and Mechanical Behavior of Biomedical Ti-35Nb-15Zr (at%) Alloy Fabricated by Laser Powder Bed Fusion, Met. Mater. Int. 30 (2024) 240–252, https://doi.org/10.1007/S12540-023-01494-8/METRICS.
[167] R. Jing, S.X. Liang, C.Y. Liu, M.Z. Ma, X.Y. Zhang, R.P. Liu, Structure and mechanical properties of Ti–6Al–4V alloy after zirconium addition, Mater. Sci. Eng. A 552 (2012) 295–300, https://doi.org/10.1016/J.MSEA.2012.05.043.
[168] X.J. Jiang, S.J. Bao, L.W. Zhang, X.Y. Zhang, L.S. Jiao, H.B. Qi, F. Wang, Effect of Zr on microstructure and properties of TC4 alloy fabricated by laser additive manufacturing, J. Mater. Res. Technol. 24 (2023) 8782–8792, https://doi.org/10.1016/J.JMRT.2023.05.137.
[169] P. Qin, Y. Liu, T.B. Sercombe, Y. Li, C. Zhang, C. Cao, H. Sun, L.C. Zhang, Improved Corrosion Resistance on Selective Laser Melting Produced Ti-5Cu Alloy after Heat Treatment, ACS Biomater. Sci. Eng. 4 (2018) 2633–2642, https://doi.org/10.1021/ACSBIOMATERIALS.8B00319.
[170] M.H. Mosallanejad, B. Niroumand, A. Aversa, D. Manfredi, A. Saboori, Laser Powder Bed Fusion in-situ alloying of Ti-5%Cu alloy: Process-structure relationships, J. Alloy. Compd. 857 (2021) 157558, https://doi.org/10.1016/J.JALLCOM.2020.157558.
[171] M. Talebi, A. Razaghian, A. Saboori, B. Niroumand, Effects of Cu addition and heat treatment on the microstructure and hardness of pure Ti prepared by Selective laser melting (SLM), J. Ultra Graine Nanostruct. Mater. 56 (2023) 213–223, https://doi.org/10.22059/JUFGNSM.2023.02.10.
[172] P.M. Terceiro, L.A. Leão, J.F.Q. Rodrigues, M. Sangali, R.J. Contieri, R. Caram, J. Soyama, Microstructural Evolution of Ti–2.5Cu Alloys Produced by Powder Metallurgy and Laser Powder Bed Fusion, Metall. Mater. Trans. A 2025 564 56 (2025) 1449–1460, https://doi.org/10.1007/S11661-025-07709-4.
[173] Y. Han, H.R. Wang, Y.D. Cao, W.T. Hou, S.J. Li, Improved Corrosion Resistance of Selective Laser Melted Ti–5Cu Alloy Using Atomized Ti–5Cu Powder, Acta Metall. Sin. (Engl. Lett. 32 (2019) 1007–1014, https://doi.org/10.1007/S40195-019-00896-1/METRICS.
[174] H. Ji, M.C. Zhao, B. Xie, Y.C. Zhao, D. Yin, C. Gao, C. Shuai, A. Atrens, Corrosion and antibacterial performance of novel selective-laser-melted (SLMed) Ti-xCu biomedical alloys, J. Alloy. Compd. 864 (2021) 158415, https://doi.org/10.1016/J.JALLCOM.2020.158415.
[175] Q. Wang, K. Zhang, W. Niu, Microstructural characteristic and mechanical properties of titanium-copper alloys in-situ fabricated by selective laser melting, J. Alloy. Compd. 885 (2021) 161032, https://doi.org/10.1016/J.JALLCOM.2021.161032.
[176] A. Issariyapat, J. Huang, S. Kariya, B. Chen, S. Li, J. Umeda, K. Yamanaka, A. Chiba, K. Kondoh, Sustainable alloy design: Fe-enhanced Ti alloys for superior mechanical performance in additive manufacturing, J. Alloy. Compd. 1010 (2025) 177767, https://doi.org/10.1016/J.JALLCOM.2024.177767.

[177] (PDF) Cost Effective In-Situ Alloying of Ti-Fe via Laser Powder Bed Fusion, (n.d.). https://www.researchgate.net/publication/374819574_Cost_Effective_In-Situ_Alloying_of_Ti-Fe_via_Laser_Powder_Bed_Fusion (accessed October 29, 2025).
[178] J. Huang, A. Issariyapat, S. Kariya, J. Umeda, K. Kondoh, On the viability of in-situ alloyed Ti-1Fe as a strong and ductile alternative to Ti-6Al-4V for laser-based powder bed fusion, Addit. Manuf. 105 (2025) 104788, https://doi.org/10.1016/J.ADDMA.2025.104788.
[179] C.L. Shi, Y. Wang, M. Zhang, W.R. Yang, H.J. Li, Z.W. Yang, Refinement of microstructure and improvement of mechanical properties of directed energy deposited titanium alloys by adding Fe, J. Alloy. Compd. 1010 (2025) 176996, https://doi.org/10.1016/J.JALLCOM.2024.176996.
[180] H. Wang, H.L. Luo, J.Q. Chen, J.C. Tang, X.Y. Yao, Y.H. Zhou, M. Yan, Cost-affordable, biomedical Ti-5Fe alloy developed using elemental powders and laser in-situ alloying additive manufacturing, Mater. Charact. 182 (2021) 111526, https://doi.org/10.1016/J.MATCHAR.2021.111526.
[181] D. Chen, R. Das, S. Lu, M. Qian, D. Qiu, In-situ elimination of β-flecks in additively manufactured Ti-3.5 wt% Fe alloy, J. Mater. Res. Technol. 29 (2024) 839–850, https://doi.org/10.1016/J.JMRT.2024.01.153.
[182] X. Pang, C. Chen, T. Yan, K. Wang, X. Ji, X. Luo, J. Zhang, M. Zhang, L. Tang, Y. Feng, Effect of Cu addition on microstructure evolution and strength-ductility synergy of LDED Ti–Fe–Cu ternary alloys, J. Mater. Res. Technol. 43 (2026) 4472–4482, https://doi.org/10.1016/J.JMRT.2026.07.016.
[183] B.A. Welk, N. Taylor, Z. Kloenne, K.J. Chaput, S. Fox, H.L. Fraser, Use of Alloying to Effect an Equiaxed Microstructure in Additive Manufacturing and Subsequent Heat Treatment of High-Strength Titanium Alloys, Metall. Mater. Trans. A 2021 5212 52 (2021) 5367–5380, https://doi.org/10.1007/S11661-021-06475-3.
[184] C. Wang, X.P. Tan, Z. Du, S. Chandra, Z. Sun, C.W.J. Lim, S.B. Tor, C.S. Lim, C. H. Wong, Additive manufacturing of NiTi shape memory alloys using pre-mixed powders, J. Mater. Process. Technol. 271 (2019) 152–161, https://doi.org/10.1016/J.JMATPROTEC.2019.03.025.
[185] T. Zhang, C. Chen, R. Li, K. Zhou, Effect of Cr content on the microstructure and mechanical properties of Ti–Cr alloys manufactured by laser directed energy deposition, Mater. Sci. Eng. A 893 (2024) 146143, https://doi.org/10.1016/J.MSEA.2024.146143.
[186] C. Cui, B.M. Hu, L. Zhao, S. Liu, Titanium alloy production technology, market prospects and industry development, Mater. Des. 32 (2011) 1684–1691, https://doi.org/10.1016/J.MATDES.2010.09.011.
[187] C. Ni, J. Zhu, B. Zhang, K. An, Y. Wang, D. Liu, W. Lu, L. Zhu, C. Liu, Recent advance in laser powder bed fusion of Ti–6Al–4V alloys: microstructure, mechanical properties and machinability, Virtual Phys. Prototyp. 20 (2025), https://doi.org/10.1080/17452759.2024.2446952;JOURNAL:JOURNAL:NVPP20;REQUESTEDJOURNAL:JOURNAL:NVPP20;PAGE:STRING:ARTICLE/CHAPTER.
[188] E. Eshed, A. Shirizly, Characterization of Nano-Sized Features in Powder Bed Additively Manufactured Ti-6Al-4V Alloy, 2025, Mater 18 (18) (2025) 3198, https://doi.org/10.3390/MA18133198.
[189] H.D. Nguyen, A. Pramanik, A.K. Basak, Y. Dong, C. Prakash, S. Debnath, S. Shankar, I.S. Jawahir, S. Dixit, D. Buddhi, A critical review on additive manufacturing of Ti-6Al-4V alloy: microstructure and mechanical properties, J. Mater. Res. Technol. 18 (2022) 4641–4661, https://doi.org/10.1016/J.JMRT.2022.04.055.
[190] T. Kakiuchi, R. Kawaguchi, M. Nakajima, M. Hojo, K. Fujimoto, Y. Uematsu, Prediction of fatigue limit in additively manufactured Ti-6Al-4V alloy at elevated temperature, Int. J. Fatigue 126 (2019) 55–61, https://doi.org/10.1016/J.IJFATIGUE.2019.04.025.
[191] J.A. Tamayo, M. Riascos, C.A. Vargas, L.M. Baena, Additive manufacturing of Ti6Al4V alloy via electron beam melting for the development of implants for the biomedical industry, Heliyon 7 (2021), https://doi.org/10.1016/J.HELIYON.2021.E06892.
[192] A.; Moridi, A.G.; Demir, L.; Caprio, A.J.; Hart, B.; Previtali, B.M. Colosimo, A. Moridi, A.G. Demir, L. Caprioc, A.J. Hart, B. Previtali, B.M. Colosimo, Deformation and failure mechanisms of Ti-6Al-4V as built by selective laser melting, (n.d.). https://doi.org/10.1016/j.msea.2019.138456.
[193] T.C. Dzogbewu, W.B. du Preez, Fused tracks and layers of Ti10Mo6Cu data obtained via laser powder bed fusion, Data Br. 46 (2023) 108775, https://doi.org/10.1016/J.DIB.2022.108775.
[194] Y. Liu, J. Zhang, Q. Tan, Y. Yin, M. Li, M.X. Zhang, Mechanical performance of simple cubic architected titanium alloys fabricated via selective laser melting, Opt. Laser Technol. 134 (2021) 106649, https://doi.org/10.1016/J.OPTLASTEC.2020.106649.
[195] I. Polozov, V. Sufiiarov, A. Popovich, D. Masaylo, A. Grigoriev, Synthesis of Ti-5Al, Ti-6Al-7Nb, and Ti-22Al-25Nb alloys from elemental powders using powder-bed fusion additive manufacturing, J. Alloy. Compd. 763 (2018) 436–445, https://doi.org/10.1016/J.JALLCOM.2018.05.325.
[196] A.A. Popovich, V.S. Sufiiarov, I.A. Polozov, A.V. Grigoriev, Selective Laser Melting of the Intermetallic Titanium Alloy, Russ. J. Non-Ferr. Met. 60 (2019) 186–193, https://doi.org/10.3103/S1067821219020081/METRICS.
[197] K. Praveen kumar, V. Gopal, S. Prasanth, G. Manivasagam, K. Chatterjee, S. Suwas, Tribocorrosion of biomedical Ti-Nb-Ta alloys fabricated by directed energy deposition using elemental powders, Tribol. Int. 211 (2025) 110906, https://doi.org/10.1016/J.TRIBOINT.2025.110906.
[198] H. Dobbelstein, E.L. Gurevich, E.P. George, A. Ostendorf, G. Laplanche, Laser metal deposition of compositionally graded TiZrNbTa refractory high-entropy alloys using elemental powder blends, Addit. Manuf. 25 (2019) 252–262, https://doi.org/10.1016/J.ADDMA.2018.10.042.
[199] I. Polozov, V. Sokolova, A. Gracheva, A. Zolotarev, V. Nefyodova, A. Popovich, Ti-Ta-Cu Biocompatible Alloy System Development via Selective Laser Melting for Prosthetic Applications, 1177, Met 14 (14) (2024) 1177, https://doi.org/10.3390/MET14101177.
[200] J. Zhang, M.J. Bermingham, J. Otte, Y. Liu, Z. Hou, N. Yang, Y. Yin, M. Bayat, W. Lin, X. Huang, D.H. StJohn, M.S. Dargusch, Ultrauniform, strong, and ductile 3D-printed titanium alloy through bifunctional alloy design, 80-. Science 383 (2024) 639–645, https://doi.org/10.1126/SCIENCE.ADJ0141;WEBSITE:WEBSITE:AAAS-SITE;JOURNAL:JOURNAL:SCIENCE;WGROUP:STRING:PUBLICATION.
[201] K.Y. Kim, J.H. Kim, D.W. Yun, P.L. Narayana, J.H. Kim, J.I. Lee, J.K. Hong, Enhancing the mechanical properties and corrosion resistance of commercially pure titanium using tungsten carbide composites fabricated via additive manufacturing, J. Mater. Res. Technol. 27 (2023) 5070–5081, https://doi.org/10.1016/J.JMRT.2023.11.051.
[202] V. Popovich, T. Becker, T. Gries, J. Li, J. Xiong, Y. Sun, Q. Wei, Influence of Tungsten Addition on Microstructure and Tensile Properties of Ti6Al4V Fabricated by Laser-Directed Energy Deposition, 2023, Met 13 (13) (2023) 1064, https://doi.org/10.3390/MET13061064.
[203] Q. Wu, X. Wang, K. Li, Y. Zhou, S. Wen, Y. Shi, Microstructure and mechanical properties of Ti6Al4V/W bimetallic structure via selective laser melting, Int. J. Refract. Met. Hard Mater. 121 (2024) 106683, https://doi.org/10.1016/J.IJRMHM.2024.106683.
[204] R.A. Rahman Rashid, S. Palanisamy, H. Attar, M. Bermingham, M.S. Dargusch, Metallurgical features of direct laser-deposited Ti6Al4V with trace boron, J. Manuf. Process. 35 (2018) 651–656, https://doi.org/10.1016/J.JMAPRO.2018.09.018.
[205] A. Sola, A. Trinchi, Boron-induced microstructural manipulation of titanium and titanium alloys in additive manufacturing, Virtual Phys. Prototyp. 18 (2023), https://doi.org/10.1080/17452759.2023.2230467.
[206] V.S. Goettgens, L. Kaserer, J. Braun, I. Letofsky-Papst, S. Mitsche, G. Leichtfried, Microstructure of a modulated Ti-6Al-4V – Cu alloy fabricated via in situ alloying in laser powder bed fusion, Materialia 28 (2023) 101731, https://doi.org/10.1016/J.MTLA.2023.101731.
[207] M.H. Mosallanejad, B. Niroumand, C. Ghibaudo, S. Biamino, A. Salmi, P. Fino, A. Saboori, In-situ alloying of a fine grained fully equiaxed Ti-based alloy via electron beam powder bed fusion additive manufacturing process, Addit. Manuf. 56 (2022) 102878, https://doi.org/10.1016/J.ADDMA.2022.102878.
[208] J. Li, X. Liu, X. Luo, F. Gao, C. Zhao, B. Ma, D. Li, C. Yang, Overcoming the strength-ductility trade-off and anisotropy of mechanical properties of Ti6Al4V with electron beam powder bed fusion, Mater. Sci. Eng. A 879 (2023) 145301, https://doi.org/10.1016/J.MSEA.2023.145301.
[209] T.W. Kim, D.H. Kim, Y.T. Cho, C.M. Lee, Manufacturing high strength Ti alloy with in-situ Cu alloying via directed energy deposition and evaluation of material properties, J. Mater. Res. Technol. 28 (2024) 1810–1823, https://doi.org/10.1016/J.JMRT.2023.12.115.
[210] F.F. Ahmed, S.J. Clark, C.L. Alex Leung, L. Stanger, J. Willmott, S. Marussi, V. Honkimaki, N. Haynes, H.S. Zurob, P.D. Lee, A.B. Phillion, Achieving homogeneity in a high-Fe β-Ti alloy laser-printed from blended elemental powders, Mater. Des. 210 (2021) 110072, https://doi.org/10.1016/J.MATDES.2021.110072.
[211] Q. Zhou, X.Z. Zhang, H.P. Tang, M. Qian, Electron beam additively manufactured Ti–1Al–8V–5Fe alloy: In-situ precipitation hardening, tensile properties and fracture characteristics, Mater. Sci. Eng. A 865 (2023) 144639, https://doi.org/10.1016/J.MSEA.2023.144639.
[212] H. Azizi, H. Zurob, B. Bose, S. Reza Ghiaasiaan, X. Wang, S. Coulson, V. Duz, A. B. Phillion, Additive manufacturing of a novel Ti-Al-V-Fe alloy using selective laser melting, Addit. Manuf. 21 (2018) 529–535, https://doi.org/10.1016/J.ADDMA.2018.04.006.
[213] C. Shang, J. Zheng, X. Hou, K. Jin, M. Chu, S. Zhang, Microstructure and tensile performance of Ti-1Al-8V-5Fe alloy produced by laser powder bed fusion versus directed energy deposition, Vacuum 234 (2025) 114114, https://doi.org/10.1016/J.VACUUM.2025.114114.
[214] T. Song, Z. Chen, X. Cui, S. Lu, H. Chen, H. Wang, T. Dong, B. Qin, K.C. Chan, M. Brandt, X. Liao, S.P. Ringer, M. Qian, Strong and ductile titanium–oxygen–iron alloys by additive manufacturing, 2023 6187963, Nat 618 (2023) 63–68, https://doi.org/10.1038/s41586-023-05952-6.
[215] S. Sui, Y. Chew, F. Weng, C. Tan, Z. Du, G. Bi, Achieving grain refinement and ultrahigh yield strength in laser aided additive manufacturing of Ti−6Al−4V alloy by trace Ni addition, Virtual Phys. Prototyp. 16 (2021) 417–427, https://doi.org/10.1080/17452759.2021.1949091.
[216] P.L. Narayana, S. Lee, S.W. Choi, C.L. Li, C.H. Park, J.T. Yeom, N.S. Reddy, J. K. Hong, Microstructural response of β-stabilized Ti–6Al–4V manufactured by direct energy deposition, J. Alloy. Compd. 811 (2019) 152021, https://doi.org/10.1016/J.JALLCOM.2019.152021.
[217] Y. Byun, S. Lee, S.M. Seo, J. taek Yeom, S.E. Kim, N. Kang, J. Hong, Effects of Cr and Fe Addition on Microstructure and Tensile Properties of Ti–6Al–4V Prepared by Direct Energy Deposition, 2018 246, Met. Mater. Int. 24 (2018) 1213–1220, https://doi.org/10.1007/S12540-018-0148-X.
[218] X. Wang, L.J. Zhang, S.J. Na, Effect of manganese on grain morphology and microstructure of Ti-6Al-4V alloy by laser wire deposition, J. Mater. Res. Technol. 32 (2024) 1141–1151, https://doi.org/10.1016/J.JMRT.2024.07.167.
[219] S. Patel, M. Vlasea, Melting modes in laser powder bed fusion, Materialia 9 (2020), https://doi.org/10.1016/j.mtla.2020.100591.

[220] L. Cai, W. Guo, H. Fu, M. Song, I. Baker, H. Wu, Multiscale segregation and phase transformation mechanisms in an in-situ alloyed Ti-Al-Fe alloy, Scr. Mater. 284 (2026) 117472, https://doi.org/10.1016/J.SCRIPTAMAT.2026.117472.
[221] Q. Jia, J. Li, Z. Zhou, Q. Zhou, G. Gao, S.J. Eder, Z. Yang, Nanowear of Zr-based metallic glasses regulated by cooling rate-induced heterogeneity, Int. J. Mech. Sci. 321 (2026) 111666, https://doi.org/10.1016/J.IJMECSCI.2026.111666.
[222] Y. Ren, L. Zhu, Y. Li, Q. Zhou, S.J. Eder, X. Sui, Q. Wu, H. Wang, Z. Wang, C. Gachot, J. Wang, W. Liu, Cryogenic tribological breakthroughs in medium-entropy alloy composites via regulated partial recrystallization, 2026 698, Sci. China Mater. 69 (2026) 4896–4911, https://doi.org/10.1007/S40843-025-4018-6.
[223] A. Limbeck, L. Brunnbauer, H. Lohninger, P. Pořízka, P. Modlitbová, J. Kaiser, P. Janovszky, A. Kéri, G. Galbács, Methodology and applications of elemental mapping by laser induced breakdown spectroscopy, Anal. Chim. Acta 1147 (2021) 72–98, https://doi.org/10.1016/j.aca.2020.12.054.
[224] C. Chen, Z. Zhang, Y. Cai, Y. Liu, H. Chen, Research and development status of in situ field assisted laser additive manufacturing: a review, Opt. Laser Technol. 181 (2025), https://doi.org/10.1016/j.optlastec.2024.111700.
[225] Y. Dong, Z. Jiao, Y. Ma, Q. Zhou, M. Yang, X. Ran, Z. Wang, C. Tang, Y. Li, X. Li, H. Teng, X. Lu, X. Liu, A systematic review on advanced surface coating technologies for high-pressure piston pumps, Def. Technol. 59 (2026) 288–309, https://doi.org/10.1016/J.DT.2025.10.018.
[226] Z. Wang, Y. Shi, Y. Liu, L. Feng, J. Yu, Y. Shen, G. An, D. Hua, J. Gao, B. Zhang, S. Lezhnev, E. Trofimov, Q. Zhou, Tribo-corrosion performances of high-entropy alloy coatings for biomedical applications: a review, J. Alloy. Compd. 1073 (2026) 189048, https://doi.org/10.1016/J.JALLCOM.2026.189048.
[227] Q. Zhou, Z. Jiao, Z. Huang, Y. Shi, Y. Li, C. Yin, H. Wang, H.C. Pinto, C. Greiner, W. Liu, Wear-resistant CrCoNi nanocrystalline film via friction-driven surface segregation, Acta Mater. 279 (2024) 120299, https://doi.org/10.1016/J.ACTAMAT.2024.120299.